Nonlinear microscopy for temporally and spatially resolved label-free imaging of living cells

THÈSE N^{O} 8891 (2018)

PRÉSENTÉE LE 23 NOVEMBRE 2018

À LA FACULTÉ DES SCIENCES ET TECHNIQUES DE L'INGÉNIEUR

CHAIRE JULIA JACOBI DE PHOTOMÉDECINE - LABORATOIRE DE BIOPHOTONIQUE FONDAMENTALE

PROGRAMME DOCTORAL EN PHOTONIQUE

ÉCOLE POLYTECHNIQUE FÉDÉRALE DE LAUSANNE

POUR L'OBTENTION DU GRADE DE DOCTEUR ÈS SCIENCES

PAR

Marie Eve Pascale DIDIER

acceptée sur proposition du jury:

Prof. C. Moser, président du jury
Prof. S. Roke, directrice de thèse
Dr S. Brasselet, rapporteuse
Dr E. Beaurepaire, rapporteur
Prof. D. Psaltis, rapporteuse

ÉCOLE POLYTECHNIQUE
FÉDÉRALE DE LAUSANNE

Suisse
2018

To my parents, Marie-Aimée and Daniel,
To my sister Pierrine and my brother Armand,
To my family and friends.

Acknowledgement

I would like to start this section with a quotation that I received from my mother when I was doing my Bachelor in Canada: “Travail et persévérance sont forces de réussite”. Throughout all these years, this sentence stayed in my head as a self-motivation. Indeed, this thesis represents not only a 5-year-long personal and scientific achievement but also marks a long-term accomplishment that would not have been possible without a benevolent surrounding.

Foremost, I am deeply grateful to have done my PhD in the Laboratory for fundamental BioPhotonics (LBP) at Ecole Polytechnique Fédérale de Lausanne with Professor Sylvie Roke, who was my PhD supervisor for these past 5 years. The workplace, the infrastructures and the research facility within the LBP and at EPFL were exquisite. The whole PhD’s apprenticeship would not have been the same without my supervisor, she occupied a significant place in this Bildungsroman that was my thesis. I would also like to thank R. Veselinov for her managing skills, her attentive ear and for making administrative tasks such a non-existent burden here!

I would like to express my sincere gratitude to C. Macias-Romero, for his continuous support, his introduction to the methodology of the PhD life and his precious scientific guidelines. He introduced me to the “every day” research life, with ups and downs. He was an important scientific figure throughout all these years and will always remain a good friend whom I appreciate discussing and taking breaks with. I would like to give a special mention to my collaborators from the Science de la Vie (SV) department: E. Ruchti, E. Gasparetto and M. Wirth for their great jobs in providing the cultures of neurons, which were essential for my experimental works. I would sincerely like to thank P. Jourdain, I. Allaman and P. Magistretti for their uttermost patience towards my neuroscience-related questions, their sharp views and advice, and their precious scientific knowledge. Thank you I. Allaman for your help and your contribution to my thesis.

Moreover, this thesis would have been impossible without the support of many external actors: my recognition goes to C. Buchs, for her understanding and her precious guidelines during these past 5 years, to O. Martin for his continuous listening, encouragement, comfort, scientific inputs and constructive remarks for my research and PhD life. A special acknowledgement goes to S. Brasselet for her excellent advice, cleverness, enthusiasm, scientific brainstorming and fair constructive

feedbacks. Her inputs were essential throughout my thesis and by her sides, I nourished my faith in academia. I sincerely thank E. Tyrode for his contribution to my thesis and his moral support.
Then comes one of the fundamental pillars of my intellectual and personal balance for these past 5 years: my surrounding friends. I would like to thank all of my colleagues from LBP: their support was essential, thank you for enduring my moods for so many years, for the fruitful discussions and for always being here when needed! I also discovered great friends in my colleagues, with whom Sat' breaks were often reiterated, thank you Orly, Jan, Nathan, Sergey, Maksim, Marie, Yixing, Igor, Siyuan, Filip, Arianna, Nikolay and thank you Claire and Halil for your feedbacks for my thesis! Thank you, Cornelis, for the introduction to the Lausanne night life, the PhD life, the LBP and SV HH EPFL life, for the great times we had together and for the great stories I will always remember. A special mention goes to Evi, your friendship, help, support and encouragement were fundamental. Your sense of humor, your Greek accent and the craziness of your parties were a must in my Lausanne time. Thanks for making everything less boring!
I would like to give a special acknowledgement to my friend and partner in crime Miguel, a great listener, always in to bring joy and happiness (and cold beverages) in our lives, for his great advice and smiley face. I gained a great friend during these struggling PhD times, and just for this I would not change anything. Completing the dream team, Semih, thank you for making us laugh, pulling my pipettes and bringing the party vibe always up (and your input in my neuroscience learning curve!). Valentin, Vincent, Gabriel and Jean-Christophe, I could not think of my EPFL time without you. You established the rocks of what became the party life style in Lausanne, Valentin, thank you for your exquisite cooking skills especially after sunset, for mingling with my neighbors and all of you for your cheering moods, the scientific help and discussions, the support and the Great Escape towards nights and days of laughter. The EPFL list can be endless, thank you Gabriele, Daniel for your endless opiniated debates, Philipp for your musical inputs, Dal for our productive philosophical walks and discussions and Federico P. for your joyful company. I would also like to thank Uzair, Miroslav, Dragan, the Markos and the whole Serbian community always here to enlighten our daily coffee breaks. I would like to stress a special thanks to Umar for your kindness and Federico N. for your support, your smile and help during my darkest and brightest times. My deepest gratitude also goes to the FINON family, Alexandra, Naya, Diana, Carolina, Xiao, Amala, Alberto, Attilio, Michael and my memories go to Juris, who will always remain present in our hearts. This adventure made us stronger, this European network was beneficial on a scientific and personal point of view and brought us all together with a strong friendship. Finally, I would like to thank all the people I met with the Forum EPFL when I was part of the committee and after, for our amazing time together, the great professional opportunities and friends that I made within this association.

My gratitude goes also to Jean-Victor, Marion and Antoine, EPFL outsiders and still part of the circle. I appreciated every moment spent together, rolling pasta dough with the tip of our fingers, enjoying our never-ending food discussions and all this wine we tasted together. I would like to thank my friends Natacha, Olivier D., Olivier M. and Richard for completing the picture, all of you contributed in a unique way to take my head off the PhD life, for the nice times, parties, dinners, balls, extended coffee breaks and delightful conversations we had together. My gratitude goes to Dylan, for his sharp comments, his down to earth views and our escapades together. Thank you, Laura-Mae, for all these years of friendship, our trips together, necessary to get away from the research life and our nice times on the road! The thank you list would not have been complete without mentioning my friend Ralph, for his support from my very first day at EPFL and for his precious contribution to my thesis! I would like to finish with my long-lasting friends Sophie, Alexandrine, Camille, Thibault and Pablo, Laurence and Maryline being together was always a pleasure in which I found great motivation and rejuvenation during the most stressful times of my studies and PhD!

I will finish this acknowledgement section by quoting Nietsche: "Without music, life would be a mistake". Indeed, music is a very important part of my life, especially during my busy times with research. Being a member of AROP brought me the exact amount of freedom, passion, breath and reward that was necessary to be even more productive back at EPFL. I would like to express my sincere gratitude to my "Opera friends", to Geo, I was always looking forward to attending all these magical events with you. To Nicolas, Honoré, Jacques-Alexandre, Pierre, Odile, Will, Camille, Rozemarijn, Antoine, Charles-Eric, Benoît, Cesar for your presence, our passionate debate about music, culture, literature, and Laurent to have always kept faith in me. We somehow always find each other somewhere in Europe for an opera or music festival, and this always brought me joy and motivation, necessary in my research. My sincere thanks go to the whole Juvenilia community, all the fascinating people I met there during my PhD years, all the events and trips we did together, all this amazing European network that we are building together and these fascinating wonderful moments spent in all the Operas of Europe, Galas, Balls, and out-of-reality events. I am also extremely proud to be a board member of Juvenilia now.

As an additional note, I would like to thank the whole team of "*Les Papous dans la tête*" and the extended team of France Culture. The richness of their topics, the humor and the intellectual excitement were essential for my intellectual health and moral support throughout all these years. My deep gratitude also goes to Hervé for his continuous encouragements, to the fairness of his judgement and unconditional faith towards me and to Ms. Brahier for her 5-year-long necessary support.

Finally, heartfelt thanks to my family, my father, my mother always here for me, for their thorough help during my whole studies, and especially to my mother for her contribution during my writing

periods. To my sister Pierrine, our trips together were always a great way to take a step back, to my brother Armand, to my cousin Bertille, to my extended family, grand-parents, aunts, uncles and cousins, all of you supported me a lot during these long 5 years and this all work and accomplishment would not have been possible without all of you.

Lausanne, 8th June 2018

Marie Didier

Abstract

The human brain consists of approximately a hundred billion of neurons that communicate through a unique series of biochemical and electrical processes. When neuronal networks are solicited, electrochemical processes happen involving millions of cells within a complex network. The morphology of the neuronal cytoskeleton is fundamental in the establishment of these complex neuronal networks and crucial for the functional integrity of electrical signaling. Traditionally, the neuronal morphology and electrical signals are measured with invasive optical probes, exogenous dyes, or by exogenous electrical recordings. To fully understand the underlying mechanisms involved in neuronal activity (morphological and electrical) and for eventual clinical applications a direct label-free non-invasive optical probe is of great significance. In this thesis we demonstrated the possibility of label-free imaging of neuronal structures and electrical neuronal activity employing the unique intrinsic sensitivity of nonlinear optical techniques.

We developed a 3D wide-field second harmonic (SH) imaging system that increases the SH imaging throughput for label-free elastic second harmonic generation (SHG) imaging by several orders of magnitude. The increase in throughput was achieved with a wide-field geometry and medium repetition rate laser source in combination with gated detection. In addition to enhanced throughput, dynamic and ultrafast measurements can be performed readily with different possible polarization configurations of the excitation and detection.

First, we performed label-free SH and two photon excitation fluorescence (2PEF) imaging of living cultured neurons with short acquisition time and at very low fluences. We demonstrated the use of wide-field high throughput SH microscopy for investigating dynamic changes in cytoskeletal morphology on the single cell level. The method allows real-time *in vitro* label-free measurements of cytoskeletal changes that can, under certain conditions, be quantified by orientational distribution or changes in the number of microtubules.

Then, we investigated the changes in neuronal morphology and metabolic activity by performing label-free SH polarimetry. We calculated the coefficient of polarization, which reports on orientational irregularities in the microtubule cytoskeleton, and used endogenous 2PEF as a metabolic marker in cultured neurons throughout the stages of their morphological development. Being able to observe morphological changes in the cytoskeleton of living neurons in a label-free way with clear

markers of organization in combination with indicators for metabolic activity, allows us to follow neuronal differentiation in detail, and in a non-invasive way.

Finally, we employed SH imaging to label-freely capture direct information of neuronal membrane potentials. We performed SH imaging of cultured neurons undergoing a chemical depolarization by a temporary extracellular excess of K^+ ions. To demonstrate the concept, we performed a patch-clamp and SH imaging comparison and showed that whole neuron membrane potential changes correlated linearly with the square root of the SH intensity. Finally, we used the nonlinear optical response of the membrane bound water to create membrane potential and ion flux maps of living cultured neurons in real time.

With these results obtained with the 3D wide-field high throughput SH microscope, we demonstrated the possibilities to image in time, label-free and with low fluence, neuronal structural changes and electrical neuronal activity employing the unique intrinsic sensitivity of nonlinear phenomena.

Keywords:

Nonlinear imaging, membrane water, spatiotemporal mapping, second harmonic generation imaging, label-free, neuronal activity, membrane potential

Résumé

Le cerveau humain comprend environ 100 milliards de neurones communicants entre eux par le biais de processus biochimiques et électriques. Lorsque des connexions neuronales sont sollicitées, des processus électrochimiques se produisent impliquant des millions de cellules au sein d'un réseau neuronal complexe. La morphologie du cytosquelette à l'échelle d'un neurone est fondamentale pour la construction des réseaux neuronaux et est cruciale pour l'intégrité fonctionnelle de la signalisation électrique. Les méthodes existantes pour l'étude de la structure morphologique neuronale et des signaux électriques font appel traditionnellement à des colorants exogènes, des sondes optiques invasives ou des enregistrements électriques exogènes.

Afin de comprendre pleinement les mécanismes sous-jacents impliqués dans l'activité neuronale (morphologique et électrique) et en vue d'application clinique future, une méthode optique directe, non invasive et sans marqueur est d'une grande importance. Dans cette thèse, nous démontrons la possibilité d'imagerie sans marquage des structures neuronales et de l'activité neuronale électrique en utilisant la sensibilité intrinsèque et unique des phénomènes physiques non linéaires.

Nous avons développé un système d'imagerie non linéaire (deuxième harmonique) 3D plein champ avec une grande efficacité d'imagerie, sans besoin de marqueurs. L'amélioration de l'efficacité d'imagerie est possible grâce à la configuration plein champ du microscope qui est couplé avec une source laser ayant un taux de répétition moyen. En plus d'une grande efficacité d'imagerie, ces paramètres permettent d'effectuer des mesures dynamiques et ultrarapides et donnent la possibilité d'imager avec différentes configurations de polarisation.

Premièrement, nous effectuons des mesures de deuxième harmonique et d'auto fluorescence à deux photons sur des cultures de neurones. Ces mesures sont faites avec un temps d'acquisition court et à des fluences (énergie déposée sur l'échantillon) très faibles. Nous démontrons l'utilisation de la microscopie de deuxième harmonique à champ plein pour étudier les changements dynamiques morphologiques du cytosquelette au sein même d'une cellule neuronale. La méthode permet de mesurer *in vitro* et en temps réel des modifications structurales du cytosquelette sans marquage qui peuvent, dans certaines conditions, être quantifiées par des fonctions de distribution d'orientation ou des changements de densité de microtubule, un des composés du cytosquelette. Nous avons ensuite effectué des mesures de polarimétrie et démontré l'influence de la directionnalité des microtubules à

l’échelle d’un pixel, dans le signal de deuxième harmonique. Nous pouvons extraire de ces mesures des informations orientationnelles dans les neurites et les corps cellulaires.

Ensuite, nous étudions les changements de morphologie neuronale et l'activité métabolique par l’étude polarimétrique du signal de deuxième harmonique en combinaison avec les signaux à deux photons, encore sans marqueurs. Tout au long du développement morphologique des neurones en culture, nous calculons le coefficient de polarisation, qui rapporte les irrégularités d'orientation des microtubules dans le cytosquelette et utilisons le signal à deux photons endogènes comme marqueur métabolique. Être capable d'identifier sans marqueurs les changements morphologiques dans le cytosquelette des neurones vivants, avec des marqueurs d'organisation structurale associés à des indicateurs d'activité métabolique, permet de suivre la différenciation neuronale en détail et peut servir d'indicateur pour déterminer l'âge relatif des neurones ainsi que leur état de dégradation en vue d’application clinique comme dans le cas de maladies neurodégénératives.

Enfin, nous utilisons l'imagerie de deuxième harmonique pour obtenir des informations sur le potentiel de membrane lié à l’activité électrique intrinsèque des neurones. Nous utilisons les changements dans les interactions entre les dipôles des molécules d’eau et les charges de la membrane pour retrouver un potentiel de membrane et créer des cartes sur le flux d'ions lors d’activité électrique. Pour démontrer le concept, nous avons effectué une comparaison entre une méthode traditionnelle, le patch-clamp et l'imagerie sans marqueur de deuxième harmonique. Nous avons montré que les changements de potentiel de membrane neuronale sont corrélés linéairement avec la racine carrée de l'intensité de deuxième harmonique, comme prédit par la théorie. Nous utilisons ensuite la réponse optique non linéaire des molécules d’eau à la surface de la membrane neuronale pour visualiser les changements spatio-temporels dans le potentiel membranaire ainsi que le flux d'ions K^+ des neurones cultivés lors d’une dépolarisation continue par un excès extracellulaire temporaire d'ions K^+ dans la solution extracellulaire. Nous observons des inhomogénéités spatiales attribuables à une distribution spatiale non uniforme et à une activité temporelle des canaux ioniques. Ces observations faites sans marqueurs et en temps réel sont les premières en date à ce jour.

Ces résultats démontrent que nous avons rempli notre défi initial. Avec le microscope développé au sein de notre laboratoire, nous avons montré les possibilités de visualiser, en temps réel, sans marqueur et avec une fluence faible, des changements structuraux neuronaux et l’activité neuronale électrique utilisant l’unique sensibilité intrinsèque des phénomènes non linéaires.

Mots clés:

Imagerie nonlinéaire, interaction membrane-molécule d'eau, cartographie spatiotemporelle, génération de deuxième harmonique, imagerie sans marqueur, activité neuronale, flux d'ions, potentiel de membrane

Content

Acknowledgements **i**

Abstract (English/French) **v**

List of figures **xiv**

List of tables **xvii**

Chapter 1: Introduction **1**

1.1 Neurons ... 3

1.1.1 Morphological aspects of neurons ... 3

The neuronal cytoskeleton ... 4

Microtubules nucleation, growth and dynamics ... 6

1.1.2 Electrical aspects of neurons ... 7

Transmembrane electrical potential and ionic flux ... 8

1.1.3 Metabolic activity ... 12

1.2 Imaging techniques for neuronal functions ... 13

1.2.1 Imaging the morphological aspects of the neurons ... 13

The static microtubule-based cytoskeleton ... 13

The dynamics of the microtubule-based cytoskeleton ... 15

1.2.2 Imaging the electrical aspects of the neurons ... 17

1.3 Nonlinear optical imaging ... 19

1.3.1 Two photon excitation fluorescence ... 20

1.3.2 Second Harmonic Generation ... 21

1.4 Principles of second harmonic generation ... 22

1.4.1 In non-centrosymetric structures ... 22

1.4.2 In voltage-sensitive processes ... 24

1.5 This thesis ... 24

Chapter 2: Experimental Details & Methodology **26**

2.1 High throughput wide-field second harmonic imaging for label-free biological imaging 27

2.1.1 Image throughput considerations 28

2.1.2 Imaging system and characterization 31

2.1.3 Imaging throughput measurements 34

2.1.4 Label-free SHG imaging of sub-cellular structures 35

2.1.5 Conclusions 37

2.2 Probing dynamics in living cells: translation and diffusion of $KNbO_3$ nanoparticles 37

2.2.1 Particle characterization 39

2.2.2 Translational diffusion of nanodoublers in water 39

2.2.3 Time resolved *in vitro* imaging 41

2.3 3D wide-field high throughput Second Harmonic imaging 44

2.3.1 Imaging system and characterization 44

2.3.2 3D imaging 47

2.4 Neuro-imaging 48

2.4.1 System and characterization 48

2.4.2 Patch-clamp equipment 50

2.4.3 Cell cultures protocol 52

2.5 Appendix 54

2.5.1 Particle characterization 55

2.5.2 Particle electroporation in HeLa cells 55

2.5.3 Particle tracking 56

2.5.4 Polarization measurements of fixed particles 57

2.5.5 Nanoparticles orientation analysis 58

2.5.6 Correspondence between the SLM period and the opening angle of the incident beams 61

Chapter 3: Mapping of morphological changes in the neuronal cytoskeleton with endogenous second harmonic imaging: a case study of nocodazole **63**

3.1 Introduction 64

3.2 Materials and methods 68

3.2.1 Nocodazole treatment 68

3.3 Results and Discussion 68
3.3.1 The orientational distribution of microtubules 68
3.3.2 SH imaging of microtubule morphology in single neuron 70
3.3.3 Mapping changes in the microtubule morphology as a function of maturity 71
3.3.4 *In vitro* SH imaging of multisite time-resolved microtubule morphology changes 72
3.3.5 Conclusions 75
3.4 Appendix 77
3.4.1 Relative variation of nocodazole-induced microtubules loss 77

Chapter 4: Probing neuronal morphology and metabolic activity with label-free SH polarimetry and endogenous 2PEF 79
4.1 Introduction 80
4.1.1 The different stages of the morphological development 80
4.1.2 Imaging the different stages of the morphological development 82
4.2 Results and Discussion 83
4.2.1 Stage 1 and 2, before the morphological differentiation 83
4.2.2 Stage 3, axonal branching 84
4.2.3 Stage 4, after the morphological differentiation 87
4.2.4 Comparison between the metabolic activity and structural changes throughout the whole morphological development cycle with 2PEF and SHG 88
4.3 Conclusions 90

Chapter 5: Membrane water as a probe for neuronal membrane potentials and ionic flux at the single cell level 92
5.1 Introduction 91
5.2 Materials & Methods 94
5.2.1 Image processing and data analysis 95
5.3 Results and Discussion 95
5.3.1 Comparing electrical and optical recordings 96
5.3.2 Membrane potential and ion flux imaging 97
5.4 Conclusions 100

Summary & Outlook **101**

Summary 101

Outlook 103

List of Figures

1.1: The different stages of neuronal morphogenesis in cultured neurons 4
1.2: The microtubules-based cytoskeleton structure and dynamics of mature neurons 5
1.3: The model of microtubules dynamics and length in cultured neurons as a function of maturity 7
1.4: The intrinsic membrane potential 8
1.5: The neuronal plasma membrane and principle states of ion channels 10
1.6: Two-photon action cross section and emission spectra from NADH and Riboflavin molecules 13
1.7: Different modalities to image the neuronal cytoskeleton 16
1.8: Schematic of the patch clamp whole cell procedure 17
1.9: 2PEF (two photon excitation fluorescence) and SHG (second harmonic generation) processes with their corresponding emission wavelength 21
1.10: The displacement of polarizable electrons in a non-centrosymmetric environment 23

2.1: Calculated imaging throughput 30
2.2: Optical layout of the high throughput wide-field SH microscope 32
2.3: Imaging chamber 33
2.4: Measured imaging throughput 34
2.5: Label-free TPEF and SHG imaging of living neurons 36
2.6: Transmission electron microscopy images and diffraction pattern of a single $KNbO_3$ nanoparticle 39
2.7: Principles of the method and translational diffusion of 100 nm $KNbO_3$ particles in water 40
2.8: Time resolved nanoparticle tracking 41
2.9: Spatial mapping of the rotational diffusion of 100 nm $KNbO_3$ nanodoublers inside a living cell 43
2.10: 3D wide-field Second Harmonic imaging system 44

2.11: Layout of the two incoming beams at the back focal plane of the objective and their configurations at the surface of the sample plane 45
2.12: Polarization configuration of the two incoming beams 46
2.13: Illustration of the 3D HiLo imaging process 48
2.14: Temperature control and constant flow equipment for live-cells imaging 49
2.15: Characterization of the temperature inside the open-bath chamber 50
2.16: 3D wide-field SH microscope and adapted patch-clamp equipment 52
2.17: Viability test 53
2.18: SH images from healthy cultured neurons (7DIV) and from dead neurons 54
2.19: Particle characterization 55
2.20: Two photon fluorescence and second harmonic confocal image stack of electroporated cells 56
2.21: Polarization characterization of the nanodoublers 57
2.22: Imaging configuration and SH intensity from the nanoparticles in the chamber 59
2.23: R^2 values for the rotational diffusion MSD analysis 60

3.1: The orientational distribution of microtubules from SH polarimetry 69
3.2: Effects of nocodazole on SH response from microtubules, during application and after washout 70
3.3: Nocodazole-induced SH intensity depletion from the cytoskeleton of neurons at different stages of maturity 72
3.4: Spatiotemporal SH imaging of microtubule stability 73
3.5: Schematic views of the variation of uniformly oriented axonal microtubules density as a function of time and exposure to nocodazole 77

4.1: Stages of development of primary cortical neurons in culture imaged with different modalities 82
4.2: Details of stage 1 and 2 of the neuronal development before the morphological differentiation 83
4.3: Cultured neuron at stage 3 imaged with PC, SHG, and 2PEF 85
4.4: Coefficient of polarization from a neuron at stage 3 of its neuronal development 86
4.5: Details of stage 5 of the neuronal development: from the dendritic outgrowth until the late stage of maturation, imaged with PC, SH, 2PEF and the corresponding coefficient of polarization (COP) 87

4.6: Quantitative comparison of the mean value of the 2PEF/SHG ratio and the standard deviation of the COP, from the cell body as a function of DIV..... 90

5.1: Second harmonic and electrophysiological response during a K^+-induced depolarization experiment..... 96
5.2: Spatiotemporal imaging of membrane potentials and ionic efflux by mean of the nonlinear optical response of water..... 98

List of Tables

1.1: Typical values of the intracellular and extracellular concentration of the most important ionic species in typical nerve cells 11

2.1: Correspondence between laser output power and the different energy distributions at the sample stage 61
2.2: Correspondence between the angle of the two incoming beams and the generated period on the SLM 63

"J'ai donc, hélas ! étudié la philosophie, la chicane et la médecine et, par malheur, même la théologie à fond ; avec un zèle ardent. Et me voilà, pauvre et sot que je suis, aussi avancé qu'auparavant ! J'ai titre de maître, voire de docteur, et voici bientôt dix ans que je tire à hue et à dia, à tort et à travers, mes disciples par le bout du nez – et je vois que nous ne pouvons rien savoir ! Peu s'en faut que le cœur ne m'en brûle. Certes je suis plus avisé que tous les pédants, docteurs, maîtres, scribes et clercs ; je suis indemne de scrupule et de doute ; je ne crains l'Enfer ni le Diable – mais en revanche, toute joie m'est ravie. Je ne m'imagine pas savoir quoi que ce soit de vrai, ne m'imagine pas pouvoir par doctrine améliorer et convertir les hommes. D'ailleurs je n'ai ni bien ni argent, ni les honneurs ou le brillant du monde. Pas un chien ne voudrait vivre ainsi plus longtemps."
(Goethe, Faust, 1808, p 4)

Chapter 1: Introduction

"In art, as in science, reductionism does not trivialize our perception – of color, light, and perspective – but allows us to see each of these components in a new way". With those words, Eric Kandel stresses the essence of scientific reasoning: the understanding of complex phenomenon is achieved by stepping back towards the identification of their fundamental mechanisms. This reductionism procedure is infinite, always revealing new complex phenomena. However, the quest of understanding is governed by intellectual questioning interconnected with technical challenges. For instance, one of the biggest intellectual questioning of all times is the understanding of the human brain, dating back to the 17th century BC where the first written reference of the brain was found in the Edwin Smith Papyrus, an Egyptian medical treatise. At that time technical advances only allowed the macro observation of the brain resulting in a quite poor understanding of its functions. Throughout the ages, besides close collaborations and interdisciplinary exchanges between anatomists, physicists, psychoanalysts, biologists and sociologists, advances in technology have proven invaluable in reductionism across multiple spatial scales: from the macro bulk observations to the discovery of single nerve cells in the late 19th century, revealing each time more intricate fundamental mechanisms and each time challenging our understanding of the brain. These neuro-anatomic cellular observations were made possible with new experimental capabilities brought about by inventions such as the microscope. During the 19th century, the improvement in light microscopy resolution together with the works of histologists and staining methods unfolded the physiology of the brain and resulted in the validation of the neuron doctrine, for which Golgi and Cajal received a shared Nobel Prize in 1906, testifying that the nervous system is composed of discrete individual cells with a cell body, an axon and dendrites.

After centuries of two-dimensional representation captured by microscopy, the 19th century started to reveal the dynamic function of the brain. The pioneer works in the field of electrical stimulation were done by two German doctors, Fritch and Hitzig. By this time, neurologists were mainly focused on histology and molecular processes, and physiologists and doctors were supporting the theory of the dynamic activity of nerve cells. Finally, Du Bois-Reymond, a German physiologist in the late 19th century, ceased the many-year conflict between the neurologists and physiologists. He demonstrated that the activity in a specific type of nerve cell was invariably accompanied by electrical activity. He

declared: “I have succeeded in realizing in full actuality the hundred years’ dream of physicist and physiologists, to wit, the identification of the nervous principle with electricity.” It was only 50 years after this finding that the first record of the electrical activity of the brain was made by Hans Berger, a German psychiatrist. The technical advances during the following decades contributed to the understanding of the electrical activity of neurons at a single cell level and within a larger network. The emergence of various techniques such as patch clamp, together with substantial improvements in microscopy, molecular biology, genetics and novel complex microscopic techniques lead to great discoveries on the sub-molecular and functional level. Nowadays the mechanisms at the origin of single-cell signaling are well studied. The nervous system is known to consist of billions of neurons that communicate between each other through complex series of biochemical and electrical processes: the dendrites integrate the signal received from nearby neurons with the reception of biochemical messengers, neurotransmitters released by presynaptic neurons, at targeted receptors. This action happens at the synapse, the communicating junction between two neurons. If the signals received overcome a certain threshold, an action potential will travel down the length of the postsynaptic axon to the terminus, resulting in the release of neurotransmitters into the synapse. To summarize, neuronal communication is made possible by the neuron’s specialized structure and biochemical mechanisms: the specific neuronal morphology and the selective transmembrane ionic fluxes through the permeable plasma membrane constitute two of the principal aspects of the neuronal signaling.

During the past decade, multiphoton microscopy has proven invaluable to the field of non-invasive bioimaging, however faces limits in term of technical advancements. In this thesis we propose a new optical layout for a nonlinear microscope and demonstrate the possibility of label-free imaging of neuronal structures and electrical neuronal activity employing the unique intrinsic sensitivity of nonlinear phenomena.

1.1 Neurons

1.1.1 Morphological aspects of neurons

Neurons are the functional units of the nervous system. A typical mature neuron is composed of a cell body (enclosing the nucleus, the organelles and subcellular components) and many neuronal projections. The term "neuronal projections", or neurites, refers to axons or dendrites emerging from the cell body. A typical mature neuron contains an axon and many dendrites made of filamentous cytoskeleton compounds responsible for the cell shape and organelles transport. Neurons are electrically excitable cells: they transmit information to each other by means of action potentials which are typically bursts of voltage variations and synaptic signaling processes, partly electrical and partly chemical.

Before becoming electrically active, neuronal cells undergo major developmental changes as they mature, develop specific projections, and establish active synaptic connections. Since most of the common understanding of the properties of developing neurites derives from studies of cells in tissues culture[1], this chapter will be focused on the morphological changes in cultured neurons. This simplification is validated since the biological mechanisms underlying the outgrowth processes are likely shared by most classes of nerve cells *in vitro* and *in vivo*[2].

During the first few hours following the postplating process and post-mitotic neuronal stage, neurons display early markers of structural differentiation (Figure1.1). Stage 1 of morphological neuronal development starts with the breakage of the roundish membrane symmetry entailed by the growth of continuous projections, the lamellipodia. After few more hours, stage 2 occurs when lamellipodia evolve in sparse protoprocesses at the periphery of the cell body. Stage 3, which occurs after one day in culture, begins with the axonal outgrowth. At this stage, one of the minor processes demonstrate a burst in growth and can extend up to several micrometers. During this outgrowth, the axon can develop many collateral protrusions. This axonal branching plays a crucial role in the inspection of the cells' surroundings. Compared to the shape of the other minor neurites, this young axon's shape is rather slender and exhibits specific axonal terminaisons: the growth cones. Composed of various filamentous materials, these distal axonal tips are also involved in the exploration of the cell's environment. The growth cones probe their surrounding by extending and retracting their peripheral regions, either in a tapered finger-like projections, called filopodia or in flat sheet-like membrane protrusions, lamellipodia[3]. Dendritic differentiation and outgrowth begins only at stage 4. Dendrites extend with filamentous-based structures like growth cones, leading the way to network exploration[4].

At this point the neuron is morphologically polarized and exhibits a dendritic branching profile with one long thin axon emanating from the cell body. The last stage of neuronal development, stage 5, is the maturation. At this step, we can observe the proliferation of branching sites on the dendrites with the appearance of dendritic spines, membranous protrusions participating in synaptic communication. Dendritic spines are highly dynamic with a relatively rapid turnover and are able to adjust to their close environment by changing their shape and localization. Dendritic spines represent one of the active components involved in the learning and memory processes, which define synaptic plasticity[5]. Once the establishment of the morphological polarization is set with mature synapses and dendritic arborization, signaling within neuronal networks is possible.

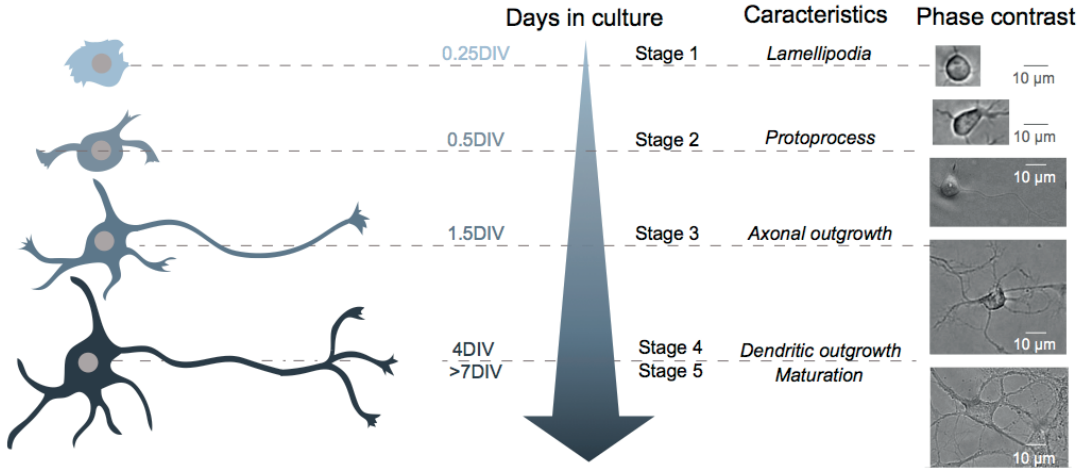

Figure 1.1: The different stages of neuronal morphogenesis in cultured neurons. The first column are schematics of the neurogenesis stages: from the post-mitotic stage (top row) to maturation (bottom row), their corresponding ages and stages and their specific characteristics. The last column represents the phase contrast images of the corresponding stages.

The neuronal cytoskeleton

The cytoskeleton morphology (Figure 1.2a) and the underlying structural organization of dendrites and axons is crucial for the functional integrity of electrical signaling. The cytoskeleton network of the neuron is made of microfilaments, intermediate filaments and microtubules. This filamentous structure provides the cell its ability to maintain its shape and electric properties. In this thesis, we will mainly focus on the microtubules, that constitute one of the major compounds of the neuronal cytoskeletal network (Figure 1.2b). They play an essential role throughout morphogenesis and during the construction of the cytoplasmic structures[6]. Microtubules are hollow cylinders 25 nm in diameter, formed by lateral interactions of 13 protofilaments. Composed of α/β-tubulin dimers, they exhibit an overall structural non-centrosymmetry, with an exposure at the extremities of either an α (minus-end)

or β (plus-end) tubulin ring (Figure 1.2b)[7,8]. The structural organization and dynamic remodeling of microtubule arrays differ in mature axons and dendrites (Figure 1.2c). In axons, microtubules are uniformly oriented and form tight bundles with their plus-end distal from the cell body[9]. In contrast, a mixed polarity orientation is observed in dendrites[10–12]. The difference between dendrites and axons differs also in their content of organelles and proteins[13]. Therefore, it's important to understand the mechanisms involved in the healthy establishment of complex cytoskeleton organization, stability factors and dynamics, as microtubule defects lead to abnormal neurodevelopmental disorders and neurodegenerative disease such as Alzheimer's disease, Parkinson's disease or Hereditary Spastic Paraplegia[14].

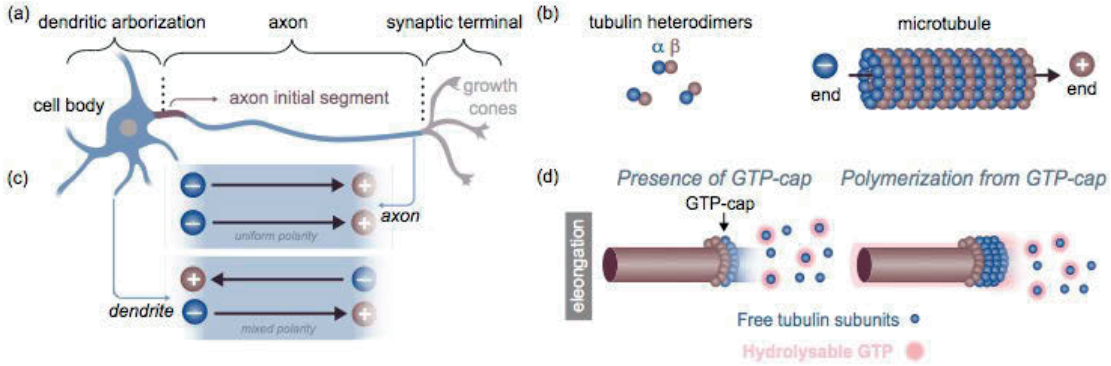

Figure 1.2: The microtubules-based cytoskeleton structure and dynamics of mature neurons. (a) In mature neurons, dendrites are formed from the basal neuronal area, and axon constitute the elongated projection from the cell body toward the apical aspect of the neuron. The axon initial segment constitutes the most proximal part of the axon that terminates into the synaptic terminal in the most distal part. (b) One of the components of the neuronal cytoskeleton is the microtubule (MT), made out of α/β-tubulin heterodimers. (c, top panel) In the axons of mature neurons, microtubules are oriented in a uniform array with their plus-end distal from the cell body, (c, bottom panel) while the dendrites of mature neurons present a mixed polarity of microtubules. (d) Polymerization and elongation mechanisms of the microtubule explained with the GTP-cap model.

Microtubules nucleation, growth and dynamics

Microtubules polymerize from α/β-tubulin nucleation seeding processes. *In vitro*, spontaneous nucleation is observed above a certain tubulin concentration threshold[15]. In neurons, the tubulin concentration is too low and microtubule polymerization requires several structural and cellular factors acting as nucleators[16]. In the early stages of neuronal development, nucleation occurs at a specific microtubule-organizing center (MTOC), the centrosome. The centrosome is a small spherical structure that comprises a central pair of cylindrical tubulin-made cell structures, the centrioles,

surrounded by the pericentriolar material, an amorphous mass of proteins[17]. The activity of the centrosome silences after neuronal differentiation[18], and nucleation activity appears to be associated with other sites, such as cellular organelles that function as a MTOC[19]. The nucleation mechanisms of non-centrosomal microtubules have been studied for decades, however, this topic remains highly controversial and not fully understood[20]. After the early stage nucleation, microtubules are spatially distributed within arrays of specific geometry as mentioned in the previous section. This structural arrangement is achieved with the regulation of newly polymerized microtubules by controlling their sliding, elongation, stability, transport, bundling and severing[21].

Microtubules are highly dynamic versatile structures[22–25]. Besides spatial displacements, microtubules undergo intrinsic stochastic instabilities[22]: the interconversion between catastrophe and rescue events. Catastrophe is defined as the transition between the polymerizing state to the β-tubulin depolymerizing shrinking state, and rescue is associated with the reversal process. The plus-end of the microtubule, exhibiting a labile behavior, endures series of catastrophes and rescues, while the minus-end remains more stable. Within both dendrites and axons, labile and stable microtubules are found, with a greater number of stable microtubules in axons compared to dendrites[26,27]. At early stages of neuronal development, a higher concentration of labile microtubules is found in minor processes and in the growth cones, whereas stable microtubules predominate in the proximal part of the axon with a decreasing stability gradient towards the axonal shaft[13,28]. As the neurons mature, microtubules are more inclined to collect post translational modifications (PMT) resulting in an increase of stability[13,29]. The origin of instabilities within microtubules has been explained as successive events of binding and hydrolysis of guanosine triphosphate (GTP) to guanosine diphosphate (GDP) by the α/β-tubulin dimers[22,30]. However, the precise mechanisms involved in the microtubules elongation and stability differences remain a controversial topic for which several models have been proposed. One of the most common models has been the existence of a GTP-tubulin cap ring at the extremity of the microtubule plus-end to prevent its total depolymerization and promote its elongation[31] (Figure 1.2d). This model suggests a polymerization from an existing microtubule, with the stable plus-end serving as a seeding site for nucleation[32] which does not satisfy all the neuro-biology community. Another contentious subject is the microtubules' length[33] and their stability. Despite technical and intellectual advances in the field of imaging and neuro biology, little is known about the precise size, and model dynamic of microtubules within neurites[33]. Figure 1.3 summarizes the "up to date" model of the microtubule-based cytoskeleton.

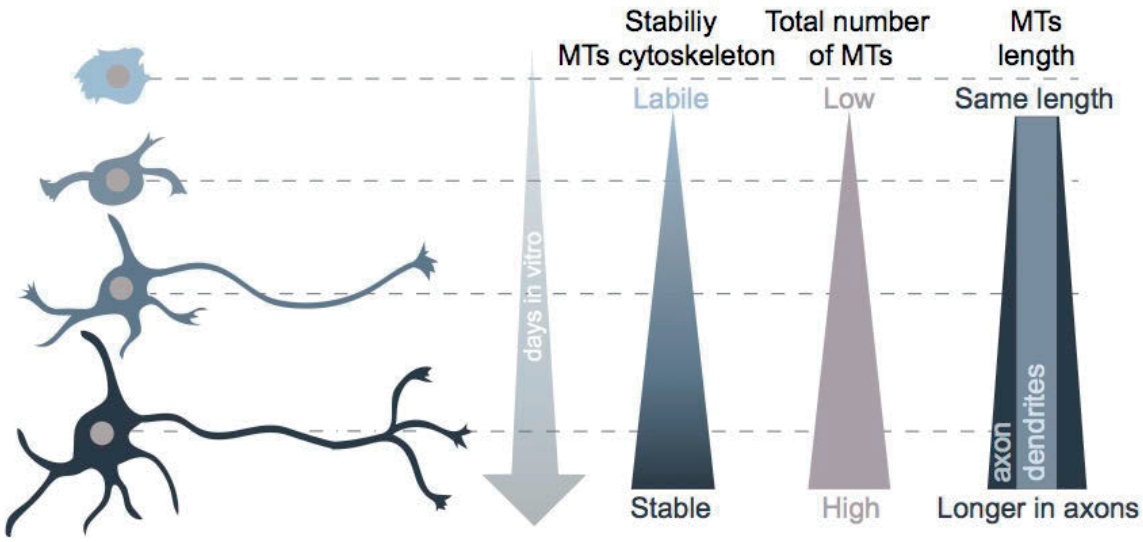

Figure 1.3: Model of microtubules dynamics and length in cultured neurons as a function of maturity. The number of microtubules and their stability increases as the neuron matures. The length of the microtubules, following their centrosomal nucleation and severing from the centrosome, remains a controversial topic. However, evidence of length diversity in dendrites and in axon has been demonstrated with immunostaining and other imaging techniques reviewed in detail in the next part.

1.1.2 Electrical aspect of neurons

The reception and gathering of incoming synaptic signals from other nerve cells is established through the mature dendritic branches sprouting from the cell body. These inputs are integrated at the origin of the axon, (the axon initial segment) and conducted along the axonal structure towards the sites of synaptic interactions at the terminus. Electrochemical and physical-chemical principles govern the electrical activity of neurons: the maintenance of ionic concentrations gradients from the extracellular and cytoplasmic compartments across the plasma membrane underpin the basics of the transmembrane potential (Figure 1.4a-b).

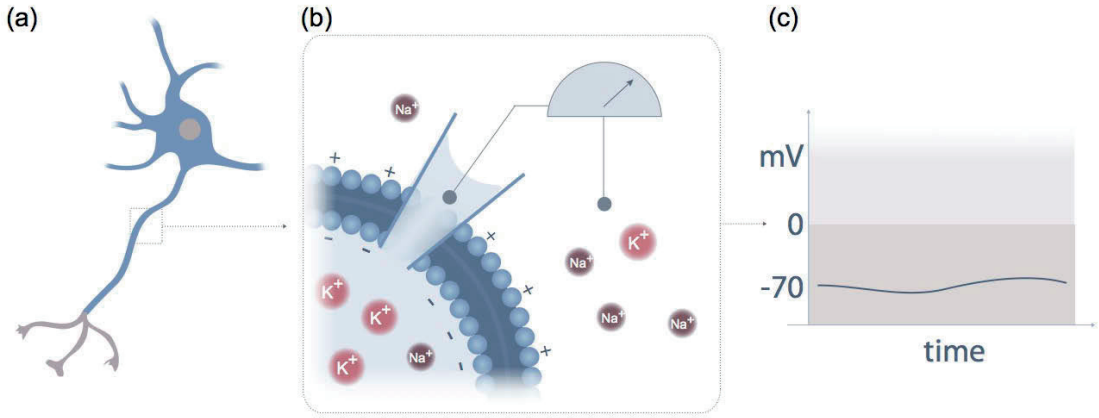

Figure 1.4: The intrinsic membrane potential. (a) In a typical neuron, a high concentration of potassium is found inside the cell and a high concentration of sodium is found in the extracellular space. (b) The resulting membrane potential across the plasma membrane can be measured with an electrode inserted into the cell and a reference electrode in the extracellular space. (c) At rest, the concentration gradient of different ionic species and the separation of charges by the plasma membrane induced an intrinsic resting membrane potential of around -70 mV.

Transmembrane electrical potential and ionic flux

Neurons are electrically active cells, even at rest they exhibit an intrinsic difference of voltage typically found around -70 mV[75] (Figure 1.4c). Changes in the resting membrane potential are measured when the neurons are exposed to external stimuli. Different types of neuronal electrical signals are observed for different types of neurons. For instance, a brief touch would activate the receptors of a sensory neuron, an activation of synaptic events from hippocampal pyramidal neurons would trigger a synaptic potential, or an action potential would be produced in a spinal motor neuron after stimulation of a spinal reflex. All these events are accompanied by a brief change in the resting membrane potential. Depolarization is defined when the potential of a nerve cell becomes more positive than its resting membrane potential, and hyperpolarization is the event in which the membrane potential becomes more negative. During depolarization, a certain threshold potential can be overcome resulting in a 1 ms transient burst of voltage that abolishes the negative resting potential and makes the transmembrane potential positive. Because neurons are relatively poor conductors this booster is needed to transmit information over long axonal distances: it is the principle of the action potential. All these electrical processes originate from ionic movements across a versatile permeable plasma membrane.

The plasma membrane is a permeable 5-nm-thick lipid bilayer structure maintaining a separation of ionic charges between the interior and exterior of the cell. However, upon external excitation (chemical, electrical or ligand-triggered), the permeability of the plasma membrane changes, allowing transmembrane ionic fluxes through selective ionic channels. Ion channels are most obvious as the fundamental excitable elements in neuronal signaling. Ionic mechanisms have been recognized since the 19th century as the key components in the excitability properties of nerve cells. The first scientist at the origin of this discovery, Sidney Ringer, demonstrated that, in order to maintain a heart beating from a frog's dissection, the perfusion solution in which the heart was immersed must contain sodium (Na^+), potassium (K^+) and calcium ions (Ca^{2+}). The later works of Walther Nernst (1888) and Julius Bernstein (1902) brought substantial contributions to the establishment of the "membrane hypothesis". In this model, the neuronal plasma membrane was selectively permeable to K^+ ions at rest and the permeability to other ions increased during excitation. This hypothesis also explained the tendency of the diffusion of positively charged ions to drop down their concentration gradient. This model evolved in a quite good up-to-date understanding of the ionic fluxes, ion channels roles and other transporters that rule the electrical signaling. The principal ions responsible for the majority of the electrochemical signaling are Na^+, K^+, Ca^{2+} and chloride (Cl^-). Those ions travel across the plasma membrane through selectively permeable ion channels, which are protein chains shaped as ionic pores embedded in the plasma bilayer lipid membrane (Figure 1.5a). A large variety of ion channels exist: they can be ligand-gated, voltage-gated or activated by neurotransmitters. Their gating response consists of a binary closed and opened state (Figure 1.5b). When opened, an ion channel has a selective permeability which allows only certain type of ions to go through down their electrochemical gradient. The rate of ionic transfer can reach 10^6 ions per second, resulting in a high throughput rate in the electrical response of neurons.

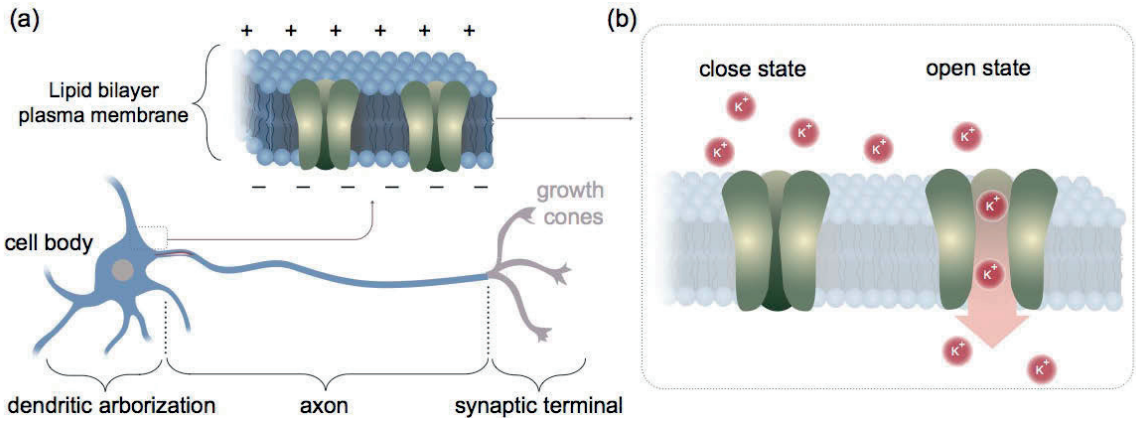

Figure 1.5: The neuronal plasma membrane and principle states of ion channels. The neuronal plasma membrane and principle states of ion channels. (a) The plasma membrane is made out of a bilayer lipid membrane. Due to proteins at the surface of the cell membrane, the exterior is positively charged in comparison to the interior. (b) Ion channels are embedded in the lipid bilayer plasma membrane and selectively let through ions (in this example from outside to the inside) by means of a dual quantal open or closed state.

In the last section, we show that a change in the membrane permeability by means of ion channels has a direct influence on the neuronal membrane potential. Additionally, the concentration gradients of the different ionic species present inside and outside the cell and the separation of charges across the membrane play a crucial role in the establishment of the membrane potential. Indeed, transmembrane ionic movements through ion channels are subject to two forces: the chemical driving force and the electrical driving force. The chemical driving force depends on the concentration gradient of a specific ion across the membrane. For instance, in neurons, a higher concentration of K^+ is found inside the intracellular space resulting in a constant efflux of K^+ outside the cell down to its concentration gradient. The electrical driving force is a function of the electrical potential difference across the membrane, by convention the inside of the cell is considered as a reference point. Those two forces are related since the greater the efflux of K^+, the more charge separation and the greater the potential difference. A balance between those two forces is needed to establish the resting membrane potential. The equilibrium potential for each ion taking into account their specific concentrations inside and outside the cells is calculated with the Nernst equation:

$$E_X = \frac{RT}{zF} ln \frac{[X]_o}{[X]_i}, \tag{1.1}$$

R is the gas constant, T the temperature (in Kelvin), F the Faraday constant, and z the ionic charge. $[X]_o$ and $[X]_i$ defines the concentration of the ion X outside and inside the cell, respectively.
The Nernst equation is used to find the equilibrium potential of any ions present inside and outside of cells. The respective concentration on both sides of the plasma membrane for the most important ionic species in neurons are summarized in Table 1.1.

Ionic species	Intracellular concentration	Extracellular concentration	Equilibrium potential
K^+	145 mM	5 mM	-96 mV
Na^+	15 mM	145 mM	+60 mV
Mg^{2+}	0.5 mM	1 mM	+9 mV
Ca^{2+}	70 nM	2 mM	+137 mV
Cl^-	10 mM	110 mM	-64 mV

Table 1.1: Typical values of the intracellular and extracellular concentration of the most important ionic species in typical nerve cells. These values are found here with their corresponding equilibrium potential derived from the Nernst equation.

As mentioned earlier, the membrane potential of a nerve cell is a function of the concentration of the different ions and their ability to cross the plasma membrane. This ability, called permeability is proportional to the number of open ion channels and to their respective specific conductivity. A correct estimation of the general value of the membrane potential is given by the Goldman Hodgkin and Katz (GHK) formula. The GHK formula is a more complete version of the simplified single-ion Nernst equation, in which the concentrations of the ions are weighted in proportion to the relative magnitudes of their permeability constants:

$$V = 58\ log \frac{P_K[K]_{out} + P_{Na}[Na]_{out} + P_{Cl}[Cl]_{in}}{P_K[K]_{in} + P_{Na}[Na]_{in} + P_{Cl}[Cl]_{out}} \quad (1.2)$$

V is the voltage across the membrane and P_K the permeability of the membrane to a specific ion. For instance, if a membrane potential is found to be close to the equilibrium potential for [K^+], it implies that the resting membrane would be most permeable to [K^+], which is the case for neurons. At rest, the electrical equilibrium is maintained by a constant K^+ efflux, the resting membrane being more permeable to K^+. These active transporter-dependent concentration-gradients are at the origin of the resting neuronal membrane potential and action potentials.

It is thus possible to estimate the membrane potential of a cell, based on the extracellular and intracellular ionic concentrations and their respective permeability. When the extracellular concentration of the K^+ changes, the gradient concentration from inside the cell towards the outside changes and the membrane potential becomes less negative (i.e. the depolarization process). Hodgkin and Katz carried out this experiment back in 1949 and stressed the importance of the multiple permeabilities of the cell membrane.

1.1.3 Metabolic activity

Endogenous 2PEF intensity have been observed in neurons and has been interpreted as a marker of metabolic activity[34–36]. On a metabolic point of view, neurons have the highest energy demand in the brain compared to other cells[37]. From growth to maturation, a specific developmental sequence of precise regulatory mechanisms is required to control the neuronal life cycle. Cellular metabolism plays an important role into the neurogenesis, which is functionally coupled to the activity of a

specific metabolic program[38]. Maintenance and restoration of ion gradients, mainly responsible for the electrical activity of neurons and reviewed in the previous section, are the main cause of neuronal energy need[39]. Also, the cytoskeletal dynamics requires energy[40]. In neurons and other cells, the energy need is covered by adenosine triphosphate (ATP), a molecule that delivers energy upon hydrolysis so that it can be used to drive endothermic chemical reactions. Mitochondria are organelles, roughly 1 micron in size that are present in every cell and are responsible for the synthesis of ATP that occurs through the oxidative phosphorylation cycle.

For endogenous 2PEF studies there are two relevant molecules in the electron transport chain (ECT) that are part of the oxidative phosphorylation cycle that leads to the final product of ATP, namely flavin adenine dinucleotide (FAD) and reduced nicotinamide adenine dinucleotide (phosphate) (NAD(P)H)[41]. In morphologically polarized neurons and during a depolarization process, electrical triggering (by neurotransmitters binding or following a depolarization induced by a change in the extracellular potassium concentration) the mitochondria become active and redox mechanisms occur, leading to a quick short-term increase in the oxidation of (NADH or FAD) followed by a long-lasting reduction. Studies of cellular fluorescence[274] showed that the reduced form of the coenzyme NADH is fluorescent while its oxidized counterpart is not (NAD+) and that the oxidized form of FAD (FAD+) is fluorescent (excitation 450-500 nm, emission 520-590 nm) while its reduced form is not (Figure 1.6a-b). Considering the emission spectra and the excitation cross section of NADH and FAD proteins (Figure 1.6a-b), an emission around 515 nm is more likely to highlight the emission of NADH, which stresses the metabolic activity of mitochondria in cells.

Additional endogenous 2PEF imaging studies haves also shown that neuronal differentiation is associated with an increased mitochondrial biogenesis[42] and that mitochondrial morphology and trafficking vary as a function of the neuronal differentiation stages[43].

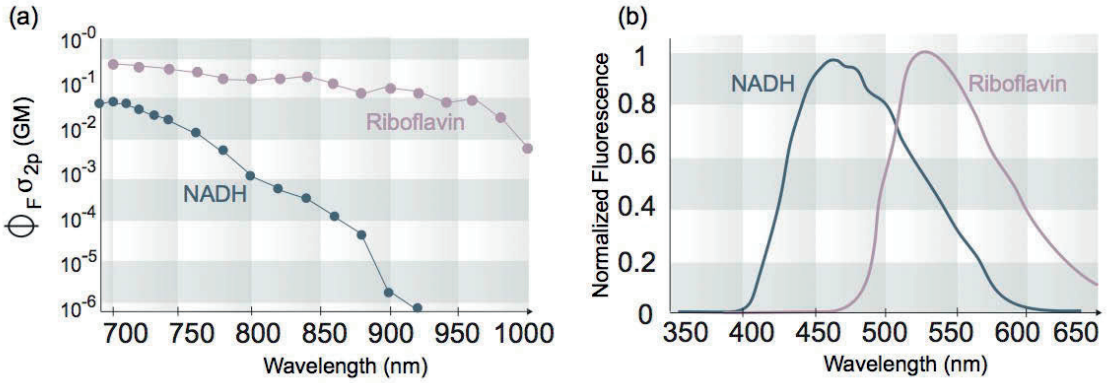

Figure 1.6: Two-photon action cross section and emission spectra from NADH and Riboflavin molecules. Graphs are taken from[36].(a) Absorption cross-section of NADH and Riboflavin, two biological molecules

contributing to the intracellular 2PEF endogenous fluorescence. (b) Emission spectra of NADH and Riboflavin measured in the same conditions as in (a).

1.2 Imaging techniques for neuronal functions

1.2.1 Imaging the morphological aspects of the neurons

The static microtubule-based cytoskeleton

How the microtubules orient themselves and establish the neuronal cytoskeleton has been a longstanding question in cellular neuroscience. The structural organization of microtubules in axons and dendrites is crucial for the functional integrity of electrical signaling and visualizing the underlying structure of the neuronal cytoskeleton is of great importance.

The external morphological differences of axons and dendrites have been observed with white light microscopy: axons are rather thin and smooth structures whereas dendrites are tapered and arborizing in mature neurons. Later, the technical improvements in electron microscopy (EM) and staining protocols revealed another difference between dendrites and axons: their complements of cytoplasmic organelles[44]. EM is a widespread imaging technique in neurobiology. The technique consists of an electron beam and sets of magnetic lenses to create an image of the specimen. Often coupled with histological staining, a process in which different cellular constituents are colored with specific dye molecules, this microscopic technique offers a better spatial resolution compared to conventional white light microscopy. The spatial resolution of an EM is a function of the size of the electron spot and depends on both the wavelength of the electrons and the optical components than form the electron beam. Taking into account the limiting aberrations of the system, the spatial resolution can reach up to 50 pm[275]. EM has its limits, it still requires thin, dried and specifically stained or coated samples to image, making it inapplicable for *in vivo* imaging. Only later, the structural underlying composition of dendritic and axonal cytoskeleton was questioned and with the advances in the field of cell fixation and high-resolution EM, the filamentous substructures of the cytoskeleton and microtubules was observed[45].

The polarization of the microtubule was first identified with the “Hook method” (Figure 1.7a). In this method, the cell is immersed in a specific solution to cause permeability and depolymerization of the microtubules, then the addition of exogenous tubulin, results in adsorption of the additional tubulin to the existing microtubules, forming hook-like appendixes. Then dendritic or axonal cross sections are fixed and analyzed with EM. The EM images reveal different chirality of the individual hooks: the number of hooks with a clockwise direction corresponds to the number of plus-end microtubules

pointing out of the cross-sectional plane and *vice versa*. With this method, the mixed microtubule polarity in dendrites and uniform polarity in axons was established[46].

Around the same time, the question of microtubules length was rising. The first study was performed with serial-section EM[32,47,48] in which series of thin cut stained sections are juxtaposed resulting in a serial reconstruction of the specific neurites (Figure 1.7b). A wide diversity of microtubules length in different species and throughout the neuronal developmental stages have been reported[47,48]. More recent advances in transgenic manipulation conjugated with fluorescence microscopy or super resolution techniques (Figure 1.7c) coupled with single particle tracking[49–51] brought new insight into the size estimation of microtubule but still remains a fully non-resolved topic.

Even though EM reconstruction and Hook methods have proven valuable into the revelation and understanding of the microtubules organization, polarity and length, they remain unprecise and highly invasive: the fixation protocol is not suitable for *in vivo* analysis, the harsh nature of fluorophores can lead to disruption of the fragile cytoskeleton substructures[52,53] and the methodology often remains complex. Even with advances in less-invasive fluorescence microscopy and labelling, due to the tightly packed cytoskeleton, the specific fluorophores are challenging to identify for a defined class of proteins and compounds and the diffraction limit can lead to bias in image interpretations. In this prospect, super resolution is a promising alternative but is still subject to fixation artefacts[54,55].

The dynamics of the microtubule-based cytoskeleton

Identifying the cytoskeleton organization was not the only challenge for scientists. Soon, real time imaging of the evolution and dynamics of the cytoskeleton became a growing interest in the biologist community. The dynamics of microtubules *in-vitro* was first tracked in 1986 with dark field differential interference contrast microscopy[56]. Invasive techniques using immuno-electron microscopy and fluorophore-tagged proteins have also been used to visualize intrinsic and induced microtubule turnover[16,57–60]. More recently optogenetic modifications or cloned proteins expression in mice[61] and differential interference contrast imaging methods[62] have also been used for the investigation of the microtubules instabilities. A common method consists of tagging the tip of the dynamically assembling microtubule (+TIP) with specific fluorophores in combination with a tracking method in fluorescence microscopy[63] (Figure 1.7d-e).

Another common approach to measure the dynamics of the microtubules consists in the use of a variety of drugs that affect the α/β-tubulin dimers and the processes of GTP binding in combination with imaging techniques. In this respect, nocodazole, which reversibly interrupts the microtubule polymerization behaviour[64] is suitable to induce instability and to probe microtubule regulation

mechanisms. Those drug-triggered techniques coupled with spectroscopic measurements[64] , or immunostaining fluorescent methods[65,66] offers insight into the understanding of the microtubules dynamics[67].

However, as it is the case in the measurement of microtubules length, the necessity to tag the microtubules with a label has disadvantages: the difficulty to attach the label specifically and permanently to microtubules, the photo instability induced by the use of a fluorophore, and the harsh interaction of the fluorophore on the chemical reaction of interest[65,68]. In addition, genetic manipulation or differential microscopy have disadvantages from a clinical perspective or have a lack in component specificity. An alternative to image the microtubule-based cytoskeleton has been recognized and demonstrated in the form of second harmonic microscopy (SH)[69–71] but owing to the inherently weak optical process of non-linear process, recording times per image are long, and photo toxicity is high[72]. The basics principles of nonlinear optics will be explained in the next sessions.

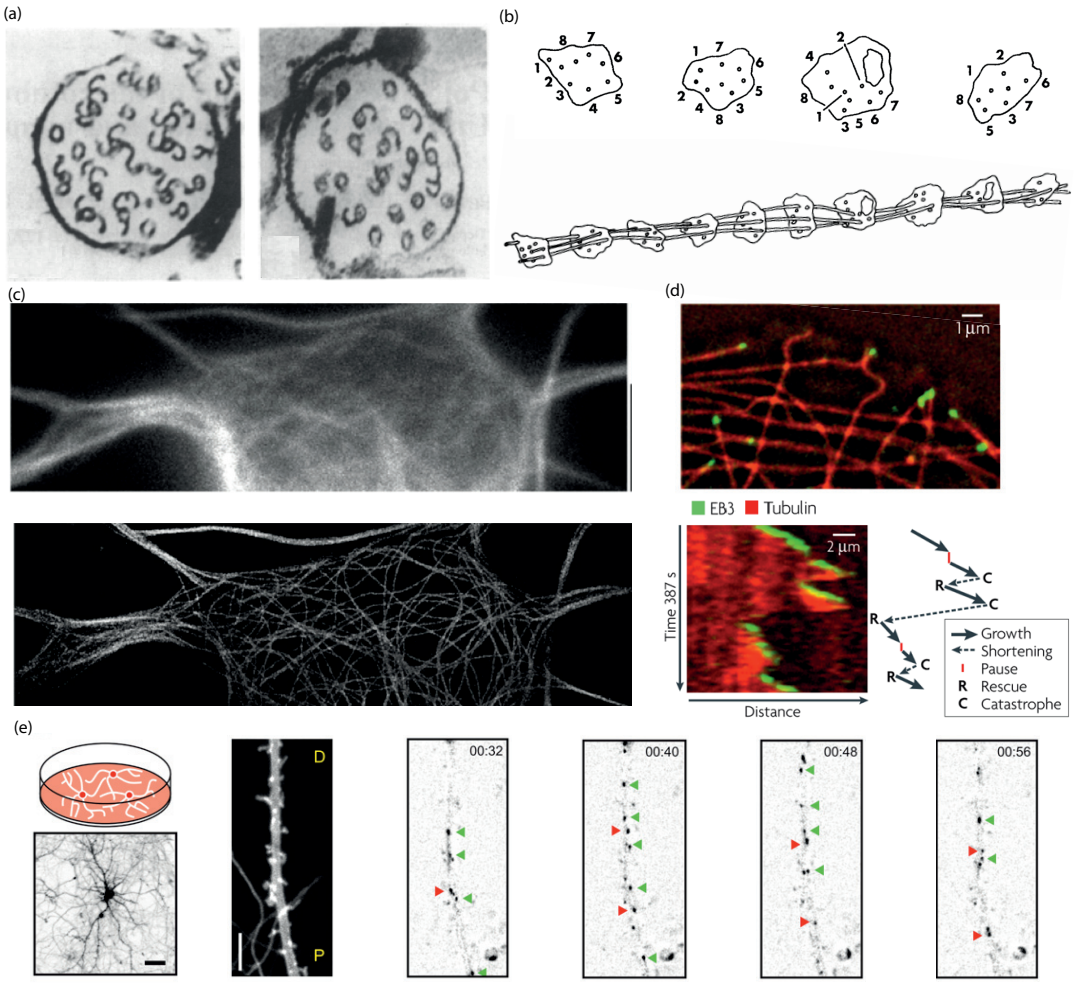

Figure 1.7: Different modalities to image the neuronal cytoskeleton. (a) Hook method illustrated with electron micrographs of dendritic (left) and axonal (right) cross-sections from[73]. (b) Serial reconstruction analysis of microtubules in cultured rat sensory axons showing the position and length of four microtubules through 6 µm distance, from[47]. (c) DIV5 neurons stained for tubulin and imaged with white light microscopy (top) and single-molecule localization super resolution microscopy (bottom), from[12]. (d) Visualization of microtubules of human lung fibroblast from live images, expressing the +TIP EB3 protein conjugated with mCherry-a-tubulin fluorophores (left) and a kymograph showing different phases of microtubule dynamic instability, from[74]. (e) Mixed dendritic microtubule organization from cultured rat neurons, transduced with GFP-MT+TIP fluorophore. The green arrowheads point to individual anterograde moving GFP-MT-+TIP comets and the red arrowheads to retrograde moving comets, from[12].

1.2.2 Imaging the electrical aspects of the neurons

Measuring neuronal electrical activity in cells in-vitro and in real time is a challenging task that follows two main approaches[72]: electrophysiological and optical.

Electrophysiology is the study of electrical signals of nerve cells. The most common electrophysiologist approach is the patch-clamp technique developed in the late 1970s and for which Neher and Sakmann received the Nobel Prize in 1991. This technique consists of measuring the

electrical neuronal activity with a microelectrode enclosed in a micropipette filled with highly conducting solution, similar to the intracellular solution, to record the voltage difference between the inside and the outside of the nerve cells. The whole setup is connected to an amplifier to record electrical nerve signals (Figure 1.8a). This micropipette is attached to the membrane of the nerve cell with the whole-cell technique: a seal is formed between the pipette and the broken cell membrane, opening access to the inside of the cell (Figure 1.8b). Two types of recordings are possible: current clamp, a technique that consist of injecting a current to the cell and recording the voltage and voltage clamp, with injection of a voltage and recording of current trace[75].

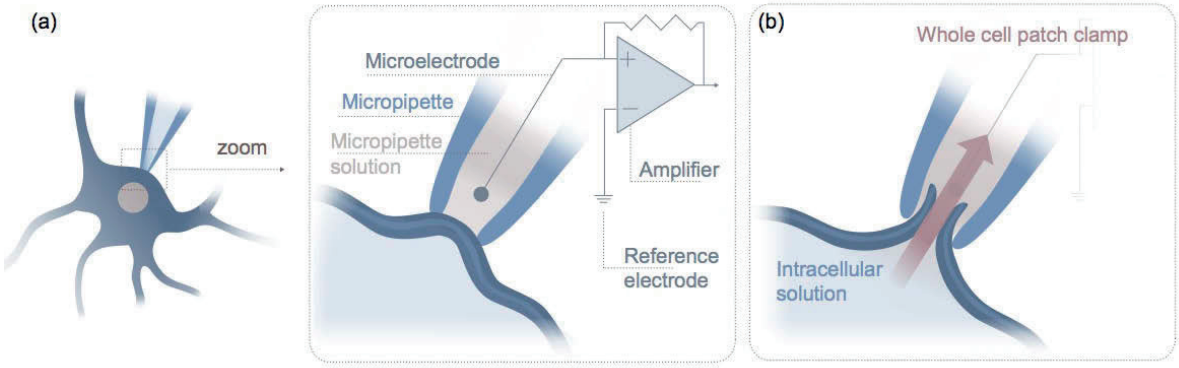

Figure 1.8: Schematic of the patch clamp whole cell procedure. (a) A glass pipette with a very small opening is put in direct contact with the cell membrane. This pipette contains a solution with a microelectrode connected to a differential amplifier. (b) Upon a suction, the membrane breaks creating a direct opening to the interior of the cell and the intracellular solution. The whole cell patch clamp consists in recording the current over the membrane of the entire cell.

Patch clamps have brought a breakthrough in the understanding of neuronal activity[76]. Nevertheless, patch-clamp techniques are highly invasive, harmful for the cells and are clinically inapplicable. Patch clamp measurements rarely exceed the time scale of several minutes and are limited to the soma (dictated by the size of the pipette and the neuronal structures). Recent improvement schemes using chronic implants can reduce these effects[77].

Because of the complexity of the experiments and the needs of highly sensitive equipment and skills, the development of optical methods brought interests to the physiologists and neuroscientists community. One of the advantages of the optical methods was the possibility to access information at a larger scale than a single cell and permits multisite recordings. First, scientists were looking at indirect signals that accompanies action potentials, such as birefringence or light scattering[78]. These signals were relatively low and means of detection not clearly optimized yet, resulting in long time averaging and bad signal to noise ratio. Even though improvement was needed, the 1970s expressed a real emergence about the idea to use optical signals to measure the electrical activity of nerve cells.

During the next decades, the discovery of fluorescent indicators brought significant advances in the improvement of time resolution and averaging reduction.

Nowadays, the use of ion sensitive dyes to monitor specific intracellular and extracellular concentration changes linked to electrical activity is widely spread. One of the main approaches is the use of calcium sensitive dyes[79] together with the detection of changes in the one or two photon fluorescence emission[80,81]. However, due to the slow temporal reactivity of the calcium sensitive dyes to the electrically-related changes of the membrane potential, the lack of sensitivity to small subthreshold events and the saturation effects of high-affinity calcium indicators, new techniques were required. Voltage sensitive dyes with their high sensitivity, their direct voltage specificity and high temporal reactivity were the answer to read out the whole neuronal electrical activity. The principle of the voltage sensitive dyes is to bind to the external surface of the plasma membrane and act as molecular transductors. Upon an excitation with the appropriate wavelength, the dyes emit fluorescence signals that are function of the membrane potential variations[82]. The mechanisms at the origin of the optical signals emission can be of diverse origin, such as the reorientation of the fluorophore embedded in the plasma membrane, electrochromic or electro-optical processes, or even transfer of energy from interactions among chromophores. Even if the voltage sensitive dyes technique brought significant advances in the measuring membrane potentials, the lack of binding specificity of fluorophores to the membrane and localization error of voltage probes remain still an unresolved problem. Moreover, the lack of sensitivity in the detection of the few emitted photons often results in either a too high increase in the power of the light source, or a too long time averaging leading to a consequent photodamage. Alternatively, labelled resonant non-linear optical approaches coupled with membrane and potential sensitive fluorescent labels have been used to image membrane potentials[83–86] whereby the optical response was correlated to the reorientation of the chromophore in the membrane[83]. Membrane potential sensitive chromophores can significantly alter the electric property of the membrane and modify the normal physiological behavior of the cell can be instable and toxic[87] therefore severely limiting the applicability of the methods[72]. To solve those nontrivial problem, other techniques emerged such as optogenetic[88,89] and interferometric microscopy in concomitance with immunostaining[90,91].

Fluorescent labelled imaging techniques offer a variety of dyes adapted for specific measurements. However, there is always a trade-off either in the temporal reactivity, photo toxicity or inherent specificity. The technical advances in optical light sources, data analysis and digital image enhancement have further broadened the applications in which fluorescent imaging can be applied and the possibilities to develop label-free imaging techniques.

In this sense, multiphoton microscopy and two-photon microscopy are promising tools in which the autofluorescence of naturally available endogenous fluorophores is detected in a label-free way. Recent works with other label-free techniques, stimulated Raman spectroscopic imaging, has shown promising results in relating spectral C-H stretch bands to membrane potential changes in erythrocite ghost cells but at this stage the connection between the Raman shift amplitudes and the membrane potential is still empirical[92].

1.3 Nonlinear optical imaging

Multiphoton microscopy (MPM), or nonlinear microscopy, is an imaging technique taking advantages of the nonlinear interactions between photons and matter. The diversity of nonlinear optical processes results in a variety of modes of contrast, the most commonly used being the multiphoton excitation processes of exogenous or endogenous fluorophores. In this section, we will focus on the two-photon processes such as two-photon excited fluorescence (2PEF) and second harmonic generation microscopy (SHG). The technical requirements, advantages and limits of 2PEF and conventional SHG techniques will be detailed.

The pioneer works in the theoretical prediction of non-linear optical processes went back to 1930s with the works of Maria Göppert-Mayer. Her contribution in the nonlinear optics field was so important that her name Göppert-Mayer, "GM", was used to as a unit to define the probability of a two-photon absorption event occurring in a fluorophore (1 GM = 10^{-50} cm^4 s/photon). At this time, the experimental demonstration of non-linear phenomena was not possible yet because of the high power needed to induce non-linear optical effects in matter. Thirty years after, the development of the laser[93] opened up the possibilities to further experimental works in the realm of non-linear optics. The first nonlinear microscope was developed in 1974 and the first experimental application was the observations of specific structures of single-crystal platelets, non-visible with conventional polarizing light microscopy[94]. After this time MPM, with its ability to observe biological processes and its deep penetration depth, gained more popularity in the field of bio-imaging. Nonlinear optical effects occur when the strong electric field of an excitation source polarizes the electrons in such a way that their behavior becomes non-harmonic. With conventional continuous light sources, this phenomenon is only possible if the produced field intensity reaches high photon fluxes in the range of 10^{20}-10^{30} photons/cm^2. Not only high intensities values are difficult to reach with continuous light sources, but also present a substantial risk in terms of energy flux and heat deposition for biological samples. With the development of mode-locked femtosecond light pulsed lasers the high photon fluxes delivery

became possible. Moreover, the spatial concentration of the beam with high numerical aperture objectives enhanced the probability of nonlinear events to happen in a small focal volume (typically 1 μm^3) still providing controversial levels of photodamage[95] (the question of energy deposition is detailed in Chapter 2). The microscopic confocal configuration combined with a scanning system, most commonly used in MPM, allows nonlinear effects to be produced only in a precise focal volume, rejecting the out-of-focus noise and providing high lateral and axial resolution. In biology and neuro-imaging, confocal MPM microscopy, used to observe mainly 2PEF or SHG signals has become the most widely used imaging technique appreciated for its non-invasive serial optical sectioning of intact thick living specimens with high contrast. However, this technique presents some caveats, and that is why alternative imaging techniques have been developed.

1.3.1 Two photon excitation fluorescence

Two photon excitation fluorescence (2PEF) is the most common MPM mode of contrast used in biology and neuro-imaging and has been used to image physiological functioning in microscopic and subcellular neural compartments. 2PEF is a process in which a fluorophore is excited almost simultaneously (10^{-16} s)[96] by two photons carrying the same energy, providing the required energy for a transition from the ground state to the excited state. The relaxation of the fluorophore occurs via vibrational processes to the lowest energy level of the excited electronic states (Figure 1.9). This relaxation is accompanied by an emission of a higher wavelength photon, and temporally delayed with respect to the absorption process. The probability of a two-photon absorption by a fluorophore is a quadratic function of the incident intensity. However, no quantitative prediction based on the one photon excitation spectrum is possible since the processes involved in the two-photon absorption do not answer the same quantum-mechanical selection rules. A wide range of studies have been conducted on the estimation and comparison of the one photon and two-photon cross sections, values which have been useful in the concept of 2PEF imaging with dyes[96].

In the recent years, 2PEF has found practical applications in imaging of intact neural tissues due to its high-resolution, high-sensitivity and low photodamage confined in a small focal volume. 2PEF microscopy, photo-stimulation and photo-uncaging of specific dyes have contributed to the understanding of a broad array of neurobiological phenomena[97,98], including the dynamics of single channels in individual synapses[99], or at larger scale to the functional organization of cortical maps[100].

1.3.2 Second harmonic generation

As mentioned earlier, SHG was the first nonlinear optical process observed[94]. In SHG imaging, two

incident photons of same energy interact with a medium but, unlike 2PEF process, a direct conversion into a single emitted photon at exactly half of the excitation wavelength occurs resulting in no energy deposition. SHG can be interpreted as a coherent phenomenon: radiations from different molecules present in the excitation volume can interfere constructively or destructively depending on their spatial distribution. Additionally, SHG is a two-photon process that requires a non-centrosymmetric structure. This lack of symmetry comes from the intrinsic properties of the material itself, its structural arrangement on a molecular and macromolecular scale, or from breaking the orientation distribution symmetry of molecules either at interfaces or with an electric field.

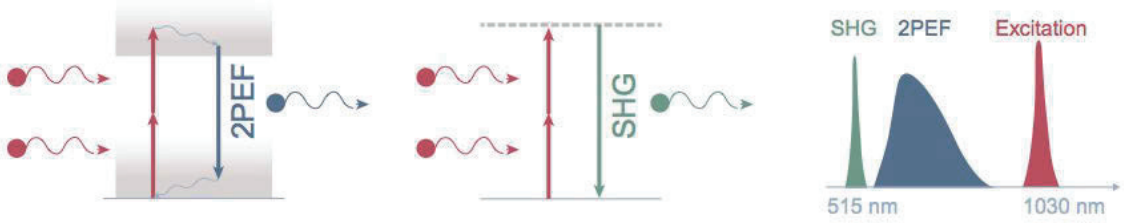

Figure 1.9: 2PEF (two photon excitation fluorescence) and SHG (second harmonic generation) processes with their corresponding emission wavelength.

2PEF and SHG processes provide complementary specific signals and can even be detected simultaneously by taking advantage of their spectral difference. As we mentioned earlier, 2PEF is Stokes-shifted compared to the half of the excitation wavelength whereas SHG occurs at half of the excitation wavelength (Figure 1.9).

SHG technique in a confocal microscopy configuration allows imaging in thick and deep tissue with a micrometer scale resolution. Effective biological use of second harmonic imaging goes back to a decade ago only. Nowadays, it is widely used to image non-isotropic polar structures such as collagen[101–103] and muscle myosin[104,105]. Up to date, a few label-free studies have been performed on neurons in culture[69,71], but because of the weak contrast of SHG in these conditions, recording times per image are long, as reported in the works of Dombeck (~ 120 s) and photo toxicity is high[72]. Alternatively, as mentioned in section 1, other methods with nanoparticles and quantum dots[106] or labelled resonant SHG approaches using membrane and potential sensitive dyes have been used to image membrane potentials[83,84,86,87] whereby the optical response was correlated to the reorientation of the chromophore in the membrane[83].

It is clear that for a better understanding of neuronal activity, a label-free non-invasive direct SHG probe of biological and molecular aspects in neurobiology is of great significance. In neurons, to avoid photodamage and because of the complex geometry of MTs in different neurites, SHG signals are weak, and an improvement in the excitation layout and detection efficiency of several orders of

magnitude is foreseen to be needed. This topic constitutes the essence of my thesis and will be detailed in the next chapter.

1.4 Principles of second harmonic generation

1.4.1 In non-centrosymmetric structures

For a monochromatic illumination, the optical response of a material in terms of the induced polarization can de expressed as follow:

$$P = \varepsilon_0 \chi^{(1)} E \tag{1.3}$$

$\chi^{(1)}$ is the nonlinear susceptibility defined such as $n^2 = \varepsilon_r = 1 + \chi^{(1)}$,with n the index of refraction and ε_0 and ε_r the vacuum and medium permittivity respectively, In non-linear optics, we can express the non-linear response of the material as a Taylor expansion of the material polarization in powers of the incident electric field E. This leads to the expression of the material polarization (considering only one component k):

$$P_k = \sum_{ijkl} \varepsilon_0 \left(\chi_{ik}^{(1)} E_i + \chi_{ijk}^{(2)} E_i E_j + \chi_{ijkl}^{(3)} E_i E_j E_l + \cdots \right) \tag{1.4}$$

where $\chi^{(n)}$ is the n-order non-linear susceptibility tensor.

We can compute the non-linear polarization for an incident electric field at a given frequency ω. The electric field E_i is expressed as

$$E_i = A_i \exp(-i\omega t) + cc \tag{1.5}$$

For simplification purpose, we will consider only the first term $A_i \exp(-i\omega t)$ with A_i the electric field amplitude at a given position. cc is the conjugated complex which we will not explicit. Finally, the second order non-linear polarization is:

$$P_k(2\omega) = \chi_{ijk}^{(2)} \left(A_i A_j \exp(-i2\omega t) + \cdots \right) \tag{1.6}$$

In this expression, the term in $\exp(-i2\omega t)$ represents the charge oscillation at twice the fundamental frequency: SHG contains a component that radiates at half the excitation wavelength. A major limitation to obtain SHG radiation is the requirement of a non-centrosymmetric environment. This statement can be easily understood with the above expression of the non-linear polarization since all even-order indices disappear for media with inversion symmetry. This can also be understood with the displacement of polarizable electrons in a non-centrosymmetric environment. Indeed, the strong electric field polarizes the electrons in such a way that their behavior becomes anharmonic and their oscillations contain a component at the second harmonic frequency (Figure 1.10a).

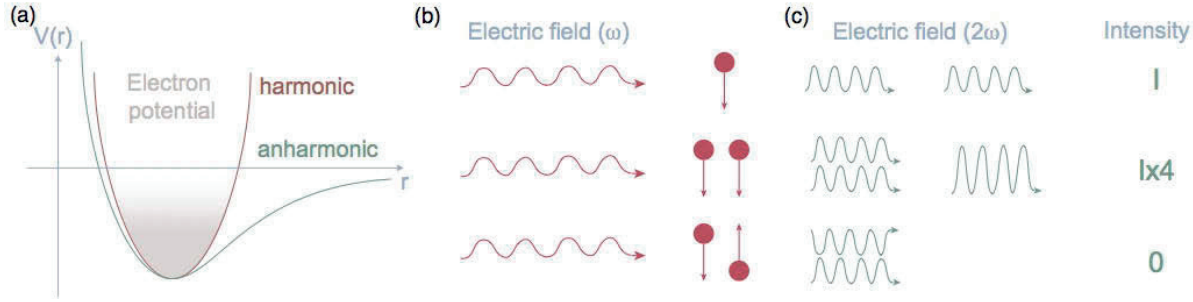

Figure 1.10: The displacement of polarizable electrons in a non-centrosymmetric environment. (a) The harmonic and anharmonic oscillation of an electron with the influence of a strong electric field. (b) Different configurations of oscillating entities with their respective interference pattern and their corresponding SHG intensity.

However, SHG is defined as a coherent second-order non-linear process. Therefore, the resulting SHG intensity is obtained as the square of the sum of the total harmonic fields originating within the focal volume. Two kinds of interactions can occur depending on the structural arrangement of the harmonophores (i.e. oscillating entities) in this focal volume. If the harmonophores are aligned in the same direction, the resulting interferences are constructive and lead to SHG signals. On the other hand, if their distribution is centrosymmetric, with anti-parallel directions, (Figure 1.10b-c) fields add up in a destructive way leading to a vanishing SHG signal. Examples of such organization and symmetries are found in biological media, for instance collagen, or microtubules.

1.4.2 In voltage-sensitive processes

Charge polarization and induction of dipoles are at the origin of propagation of light in any medium. Thus, for neuronal label-free applications on cell membranes, we can express the relationship of the induced 2nd order polarization vector $P^{(2)}(2\omega)$ with the interfacial electrostatic field E_m as follow:

$$P^{(2)}(2\omega) = \chi^{(2)}: E(\omega)E(\omega) + \chi^{(3)}: E(\omega)E(\omega)E_m \qquad (1.7)$$

$E(\omega)$ represents the electric field of the incident light, $\chi^{(2)}$, the second order electrical susceptibility tensor that depends on the intrinsic property of the material, and $\boldsymbol{\chi}^{(3)}$ is the third-order tensor associated with the third order process that links the electric field of the membrane to the frequency response. This can be illustrated with the explicit expression of the electric field, $E(\omega)^2 = E_0^2 \exp(i2\omega t)$ representing the second harmonic oscillation, which oscillates at 2ω. With this formalism, $\chi^{(3)}: E(\omega)E(\omega)Em$ also oscillates at the second harmonic. In most materials[86],

$\chi^{(3)}:\mathrm{E_m} << \chi^{(2)}$, so the second term is often neglected. In this thesis, we are interested in the membrane potential changes in neurons which occur at significantly higher time scale than the oscillation of the field. As explained in the previous section, the typical resting membrane potential for a cell is around -70 mV. The average electric field across a 7.5 nm thick plasma membrane is in the range of 10 mV/nm (10^5 V/cm) and in those conditions, $\chi^{(3)}:\mathrm{E_m}$ becomes comparable to $\chi^{(2)}$. Therefore, a slight change in the membrane electrostatic field E_m will induced a change in the induced polarization resulting in small variations of the detected SHG intensity. That is why, high sensitivity in SHG detection is required to detect such slight fluctuations.

1.5 This thesis

In this thesis, we develop a 3D-wide field high throughput nonlinear microscope. We demonstrate the possibility of label-free imaging of neuronal structures and electrical neuronal activity in cultures employing the unique intrinsic potential sensitivity and high imaging throughput of our microscope. This thesis is structured in the following way:

- Chapter 1 gives a brief overview of the biological concepts of the morphological and electrical aspects of the neurons and the state of the art in the field of neuro-imaging. The last section introduces the theoretical principles of nonlinear optics that we will be using throughout this thesis, 2PEF and SHG.
- Chapter 2 contains the description and characterization of the developed imaging systems and the methodology needed for our experiments. Samples preparation protocols and technical details are given in this chapter.
- Chapter 3, contains information about the microtubules-based cytoskeleton of cultured neurons. Then, we present an experimental application on the dynamic mapping of drug-induced microtubule instabilities.
- Chapter 4 describes SH polarimetric measurements and the quantification of the coefficient of polarization from neurons at different stages of maturity. We establish a comparison between two mode of contrast, 2PEF, highlighting the metabolic activity and SHG.
- Chapter 5 describes the label-free optical measurements of neuronal resting membrane potentials. We measure the signal arising from the oriented interfacial water molecules within the presence of transmembrane electric fields to map membrane potentials, by exploiting the high sensitivity of the 3D high throughput SH microscope.
- Chapter 6 contains a summary of this thesis and provides an outlook of future works in this realm and perspective for additional experiments and analysis.

The list of the published and submitted publications are found at the end of this thesis.

Chapter 2:
Experimental Details & Methodology

Second harmonic generation (SHG) is inherently sensitive to the absence of spatial centrosymmetry, which can render it intrinsically sensitive to interfacial processes, chemical changes and electrochemical responses. Here, we seek to improve the imaging throughput of SHG microscopy by using a wide-field imaging scheme in combination with a medium-range repetition rate amplified near infrared femtosecond laser source and gated detection. The imaging throughput of this configuration is tested by measuring the optical image contrast for different image acquisition times of $BaTiO_3$ nanoparticles in two different wide-field setups and one commercial point-scanning configuration. We find that the second harmonic imaging throughput is improved by 2-3 orders of magnitude compared to point-scan imaging. Capitalizing on this result, we perform low fluence imaging of (parts of) living mammalian neurons in culture, Next, we follow the rotation and translation of noncentrosymetric crystalline particles, or nanodoublers, with 50 µs acquisition times in living cells. The rotational diffusion can be derived from variations in the second harmonic intensity that originates from the rotation of the nanodoubler crystal axis. We envisage that by capitalizing on the biocompatibility, functionalizability, stability, and nondestructive optical response of the nanodoublers, novel insights on cellular dynamics are within reach. Finally, we introduce a 3D SH imaging system that uses structural illumination to achieve a better spatial resolution and the capability of z-sectioning.

The microscope described in the first section of this Chapter was built by Carlos Macias-Romero and Marie Didier. For the work presented in the two first sections, Marie Didier, Lucas Delannoy performed the experiments and together with Carlos Macias-Romero, they did the data analysis.
The 3D wide-field Second Harmonic microscope was built by Carlos Macias-Romero and Marie Didier. The parts related to biologically relevant measurements were implemented by Marie Didier who adapted it accordingly to the needs of the experiments.

2.1 High throughput wide-field second harmonic imaging for label-free biological imaging

Second-harmonic generation (SHG) is an elastic two-photon process in which two photons are transformed by a material into one photon with the double frequency. SHG is inherently sensitive to the presence of spatial non-centrosymmetry. Therefore, it is sensitive to bulk non- centrosymmetric structural spatial arrangements (in fibrils or in crystals), interfaces, or electric field induced breaking of symmetry. SHG imaging was demonstrated in the 1970's[94,107] and was first applied to imaging tissues in the 1980's[101]. Thanks to the development of, among other things, ultrafast laser sources, it is only in the two recent decades that SHG imaging has seen a tremendous development [108,109]. SHG imaging has been applied in many chemical, biological and medical applications. For example, ferroelectric domains in niobite crystals[110] , dye covered Langmuir films[111] modified membranes[112–114] (using the UV resonance of biomolecules), quantum dots[115] , and non-centrosymmetric crystal structures of proteins at very low concentrations in solution and bacteria have been successfully explored[116–118].

The intrinsic energy conservation of the SHG process ensures low photo-damage and -toxicity, which is ideal for imaging of biological and medical samples. SHG imaging has been used to visualize the membrane of vesicles[119] and cell membranes with the aid of fluorophore labeling[120] and to image tissues that are rich in endogenous non- centrosymmetric material, such as collagen[121,122], muscle myosin[104,123] and microtubulin fibrils[124–126]. The latter has been used to determine the microtubule organization in neurons[124,125]. SHG studies have also been performed to aid medical diagnostic purposes[121,125–128] and medicine development[129,130]. Voltage sensitive membrane specific markers have permitted for single site time dependent optical recordings of membrane potential activity[72,83,131–134]. This enabled the team of Yuste and Eisenthal to measure the length of the dendritic spine necks in living neurons and to determine that dendritic spines linearize the summation of excitatory potentials[135]. In another promising approach, SHG active surface modifiable non-centrosymmetric nanodoublers[136] have been introduced as a practical alternative to fluorescent molecules and quantum dots, to track processes through in-vitro (cell) imaging[137–141]. These studies clearly demonstrate the unique ability and promising possibilities of SHG microscopy to probe materials and interfaces, identify and quantify histoarchitectural tissue alterations, and to track changes in living systems.

Even though SHG imaging is used in a wide range of applications, the imaging throughput, defined as number of detected photons per frame per second, is still relatively low compared to linear microscopy[142]. An improvement of the imaging throughput could enable the use of SHG imaging to detect dynamical biological processes that occur on the (sub) millisecond time scale or advance the use of label-free SHG imaging for material studies or clinical applications. Label-free imaging applications are of interest for clinical and long-term measurements; labels (chromophores or particles) inevitably interfere with the process of interest and are often toxic, limiting the imaging time significantly. Two approaches are taken to improve imaging throughput (reviewed in[142,143]): The first one is to improve the scanning speed of the microscope in combination with the use of faster repetition rate laser sources[144,145]. The second one is to parallelize the imaging process. Recent advancements[143] include wide-field counter propagating SHG geometries[114,115], lens-less imaging approaches[146], harmonic holography[147,148], multi-confocal imaging[149,150], and spatiotemporal wide-field illumination[151–155].

Recently we presented a method to perform high throughput SHG scattering experiments to obtain elastic non-resonant surface responses from unlabeled 80 nm sized liposome membranes in aqueous solution with 5 millisecond acquisition times, in which we employed a medium-ranged (200 kHz) repetition rate femtosecond amplified laser system in combination with gated detection[156]. In principle this throughput could also be achieved in an imaging application. We therefore investigate here the possibilities of SHG imaging using a wide-field illumination scheme in combination with such a laser source and gated detection. We start by considering the parameters that are needed to maximize imaging throughput, so that laser fluences can be kept low (as required for biological imaging) and characterize the optical parameters of our proposed scheme. Then, we compare our approach to a commercial scanning SHG microscope, and a previously published wide-field approach employing a 1 kHz near infrared femtosecond laser as light source. We find an improvement in imaging throughput of 2-4 orders of magnitude compared to the commercial scanning system and the 1 kHz system. Finally, we explore the possibilities for label-free low fluence imaging of single living neurons in culture.

2.1.1 Image throughput considerations

The image efficiency is defined as the number of photons detected per area and as a function of time[157]. To maximize the imaging throughput, we consider the number of photons N_i produced per second per illuminated area:

$$N_i \propto \left|\Gamma^{(2)}\right|^2 \frac{E_{p,i}^2}{\tau_i \cdot A_i} f_i, \tag{2.1}$$

where $\Gamma^{(2)}$ is the effective second-order surface susceptibility of the probed surface or microscopic object[158]. The index *i* is used for the comparison between the scanning system (*s*) and our wide-field system (*wf*). $E_{p,i}$ is the pulse energy (in J), τ_i the associated pulse duration (in s), the repetition rate f_i is given in Hz and the illumination area $\mathcal{A}_i$, is in m^2. The illumination area and the repetition rate of the laser source are two influent parameters in the imaging output of the system. It is clear from this equation that decreasing the area and increasing the repetition rate increases N_i.

However, to calculate the throughput in an imaging system it is necessary to take into account the ratio between the size of the image and the illumination area. In a wide-field configuration the size of the image is defined by the size of the illumination area $\mathcal{A}_{wf}$. In a scanning system, assuming the scanning rate of the system is one image frame per second, the number of scanning points is $n = \mathcal{A}_{wf}/\mathcal{A}_s$. The latter is a reasonable assumption, but somewhat on the low side as it is common in scanning systems to oversample the image.

The amount of energy delivered onto the surface of the sample, the fluence (F_i), is defined as the ratio between the pulse energy of the incident field (E_i) on the illumination area ($\mathcal{A}_i$), $F_i = E_{p,i}/\mathcal{A}_i$. Assuming that the pulse wavelength, duration and fluence is equal for both scanning and wide-field systems, we have $\tau_{wf} = \tau_s$ $F_{wf} = F_s$, and $E_{wf} = n.E_s$. We can then compute the throughput ratio $\frac{N_{wf}}{N_s}$ as

$$\frac{N_{wf}}{N_s} = n.\frac{f_{wf}}{f_s} \tag{2.2}$$

Thus, for an image with 100 x 100 (or 1000 x 1000) scanning points and a repetition rate f_s= 100 MHz, a wide-field system delivers more photons per image per second if f_{wf}> 10 (or 0.1) kHz. Depending on the size of the image, a further substantial improvement is possible with higher repetition rates: a 100 kHz system may reach a 10 – to 1000-fold improvement.

We observe such improvement when plotting the imaging throughput as a function of fluence for three different imaging schemes (Figure 2.1a): a scanning system (80 MHz, 820 nm, 190 fs), with an illumination diameter of 0.5 µm, image size of 100 x 100 µm (black line, Figure 2.1a); a wide-field double-beam illumination (1kHz, 800 nm, 190 fs) with an illumination ellipse with diameters of 250 and 1000 µm (emission area with a diameter of 250 µm, green line in Figure 2.1a); and a wide-field double-beam illumination representative of our setup (200 kHz, 1028 nm, 190 fs) with an illumination ellipse with diameters of 100 and 140 µm (red line in Figure 2.1a).

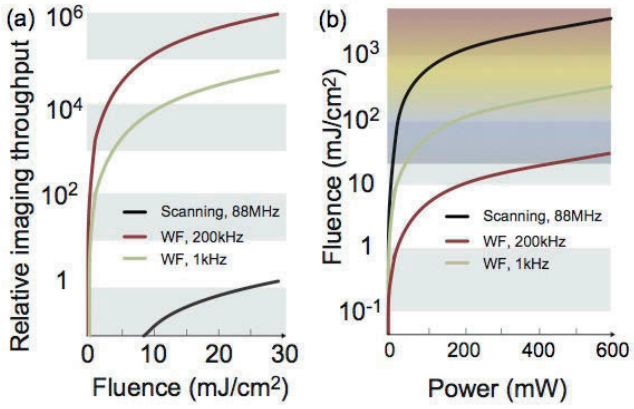

Figure 2.1: Calculated imaging throughput. These graphs are taken from the published works of Macias et al.[159]**.** (a) The imaging throughput for a given fluence (proportional to the number of emitted photons per image) for a scanning imaging system (black line), a wide-field imaging system as described here (red line), and a 1 kHz wide-field system (green line). (b) Calculation of the delivered fluence for a given power for the three different systems; the illumination parameters can be found in the text. The colored area illustrates for which fluences unstained CHO cells start to be perturbed in growth (yellow) and permanently damaged (red)[160].

Low fluence imaging is of particular importance in biological imaging. Irrespective of the mechanism to induce damage, imaging of living specimens requires that the delivered energy per area be kept as low as possible, so that the cells are minimally perturbed by the laser pulses. It has been reported that unstained CHO cells slow their growth rate and die above fluences of 381 and 1222 mJ/cm^2, respectively[160], when illuminating with 1035 nm wavelength, 393 fs pulses, 100 kHz repetition rate, and 10 x 50 µs dwell time. Figure 2.1b shows a calculation of the delivered fluence as a function of delivered laser power for the three different illumination schemes used in the calculation of Figure 2.1a. Damage thresholds are indicated by the colored area in Figure 2.1b. Larger illumination areas allow for lower fluences, and in the case of the wide-field configuration the used fluences are well below the reported damage thresholds.

It should be noted, however, that in reality the fluence for a scanning system is lower than the numbers used here since each pixel has a dwell time that is usually less than a millisecond. How much this matters for the actual damage done to a system depends on the optical transition, the excited state, and the energy transfer and transport equations that govern the phototoxicity and damage process. It is also likely that a certain spot on the sample may receive photons from neighboring scanning points so that it is not trivial to quantify these effects. For low repetition rates, effects such as white light generation become important. In terms of achieving maximum imaging throughput with our approach, it is thus likely that the energy transport mechanisms play an important role, which suggests that the maximum gain in imaging throughput is reached for repetition rates of ~1 MHz[161,162].

2.1.2 Imaging system and characterization

We employ two weakly focusing propagating beams as in[114,115] with an additional prism for efficient coupling (see Figure 2.2a-d). Compared to the systems of Kriech and Peterson[114,115] the illumination source and detector is very different. Kriech and Conboy in[114] used unfocused light from an optical parametric oscillator with a repetition rate of 10 Hz and pulse duration of 7 ns and 10 mJ output per pulse centered at 550 nm wavelength; the beam had a diameter of 2 mm incident on the sample at an angle of 70°, and the detection consisted of a monochromator followed by a photomultiplier tube. Peterson et al in[115] used 800 nm, 120 fs, 1 kHz laser pulses focused down to an elliptic area of π (125 x 500 μm)^2 with an unspecified power of 40-400 mW, and a CCD camera for detection. In our microscope, the illumination source is a Yb:KGW amplified pulsed laser (Pharos, Light Conversion) which generates 190 fs pulses centered at 1036 nm with a repetition rate of 200 kHz. Two loosely focused beams provide a large elliptical illumination area with a typical output power on the sample around 10-100 mW. The dimensions of the elliptical illumination spot on the sample is 100 μm by 140 μm in diameter. The pulse duration together with the temporal and spatial overlap of the beams, results in an illumination depth of 70 μm. The light is split equally over two counter propagating beams with an angle of 90 degrees that are coupled into the sample chamber using a 45 degrees prism (Figure 2.2b). The polarization of each beam is controlled by a zero-order half-wave plate (Thorlabs) inserted in the excitation beam just before the beam splitter and focused on the sample with a f = 20 cm doublet lens (Thorlabs) (Figure 2.2c). This non-collinear two-beam geometry allows to probe 8 polarization configurations and to prevent any optical damages to the objective lens. The collection of the SHG or TPEF signal is done through a 50x, 0.65 NA objective lens (Mitutoyo Plan Apo NIR HR Infinity-Corrected Objective) in combination with a tube lens (Mitutoyo MT-L), an 800 nm short pass filter (omega optical) a 515 nm band pass filter (Omega Optical, 10 nm bandwidth) in the forward direction along the phase-matched direction of the two incoming beams. Such forward detection geometry is encouraged for imaging of samples such as thin and transparent biological tissues or living cells. Detection and acquisitions are done with a gated EM ICCD Camera (Pi Max 4, Princeton Instrument) with different combination of Electron Multiplier Gain, Intensifier Gain, on-CCD accumulation, binning and frame transfer parameters to change the readout time and to enhance the signal. A meniscus lens was placed behind the objective lens to remove spherical aberrations induced by the coverslip.

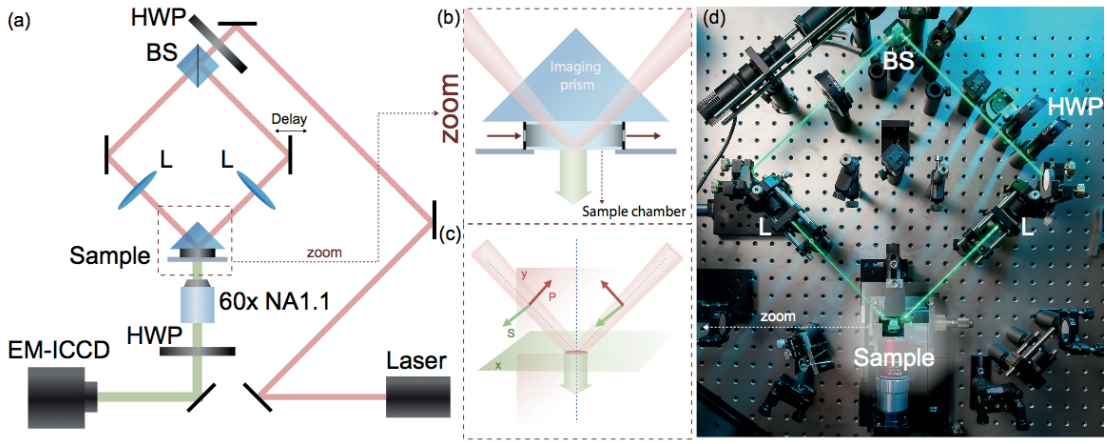

Figure 2.2: Optical layout of the high throughput wide-field SH microscope. (a) The optical layout of the nonlinear microscope. Symbols: HWP: half wave plate, L: lens, BS: beam splitter, EM-ICCD: camera detector. The delay line is adjusted to overlap the two beams spatially and temporally onto the sample. The polarization of the two beams is controlled with an HWP prior to the BS. (b) An imaging prism is used to couple the two beams and correct for polarization aberrations. A closed sample chamber with either nanoparticle or coverslips is placed under the prism (see details in Figure 2.3). A flow of solution can be implemented in the chamber (red arrows) to provide the cells with fresh solution and nutriments during live-cell experiments. Imaging is done in the forward direction. (c) polarization configuration. The plane perpendicular to the sample plane contain the polarization defined by y (or P), and the plane parallel to the sample plane, a polarization along x, (S). (d) photograph of the imaging setup, built with a vertical configuration.

Epi-detection can be implemented easily by rearranging the incoming beams, changing the prism to a flat top prism, and correcting for spherical aberrations. In the imaging system of Figure 2.2(a-d), the illuminating section has a larger depth of field compared to scanning nonlinear microscopes and spatiotemporal focusing microscopes[151–155]. It is possible to limit the illumination depth by using a 5 µm high sample cell[159] or by producing axial cross-sections using structured illumination[155]. In principle spatiotemporal focusing shares some of the improvement in imaging throughput. The detection is different, and spatiotemporal aberrations induced by e.g. biological specimens are no issue here.

We built a closed-chamber for live-cells measurements, adapted to our microscope. As explained before, the chamber is positioned under the imaging prism and the detection is done in the forward direction (Figure 2.3a).

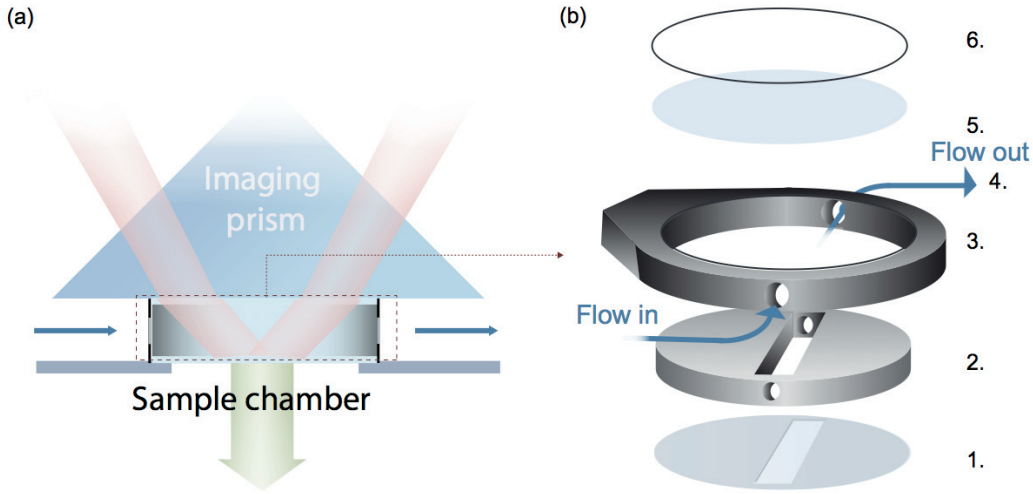

Figure 2.3: Imaging chamber. (a) Two loosely focused beams coupled with a prism onto the sample plane. The closed chamber containing the samples is placed under the prism. The detection of SHG is in the forward direction. (b) Organization of the different compounds constituting the closed sample chamber: 1. Coverslip with cultured cells, 2. Teflon chamber gently placed on top of the coverslip with cells. Holes are made from either side of the chamber to allow an in and outflux of solutions connected to a gravity perfusion system. Imaging of the cells is allowed only from the center of this chamber, 3. Modified Lens mount (LMR1 - Lens Mount for Ø1" Optics) with holes from either side of it. 4. Outflow of solution existing the chamber connected to a waste. During live cells experiments, a constant flow of physiological solution is running to keep the cells alive under the microscope and renew their environment in nutritional media, 5. Standard coverslip and 6. retainer ring (SM1RR - SM1 Retaining Ring for Ø1") to close the whole sample chamber.

We used a standard gravity perfusion system to flow fresh solution through the closed custom-made sample chamber (Figure 2.3b). Due to the imaging configuration with the imaging prism and the closed-chamber disposition, this layout is not fully optimized for live cell imaging. The second section of this chapter will describe another microscope, with an open-chamber disposition, more suitable for long term live-cell imaging.

2.1.3 Imaging throughput measurements

To test the throughput of this configuration, we have measured SHG images of 50 nm $BaTiO_3$ nanoparticles that were deposited on a coverslip using fiducial markers. We tested three different illumination conditions, corresponding roughly to the configurations used in the calculation of Figure 2.1. We measured images from the same spot on the same sample with the same wavelength and pulse duration. The fluence was 10.5 mJ/cm2 for the 1 kHz system or 2.55 mJ/cm2 otherwise and the imaging acquisition time was varied. The contrast (amplitude of the signal divided by its spanning range) was calculated for each image and plotted as a function of acquisition time in Figure 2.4. The black data points were taken with a Leica TCS SP5 scanning microscope in transmission mode, the

blue and the red data points were obtained with the SHG wide-field system of Figure 2.2 (using different gain settings for the camera), and the green data points were obtained by reducing the repetition rate of our laser to 1 kHz and using a regular CCD camera, i.e. without intensifier or electron multiplier, with a quantum efficiency of 50%. Figure 2.4 suggests that the same contrast can be obtained with either one of the systems, but with acquisition times that are 2-3 orders of magnitude shorter when using the wide-field system of Figure 2.2.

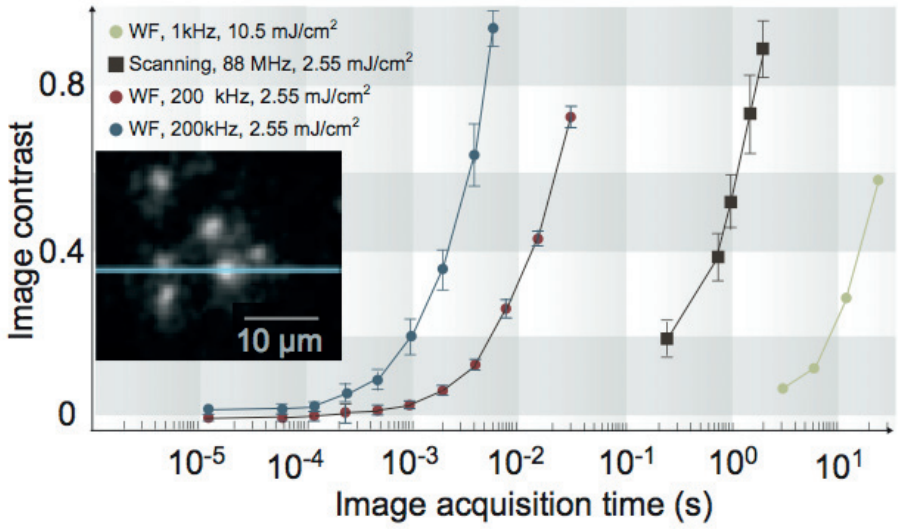

Figure 2.4: Measured imaging throughput. Measured contrast in the images recorded from the same position of the same sample in four different systems: wide-field (200 kHz, gated detection as proposed here, blue and red curves), a scanning microscope (Leica TCS SP5 with 1028 nm, 88 MHz, 190 fs laser pulses illumination, a 1.2 NA 20x water immersion objective, a scanning rate of 1000 Hz/line, image size of 256 x 256 pixels, and collecting NA of 0.9), and a wide-field 1 kHz geometry with a normal CCD camera. The used pulse power and repetition rate are given in the legend. The blue data points were recorded with the intensifier and the electronic amplification of the camera both turned on, while the red data points were recorded with only the intensifier on. The inset shows an image of the nanoparticle sample.

An increase in imaging throughput of several orders of magnitude can thus be obtained compared to the 1 kHz configuration (similar to[115]) and the commercial scanning system for elastic SHG imaging. To confirm this conclusion, however, we first verify that our data points are indeed reasonable compared to published literature. Regarding the scanning measurement of the $BaTiO_3$ nanoparticles, we can make a direct comparison to the work of Pantazis et al. in[137], who imaged immobilized 30 – 90 nm $BaTiO_3$ nanoparticles in a scanning configuration, using 820 nm, 80 MHz, 300 fs pulses focused down to a $\pi \times (0.26\ \mu m)^2$ focal area with a power of 5 mW. They calculated the signal to noise ratio (SNR) of their images to be 10 when imaging at 20 frames/s (or 50 ms/frame) an area of 0.69x0.69 μm^2 and using a 40 nm-broad bandpass filter. Taking those parameters, their fluence would

be F = 29.4 mJ/cm^2. For our scanning data (black curve), an SNR of 13 is obtained using 50 nm nanoparticles if we scan at 0.48 frames/s (2.1 s/frame) an area of 30x30 μm^2, with a fluence of 2.55 mJ/cm^2 and using a 50 nm-broad bandpass filter (BP525/50). Comparing the image acquisition time, we have 2.1 s vs 50 ms in[137]. Thus, we have a factor of 42 longer in the acquisition time, but this is obtained with a fluence that is a factor of 11.8 smaller. Correcting for the difference in fluence, scanning areas, pulse durations, frame rate, and SNR, it therefore seems that the imaging throughput of our scanning measurement compares well with that of the literature.

2.1.4 Label-free SHG imaging of sub-cellular structures

Figure 2.5 shows images of living primary cultured neurons (from E17 OF1 mice embryos). Figure 2.5a shows the phase contrast (PC) image of unstained cultured neurons (28DIV: 28 days *in vitro*). The image displays a cell body from which emerged several neurites (arrows) and one axonal-like neurite (arrow head). Figure 2.5b shows the corresponding TPEF and SHG signals are shown on the composite image in Figure 2.5b. The TPEF intensity is represented in blue, and the SH intensity either in red (with a polarization along the x direction, projected on the sample plane) or in blue (with a projection along the y). Figure 2.5c shows the three different channels split individually.

The image displays a cell body from which emerged several neurites. We notice a difference in the morphology of those processes, some are thick and rough (Figure 2.5a, arrows) and another, almost not distinguishable on the PC image is thinner (Figure 2.5a, arrow head). Figure 2.5b shows the corresponding TPEF (blue) and SHG intensities (in red, acquired with a polarization along the x axis, and in green acquired with a polarization along the y axis) which are shown as a composite image in Figure 2.5c. To make more precise and definitive structural assignments, a comparison of these images to images taken with targeted labeling should be considered, which is beyond the scope of this work.

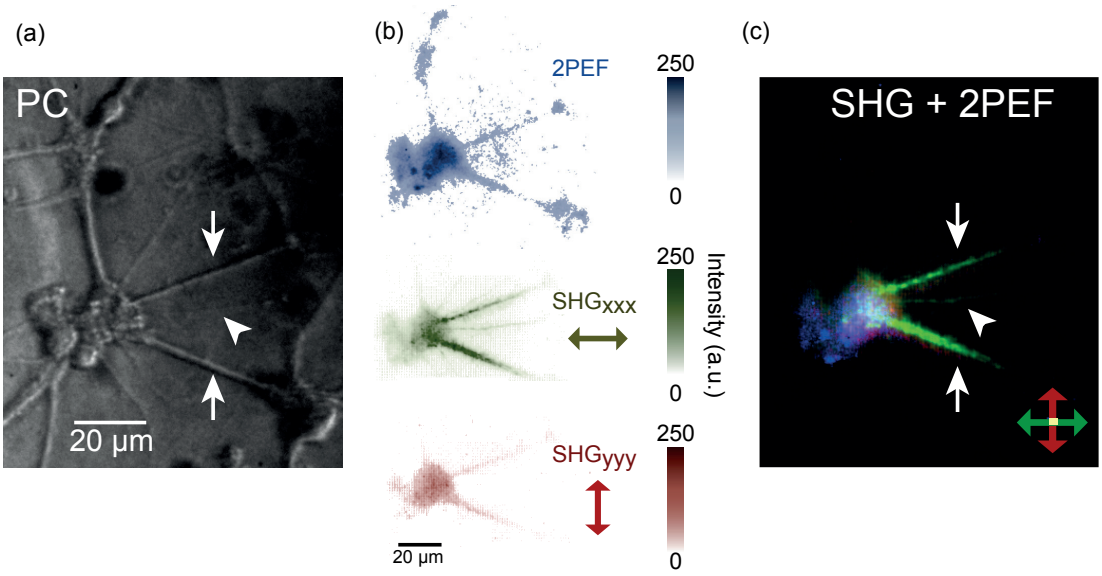

Figure 2.5: Label-free TPEF and SHG imaging of living neurons. (a) Phase contrast (PC) the two arrows show dendrites and the arrow head the axon, (b) Top panel: endogenous 2PEF signal averaged over 100 frames, with 639 ms/frame. Down and middle panels: SH images, in green obtained with an excitation and detection along x (xxx), and in red obtained with an excitation and detection along y (yyy). Both imaged are averaged over 100 frames, acquired with 639 ms/frame and a power on sample around 125 mW. (c) Composite image with label-free SHG xxx and yyy in green and red respectively, and endogenous 2PEF in blue. The two arrows show dendrites and the arrow head the axon as localized on (a).

Comparing the illumination parameters to literature, the SHG images in Figure 2.5 were recorded with ~6 s acquisition time, a fluence of 7.3 mJ/cm^2 (or averaged intensity <I> = 147 W/cm^2), and xxx polarization. Compared to earlier work on unstained neuronal cultures by Dombeck et al.[124] who used a 120 s acquisition time and averaged intensities of ~30 MW/cm^2 (= 3400 mJ/cm^2), the acquisition time and fluence is drastically reduced. Spatiotemporal focusing techniques have not yet been used for label-free imaging of living neurons[163]. Thus, we show here that the increased imaging throughput can be used to reduce the imaging acquisition time and/or the fluence, which results in a significant reduction of photodamage probability.

2.1.5 Conclusions

In summary, we have implemented changes in the optical layout of a second harmonic imaging system that increases the second harmonic imaging throughput for label-free elastic SHG imaging by several orders of magnitude. The increase in throughput was achieved with a wide-field geometry and medium repetition rate laser source in combination with gated detection. In addition to enhanced throughput, the pulse duration is not distorted and can be measured directly at the sample, and dynamic and ultrafast measurements can be performed readily with all 8 possible polarization

directions. Label-free second harmonic and TPEF imaging of living neurons have been performed with short acquisition time and at very low fluences. Clear second harmonic emission is observed from the neurons, which is emitted from different locations as the TPEF.

2.2 Probing dynamics in living cells: translation and diffusion of $KNbO_3$ nanoparticles

Cellular functions rely on a complex network of pathways and dynamic processes. To study dynamical processes such as membrane transport, translocation and formation, axonal transport, and drug delivery, it is often necessary to insert foreign bodies as probes that can be chemically and selectively linked to one of the actors to follow the process by optical imaging[164–168]. As mentioned in Chapter 1, ideal tracking probes should not saturate, blink, nor photobleach[169] and they should not be destructive or toxic to the embedded environment. The probe should be sufficiently small to not disrupt the process under study (100 nm or smaller) and have a narrow spectral bandwidth and a bright emission spectrum[139,170,171]. The probe should also be biocompatible and functionalizable. In order to obtain a complete map of the dynamics under study, both the translation and the rotation of the probe should be followed on ideally microsecond time scales (which is the typical time scale of rotational diffusion). To date, those aspects have not been met in wide field live cell imaging. In this chapter, we describe how we follow the rotation and translation of nanodoublers *in vitro* with 50 μs acquisition time per image. The rotational diffusion is derived from variations in the second harmonic intensity that originates from the rotations of the principal axis of the nanodoubler.

In recent years, many advances have been made both in terms of imaging systems and probe development. An imaging system dedicated to translational and rotational tracking should ideally have image acquisition times that are faster than the translational and rotational motion of a nanoparticle ($\ll$1 ms) and allow for a simultaneous observation of a large field of view (>2000 μm^2). Current state-of-the-art tracking imaging systems include one-photon fluorescent microscopes in confocal[172] total internal reflection fluorescence[173,174] (TIRF) and epi configuration[175], dark-field linear scattering[176,177] photothermal imaging[178] difference interference contrast microscopy[165,166,179,180] linear[181,182] and nonlinear[183] correlation spectroscopy, two- photon, single[184] and multi-confocal microscopy[185] planar illumination[186] linear TIR scattering[187] defocused wide field[188], nonlinear holographic imaging[136], and scanning second harmonic microscopy[136,137,189–192]. Linear *in vitro* imaging of gold nanorods with CMOS technology[165] can reach image acquisition times

of 2 ms. Second harmonic imaging of nanodoublers has been performed with a 50 ms acquisition time per image for fixed nanodoublers and with a 1 s acquisition time per image for *in vivo* imaging[193]. As mentioned in Chapter 1, in general, the image acquisition time for second harmonic imaging is commonly slower because of the weak nonlinear optical response and the subsequent need to scan a tight focus in order to overcome low signal-to-noise ratios.

For the probes, fluorescent molecules[164], metallic nano-particles[164,165,185] quantum dots[168,194] nanodiamonds[172] and nanodoublers[137,143,196–198,171,183,184,189–191,193,195] are available. While it is possible to track the translation of all these probes, the rotation can only be observed if some kind of geometrical or optical anisotropy is present. Nonspherical fluorescent molecules[167,173,174] , quantum rods[175] and metallic nanorods[165,166,176–178,180,182,185–187] are typically the preferred candidates for this purpose, using the anisotropy resulting from the aspect ratio of the object. Optical imaging combined with the detection of magnetic spin echo decay in nanodiamonds[172] is another approach toward tracking of translation and rotation. Nanodoublers are particles with a noncentrosymmetric crystal lattice structure. When a nanodoubler interacts with an optical beam with frequency ω, it emits light with a frequency 2ω with a spectral width that is determined by the spectral width of the incident optical beam. This second harmonic generation process is elastic; saturation and photobleaching are absent, allowing for measurements during indefinite periods of time. Nanodoublers can also be easily functionalized with, for example, proteins[138,139,141,192] for targeting[188] specific biological questions[136,138,139,170,171].

In this section, we demonstrate the possibility to track the translation and rotation of nanodoublers in living cells with image acquisition times as low as 50 μs per image. We show the translational diffusion of functionalized 100 nm $KNbO_3$ nanodoublers in water and inside living cells, paying attention first to the translational and then to the rotational motion of the nanodoublers.

2.2.1 Particle characterization

The nanodoublers used in our study are $KNbO_3$ crystalline particles that are coated with polyethylene glycol (PEG)[171]. The particle size distribution was measured by dynamic light scattering (DLS) in water and cell serum, which showed an average particle diameter of ~107 nm with a polydispersity index of 12%. The particles were further characterized by transmission electron microscopy (TEM) in imaging and diffraction mode (Figure 2.6). The TEM diffraction images show that the particles are highly crystalline, while the TEM images show that the particles have an irregular shape. Because the DLS size distribution in solution is narrow and the TEM images display different irregularities per particle (see Appendix 2.5.1), we approximate the particle shape as spherical, which we will need to calculate the rotational diffusion.

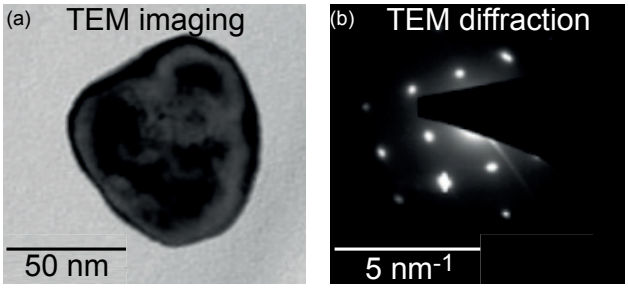

Figure 2.6: Transmission electron microscopy images and diffraction pattern of a single $KNbO_3$ nanoparticle. This method is used as a measure to determine its degree of crystallinity. More data on the particle characterization can be found in Appendix 2.5.1.

2.2.2 Translational diffusion of nanodoublers in water

We first explore the diffusion of 100 nm $KNbO_3$ nanodoublers[171] in pure water at room temperature (293 K). A nanodoubler dispersion of 3 μg/mL is inserted in the flow chamber (5 μm in depth) and the trajectories of the particles are recorded with 250 μs acquisition time per frame. Figure 2.7a-c shows an illustration of the wide field illumination scheme, the beam geometry with the nanoparticles in the flow chamber and the principle behind the measurement of the nanodoubler rotation. Figure 2.7d shows a frame taken from a typical movie with the tracks superimposed. Figure 2.7e shows the mean square displacement (MSD) calculations and the corresponding fits to a Brownian diffusion model[199]. One can see from the MSD (Figure 2.7e) that, apart from the pink track (T1), which follows a driven motion, the rest of the particles follow approximately a Brownian motion[199]. The extracted diffusion coefficient of 20 tracks was 4.88 ± 0.59 μm^2/s. Given the small irregularities in the particles shape, this is in excellent agreement with the expected translational diffusion of 4.80 μm^2/s for 100 nm spherical particles in water. For the four tracks displayed in Figure 2.7e, the measured mean diffusion coefficient is 4.89 ± 1.49 μm^2/s. From the images it can be seen that the intensity distribution is uniform across each particle. The DLS data (see Appendix 2.5.1) shows that the solution contains single particles and no clusters. As the height of the sample chamber (5 μm) (Figure 2.7b) is smaller than the illumination depth (70 μm) all particles are in focus. The observed intensity variations can be related to particle rotation, as we will show later in this chapter.

Next, we explore the options for *in vitro* imaging and focus on the rotational dynamics of particles (with an acquisition time of 50 μs per image).

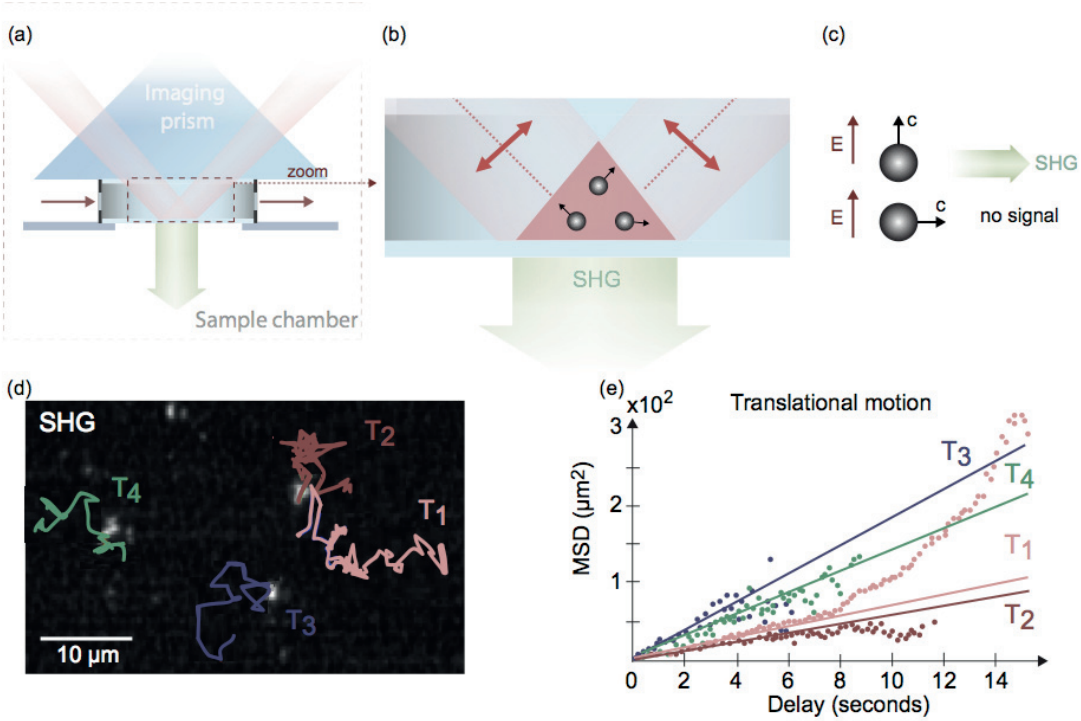

Figure 2.7: Principles of the method and translational diffusion of 100 nm $KNbO_3$ particles in water. (a) Schematic of the sample chamber, wide field illumination scheme and beam geometry. (b) Magnified inset of the sample chamber with an illustration of the principle behind the measurement of the nanodoubler rotation. The black arrows indicate the orientation of the principal axis of the crystal. The two incoming beams with a specific polarization state (red double head arrows) overlap onto the sample plane and interact with the single-axis crystals in water. (c) Scheme of the generation of SH when the polarization is parallel or perpendicular to the principal axis of the nanoparticle (noted as c in the image). The brightness of the nanodoublers in the image depends on the relative angle between their crystal axis and the electric field direction of the laser beam. A detailed description of the angles and formula can be found in the Appendix 2.5.4. (d) A frame taken from an SH intensity time lapse recording (time averaged for 10s) of nanodoublers diffusing in water (250 µs per frame confined to a chamber 5 µm in depth). The solid lines depict the tracks of four particles. (e) The corresponding MSD of the four nanoparticles tracked, with their respective linear fits using the first 15% of the maximum delay of the data.

2.2.3 Time resolved *in vitro* imaging

Figure 2.8 demonstrates the possibilities of time resolved imaging of cellular processes within living cells. Human epitheloid cervix carcinoma (HeLa) cells were electroporated with 100 nm diameter $KNbO_3$ particles. Figure 2.8a shows a phase contrast image (PC), and Figure 2.8b shows a time-integrated stack of second harmonic images of the cells containing the particles. Three dimensional confocal two photon fluorescence and second harmonic imaging of Nile red stained HeLa cells containing the nanoparticles showed that the particles are inside the cell (see Appendix 2.5.2). The arrow in Figure 2.8b points toward the motion of the selected nanodoubler. It can be seen that the cell has immobilized the particle encircled in red and that another particle appears to interact with the cell

membrane, which is possibly being ejected by the cell (blue path). The translational mean square displacement is shown in Figure 2.8c. Compared to Brownian motion in water (indicated by the black line), both particle tracks display a difference from normal diffusion.

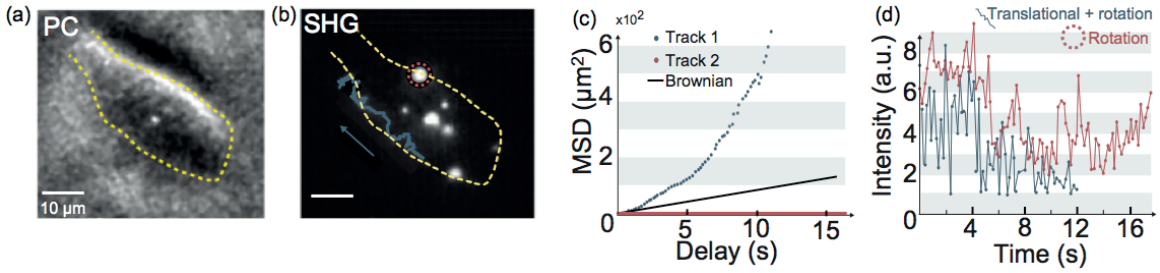

Figure 2.8: Time resolved nanoparticle tracking. Phase contrast image (a) and second harmonic image stack (b) of human epithelial cervix carcinogenic cells transfected with 100 nm diameter KNbO3 nanodoublers. The image in (b) is a time-averaged stack depicting in blue the track of a particle diffusing and rotating and a particle rotating encircled in red. The movie provided in the Supporting Information (Movie 2) displays the moving particle interacting with the membrane before continuing its path (blue track), and the rotation of the particle encircled in red. The mean square displacement (MSD) of each particle is shown in (c). It can be seen that the particle motion deviates significantly from Brownian motion (black line) for both cases. The intensity of the two nanodoublers is shown in (d) as a function of time. The intensity fluctuations are caused by rotational motion.

While the particle in red is not moving, the particle in blue follows a driven diffusion that is significantly faster (12.18 $\mu m^2/s$) compared to Brownian diffusion in water (4.80 $\mu m^2/s$). This significant difference might suggest that the particle is being ejected by the cell. The intensity of both particles is displayed as a function of time in Figure 2.8d, fluctuating on a scale of 1−9. As the standard error to the mean in our setup is 1−2%[156] we can exclude instrumentation errors as the source of the fluctuations. The significant variation in intensity is caused by particle rotation: the intensity of monocrystalline nanodoublers strongly depends on the orientation of the particle crystalline axis relative to the electric field of the illuminating beams (as sketched in Figure 2.7c and shown in more detail in Appendix 2.5.4). If the main crystalline axis of the particle is perpendicular to the oscillation direction of the input electric fields, no SH light is emitted (see Appendix 2.5.4 and Figure 2.20 for the theoretical calculations of the intensities). Vice versa, maximum SH emission is obtained when both are parallel. The same principle holds for our beam geometry. The Appendix 2.5.4 contains the formulas used to relate the intensity to the rotation of the nanodoublers. The intensity variations observed here correspond to those observed for immobilized particles illuminated with rotating polarization. This data is included in the Appendix 2.5.3 (Figure 2.19). The intensities of Figure 2.8 are similar in value as those in Figure 2.7, and the intensity distribution across the particles is also

uniform, indicating that we are measuring single particles. Because the scattered second harmonic intensity from a particle or cluster is strongly size dependent[200], clusters will have significantly larger intensities and are likely not present in the image. It is further interesting to note that the analysis of the rotational motion of nanodoublers using the temporal intensity profiles has been predicted previously[136,189,190,193]. In order to map the rotational diffusion more accurately we image nanodoublers *in vitro* with shorter acquisition times.

Figure 2.9 shows the rotational diffusion of the nanodoublers *in vitro* with integration times of 50 µs, together with a spatial map of the rotational diffusion coefficient. Here, HeLa cells were again electroporated with the 100 nm $KNbO_3$ particles and a movie was recorded with 50 µs acquisition time per image. Similarly, to Figure 2.8, the particles seem to be trapped inside the cell (which contours are indicated by the yellow dashed line in the SHG image in Figure 2.9a). The intensity (Figure 2.9b) displays variations in time (with the same order of magnitude as in Figure 2.8), which we analyzed using an MSD algorithm and the relation between the intensity of the particle to the rotation (see Appendix 2.5). Figure 2.9c shows the result of calculating the rotational diffusion for each pixel in the movie. It is clear that the various particles have different rotational diffusion coefficients, ranging from <1 deg^2/s up to 15 deg^2/s.

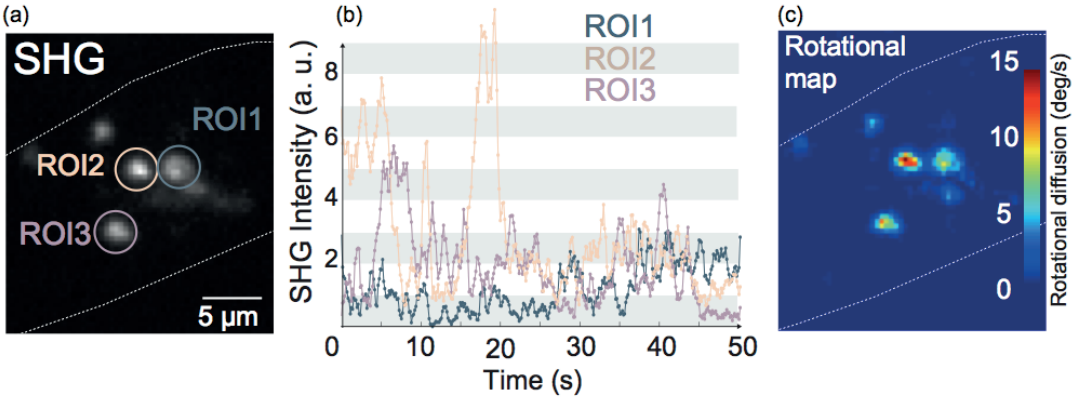

Figure 2.9: Spatial mapping of the rotational diffusion of 100 nm KNbO3 nanodoublers inside a living cell. (a) Second harmonic intensity integrated over 100 frames of a movie taken with an acquisition time per frame of 50 µs. (b) Temporal evolution of the second harmonic intensity at the points in (a) denoted as ROI1, ROI2, and ROI3. (c) Spatial map of the rotational diffusion obtained from the relation between the variations in intensity and the rotation of the nanodoublers; the r^2 value of the fit is shown in the Appendix 2.5.5.

Summarizing the above, our work demonstrates the possibility for high resolution *in vitro* imaging with specificity to translational and rotational motion with acquisition times in the microsecond range. Our approach parallels certain aspects of recent advances in multiphoton optical imaging, harmonic holography[147,148] multiconfocal imaging[150], and spatiotemporal wide field illumination[151,152,154,155]:

with harmonic holography, it has been possible to image 1500 nm sized clusters of SH active particles with 100 ms acquisition time per image (with 1 mJ peak energy)[147]. Single shot holography of moving particles *in vitro* has not been demonstrated but would be very promising. Multifocal multiphoton microscopy has been demonstrated with 1.6 ms acquisition time per image[150]. A wide field method based on spatiotemporal focusing has been used to track 500 nm fluorescent particles with 5 ms acquisition time per image in a comparable illumination area[154]. Comparatively, our approach allows to obtain 50 µs acquisition times and hence follow accurately the rotation and translation of 100 nm nanodoublers. Given that the amount of emitted light scales with the volume of the object we believe our approach represents an important addition. The elastic nature of the light matter interaction process ensures that rotational and translational tracks can be imaged for unlimited periods of time and minimal invasion. We envisage that by employing additional appropriate functionalization with, for example, proteins and antibodies[141], the dynamics of specific biochemical processes can be targeted with greatly increased precision.

2.3. 3D wide-field high throughput SH imaging

2.3.1 Imaging system and characterization

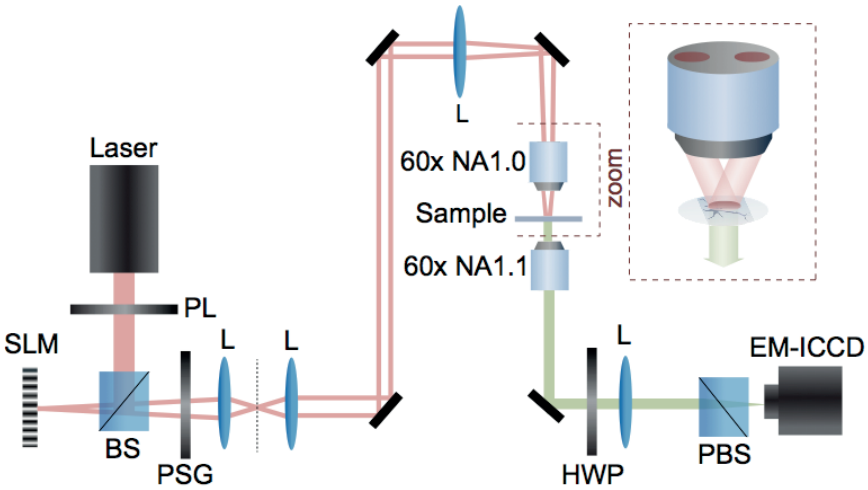

Figure 2.10: 3D wide-field Second Harmonic imaging system. Schematic of the 3D wide-field second harmonic microscope; with optical components: spatial light modulator (SLM), polarizer (PL), beam splitter (BS), polarization state generator (PSG), achromatic lens (L), dichroic beam splitter (DB), numerical aperture (NA), half wave plate (HWP), polarizing BS (PBS), (F) Fourier plane, conjugated with the back focal plane of the top objective. The magnified inset represents the non-collinear 2 beam imaging configuration with a forward detection.

The 3D wide-field SH microscope is represented in Figure 2.10. The light source is an amplified laser

system (Pharos SP-1.5, Light Conversion) delivering 168 fs laser pulses centered around 1036 nm (+/- 6 nm) with a beam diameter of 3.7 mm and a maximum output power of 6 W at variable repetition rates between 1 kHz and 1 MHz. For the experiments described in this thesis, the laser system is used at 200 kHz repetition rate. The pulse energy delivered to the sample is 36 µJ and shaped into a circular illumination spot size with a FWHM of 150 µm in the sample plane, reaching 2.15 mJ/cm^2 in terms of fluence and 12.79 GW/cm^2 in terms of peak intensity. A safe fluence for live-cell imaging is beyond 13 GW/cm^2 [201]. This fluence is achieved by tuning the output laser power to 2.8 W corresponding to 70% of its original value (4W) (see Appendix 2.5.5 for detailed fluence and energy deposit calculations on the sample plane). All experiments described in the following sections and chapters were performed with a percentage output power laser of 70%.

The laser beam illuminates a spatial light modulator (SLM, Phase Only Microdisplay 650- 1100 nm, fill factor of 93%, with a 1920 x 1080-pixel resolution and an 8 µm pixel pitch from Holoeye, Pluto-NIR-015) under normal incidence. The SLM is used as a reflective diffraction grating and generates a gray scale hologram image of a rotatable slit pattern (Figure 2.11). The pattern is filtered in the Fourier plane of a lens (f = 20 cm, Thorlabs) placed after the SLM, such that only the 1st and -1st orders are retained (Figure 2.11a-b). These two beams hit the back focal plane of a top objective (Olympus LUMPLFLN 60x1.0NA water immersion objective) and then imaged onto the sample plane (Figure 2.11c-d).

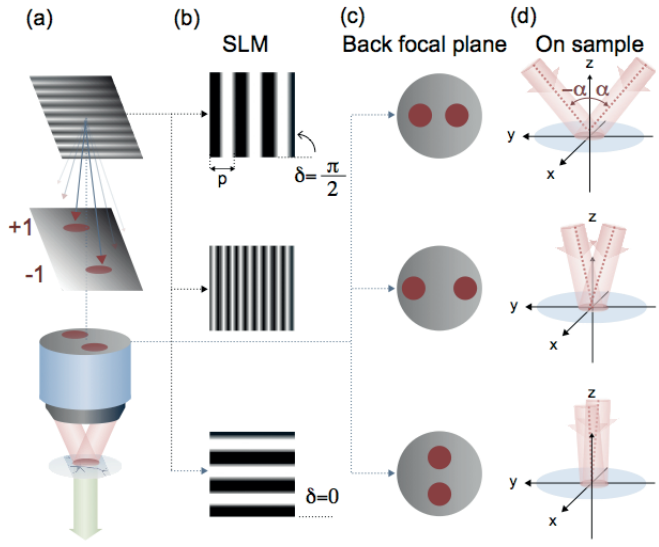

Figure 2.11: Layout of the two incoming beams at the back focal plane of the objective and their configurations at the surface of the sample plane. (a) A SLM used as a reflective grating generates multiple orders diffraction beams. We used an adjustable iris to select the two first orders of the diffracted beam (+1

and -1). (b) δ is the angle of the orientation of the grating's pattern. An angle of $\delta = 0$ rad, leads to an incident propagation in the (x, z) plane and $\delta = \pi/2$ to a propagation in the (y,z) plane. The period of the grating determines the angle between the two incident beams. A short period corresponds to a wide opening and vis versa (see Appendix 2.5.6 for detailed calculations). (c) The back focal plane of the top objective is conjugated with the Fourier plane. (d) Varying the spatial period and the orientation of the SLM grating sets the opening angle and the relative orientation of the beams with respect to the normal of the sample plane.

The opening angle of the two incident beams and their orientation with respect to the normal to the sample plane is tunable by varying the spacing period and orientation of the grating on the SLM. The correspondence between the grating period from the SLM and the opening of the two incident beams is summarized in Table 2.2 in Appendix 2.5.6.

The incident beams propagate in the plane perpendicular to the sample stage and the polarization of each beam is controlled by a zero-order half-wave plate (Thorlabs, WPH05M-1030) placed before the objective. For each beam, a polarization parallel to the incident plane is defined as y, (or P) and a polarization perpendicular to the incident plane as x (or S) (Figure 2.12). We use the same notation to characterize the orientation of the analyzer in the detection path.

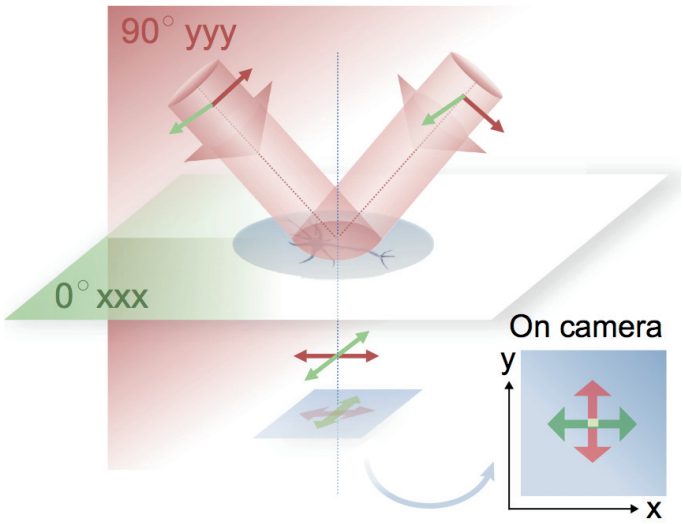

Figure 2.12: Polarization configuration of the two incoming beams. An excitation with a detection along x is noted first xxx (or SSS) and an excitation and a detection along y is noted yyy (or PPP). On the camera, a y polarization is projected along the y axis and a x polarization along the x axis.

The generated SH light or two-photon emission fluorescence was collected in the forward direction using a high numerical aperture Olympus, LUMFLN 60x1.1NA objective and analyzed with an analyzer placed in the collection path after a 515 nm band pass filter (Omega Optical, 10 nm bandwidth) or 550/10BP (Omega Optical, 10 nm bandwidth) filter respectively. The sample stage, controlled by actuators, has a 5 cm travel range in x and y (Asi Imaging, PZ-2000) and a 300-µm

travel range in z, controlled by a piezoelectric stage. The objective lenses are mounted on single axis actuator stages (Asi Imaging, LS-200) and the microscope cage on which all the stages and optics are mounted is a modular microscope system (Asi Imaging, RAMM). Imaging was performed with a gated detection on a back-illuminated electron-multiplying intensified charge-couple device (Bf GEN III, EM-ICCD, PiMax4, Princeton Instruments) with a 512 x 512 pixels chip. The microscope also integrates a path for phase contrast imaging with white light.

The transverse HWHM resolution (188 nm) was determined by imaging 50 nm diameter BaTiO3 particles on a glass coverslip (refer to section 2.2 for details on the particles and imaging procedure). The maximum HMHM axial resolution, achievable in fluorescence or TPEF imaging was determined by scanning a 300 nm thick aqueous solution of 9-diethylamino-5- benzo[α] phenoxazinone (Nile Red) through the focus. Using a spatial frequency of $\sigma = 0.83\ \mu m^{-1}$ we obtain an axial resolution of 520 nm. Compared to our previous 2D wide-field microscope described in the first section of this Chapter, the resolution in the transverse direction is improved by a factor >2, and the Z-sectioning ability is new. Compared to an in-house Leica TSC SP5 commercial scanning confocal multiphoton microscope, used to measure the same spot on the same sample operated with the same pulse duration, wavelength and NA, the transverse resolution is improved by a factor of ~1.4.

2.3.2 3D imaging

To achieve 3D imaging and to improve the transverse spatial resolution[202], we used an adapted HiLo imaging procedure[203–206] that relies on partial spatial coherence introduced by a chirp in the illuminating pulse. HiLo procedures are based on Fourier filtering and are regularly applied for fluorescence imaging. The fluorescent sample is illuminated with an intensity pattern that is typically created by the interference of two coherent beams. Such interference creates an intensity pattern in the transverse and in the axial direction as illustrated in Figure 2.13. When imaging a fluorescent sample that emits fully incoherently, only the transverse intensity pattern remains visible in the image space. The axial intensity pattern disappears everywhere in the image space except at the image plane, which is the only place where the image of the transverse intensity pattern is visible. Only at the image plane the light from the incoherent sample sources come into phase to create the image of the intensity pattern. This means that for incoherent emission, the visibility of the pattern decays rapidly in the axial direction away from the image plane as illustrated in Figure 2.13. The extent of this decay, which in the incoherent case depends only on the angle between the interfering beams[204], dictates the HiLo axial resolution. A rapid decay is thus essential to obtain cross-sectioned images with high axial resolution.

In the case of partially or fully coherent emission, the visibility of the interference pattern along the axial direction in the image space depends on the degree of coherence of the emitted light. As illustrated in Figure 2.13 the interference pattern persists throughout the axial extent if the emitted light is fully coherent, while the pattern is visible to a certain extent if the emitted light is partially coherent. Cross-sectioning is not possible with the HiLo method in the case of fully coherent emission. In the case of partially coherent emission, HiLo imaging may still be performed but with a lower axial resolution than in fluorescence imaging and if the side lobes can be neglected. In the partially coherent case, the axial resolution depends on the angle between the beams but also on the degree of coherence of the emitted light.

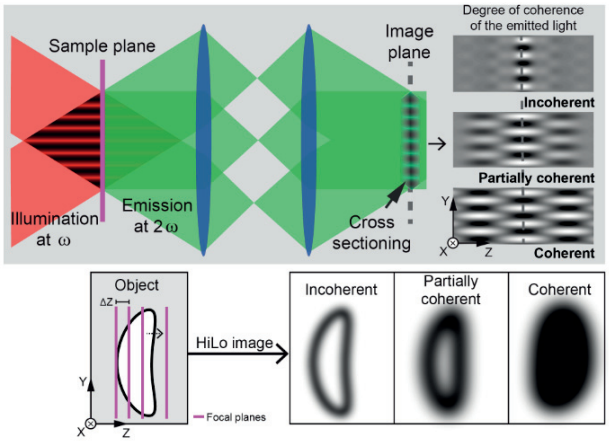

Figure 2.13: Illustration of the 3D HiLo imaging process. Figure taken from supplementary materials of Macias et al.[207]. The axial resolution is expected to vary with the amount of coherence in the emitted light. For incoherent emission a good axial resolution is achievable. For fully coherent emission, no axial resolution is achievable. For partially coherent light an improved axial resolution is expected. The right-hand images illustrate the type of interference pattern that is obtained, and the bottom panel illustrates the effect of no, partial, or complete coherence on the appearance of an image.

2.4 Neuro-imaging

2.4.1 System and characterization

To maintain the cells in a physiological environment while imaging them, we implemented a system to bring a constant flow of fresh extracellular solution with a pump from Harvard Apparatus (PHD 20000). The regular physiological solution used for cell imaging consists of 140 mM NaCl, 3 mM KCl, 3 mM $CaCl_2 \cdot 2H_2O$, 2 mM $MgCl_2 \cdot 6H_2O$, 5 mM glucose and 10 mM Hepes (noted as HEPES solution in this thesis). A tunable flow rate was chosen at 1 mL/mn associated with a suction speed

of 1.2 mL/mn to provide a laminar flow and to prevent flooding and imaging aberrations. Depending on the experiments, different solutions can be draw from the pump to the cell containing chamber (Figure 2.14a). We used an open-bath chamber (Quick Change Imaging Chamber from Warner Instruments Series 40 RC-41LP) in which coverslips with plated neurons are inserted (Figure 2.14b). The bottom of the imaging chamber is a glass coverslip with plated neurons, on top of which a polycarbonate ring is gently placed. This imaging chamber allows for a maximum liquid content of 3 mL, a laminar flow across the chamber, a rapid exchange of liquid, a short working distance and an open bath. Our microscope also integrates a resistive heating configuration for the sample holder platform in which the sample chamber is placed (Warner instrument QE-1) (Figure 2.14c). Maintaining a constant flow of fresh solution and controlling the temperature of the cells environment are imperative to perform long-term live-cell imaging.

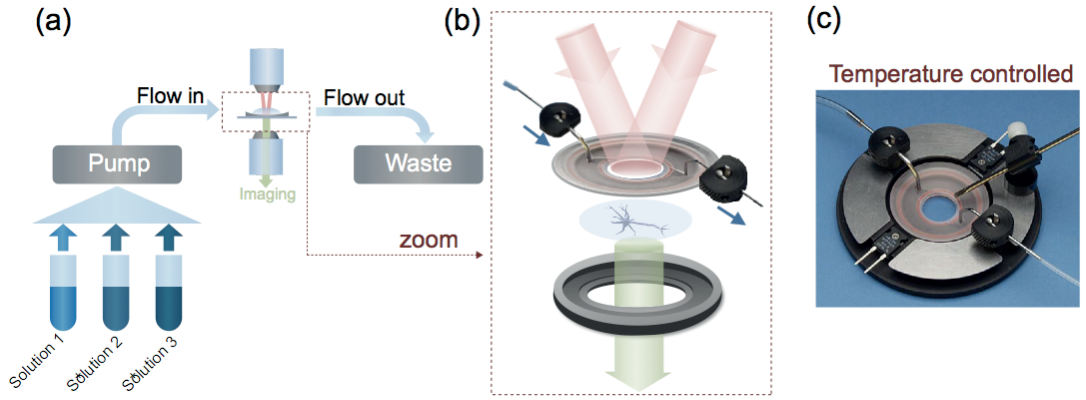

Figure 2.14: Temperature control and constant flow equipment for live-cells imaging. (a) A flow system with a pump (Harvard Apparatus, PHD 20000) brings a constant flow of fresh solution to the open-bath chamber placed under the top objective of the microscope. Different solutions can be chosen to flow in and the outflow leaving the open-bath chamber goes to a waste. (b) an open-bath and quick-exchangeable sample chamber (Warner Instruments, series 40 RC-41LP). (c) A temperature-controlled chamber (Warner instrument QE-1).

A feedback control for the temperature controller is provided via a thermistor, which is inserted into a hole in the base platform of the Warner instrument QE-1 sample holder. Connectors directly attached to the two resistive heating elements of the platform are connected to a heat controller. We characterized the differences between the set temperature on the heat controller, read from the internal thermometer and the actual temperature inside the sample chamber measured with an additional external electronic thermometer (Figure 2.15). The identification of the real temperature inside the sample chamber and the kinetics to reach a certain temperature are important for temperature-sensitive experiments such as neuro-imaging.

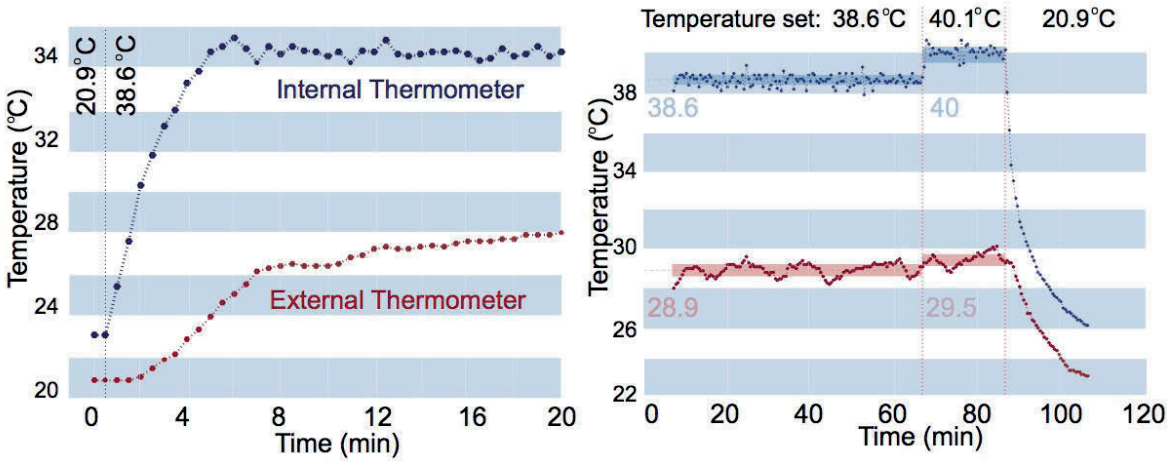

Figure 2.15: Characterization of the temperature inside the open-bath chamber. Characterization of temperatures differences between the set temperature from the control heater (internal thermometer) and the real temperature inside the open-bath chamber (external thermometer) and their relative kinetics as a function of time.

It can be seen that the heater device has a certain inertia, and that there is a difference of approximatively 10 degrees between the internal and external thermometer. Because of this, the heater device was turned 15 minutes prior performing any live-cells imaging experiments and we set the temperature up to 41 degrees in accordance with the internal thermometer display to keep a constant temperature in the chamber around 30 degrees.

2.4.2 Patch-clamp equipment

The 3D wide-field SH microscope integrates an equipment to perform patch-clam measurements (double patch clamp EPC10 amplifier from HEKA Elektronik, Lambrecht, Germany) controlled by PatchMaster software (Figure 2.16a). The software-controlled EPC10 amplifier prevents the addition of any electronic noise from knobs, switches or dials. We used it for recording of whole-cell current clamp measurements. In a current-clamp configuration the EPC 10 USB amplifier acts as a "voltage-follower" similar to microelectrode amplifiers which guarantees very fast and accurate membrane potential recordings. Together with the amplifier, the hardware components of the EPC 10 USB system also contain a headstage (EPC10 USB red star headstage) with a microelectrode holder machined in polycarbonate. This equipment combination is optimized for whole-cell and low noise recordings. The microelectrode holder accepts 2 mm outer diameter (OD) capillaries that are freshly pulled into micropipettes prior to the measurements using a two-step horizontal puller. The size of the micropipettes is characterized by their tip resistance, typically in the range of 5-7 MΩ. For whole-cell current-clamp recordings, the intracellular (patch pipette) solution (Intracellular buffer,

Fivephoton biochemicals) contains (in mM): 140 NaCl, 10 Na_2HPO_4, 2 KH_2PO_4, 3 KCl, pH 7.3±0.1, with an osmolarity of 290±10 mOsm. As a reference electrode connected to the headstage, we used a pellet electrode (Warner Pellet E206) placed into the liquid of the cell-containing open-bath chamber. The large distal tip of the electrode, made out of pure silver embedded into an Ag/AgCl matrix is suited for probing bioelectrical recording with noise reduction.

Due to the tight configuration of our microscope (Figure 2.16b) and the 3 kg weight limit of the piezo stage in which the microscope slide is inserted, a specific micromanipulator was required. We selected the triple axis SENSAPEX micromanipulator (39x87x77 mm SMX, R-FS-50, i39x87x77 mm in size and a weight of 295-370 g) which fits our constrained environment. This micromanipulator offers a displacement range of 20 mm with 7 nm resolution in (x,y,z). Despite its small size, the operating principle of this micromanipulator based on a linear piezo-drive offers a high precision and stability. In order to reduce the load on the piezo stage we used an intermediate cable configuration between the headstage and the microelectrode holder (SENSAPEX SMX-IM-BNC) (Figure 2.16c-e). This configuration provides a complete compact patch-clamp recording system without any additional noise. The micromanipulator displacement is remotely controlled by a rotary knob controller (SENSAPEX SMX-CUK3) with a stand-alone battery which allows for long time experiments and electric noise reduction. To reach the middle of the sample stage, we modified the headstage of the micromanipulator (Figure 2.16c-e).

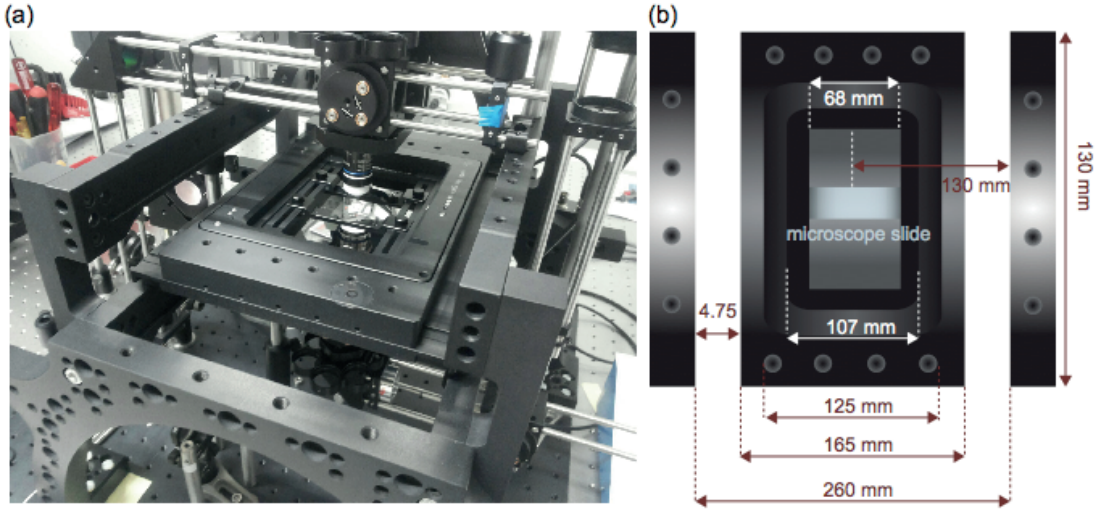

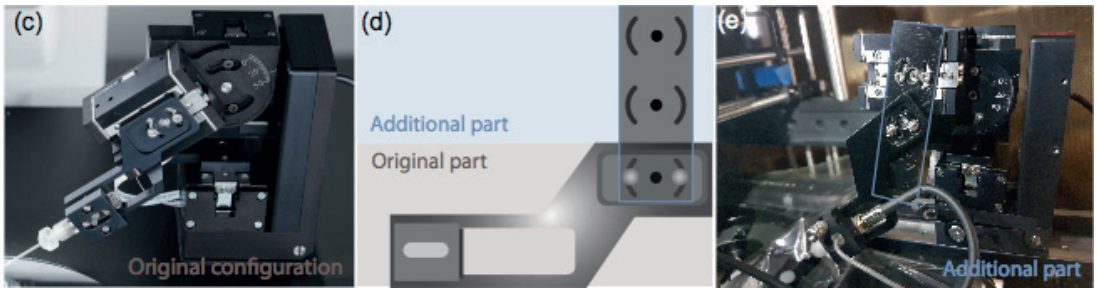

Figure 2.16: 3D wide-field SH microscope and adapted patch-clamp equipment. (a) the overall layout of the microscope, (b) dimensions of the restricted space with the sample stage characteristics, (c) the original configuration of the micromanipulator, (d) schematic of the additional part added to the micromanipulator, (e) the modified micromanipulator used in our experiments with the intermediate cable extension.

2.4.3 Cell cultures protocol

Primary cultures of cortical neurons come from the Laboratory of Neuroenergetics and cellular dynamics. The cultures were prepared from E17 OF1 mice embryos of either sex. Briefly, embryos were decapitated, and brains removed and placed in PBS-glucose. Cortices were removed under a dissecting microscope and collected in a small Petri dish in PBS-glucose. A single-cell suspension was obtained by gentle trituration with a fire-polished Pasteur pipette in Neurobasal medium supplemented with B27 and GlutaMAX (Invitrogen, phenol red free). Cells were plated at an average density of 15,000 cells/cm^2 in supplemented Neurobasal medium on polyornithine-coated glass coverslips (20 mm diameter). After 3–4 h, coverslips were transferred to dishes with supplemented Neurobasal medium. Neurons were maintained at 37°C in a humidified atmosphere of 95% air/5% CO_2 and were used at different days *in vitro* (DIV) depending on the experiments**.**

2.4.4 Primary viability test on living neurons

Prior to every imaging experiments, we checked the viability of neurons by mapping their morphological response to a solution enriched in K^+ as imaged by phase contrast imaging (Figure 2.17a). The protocol consists of flowing a HEPES solution for 1 minute, then switching to a 50 mM K^+ enriched solution in the chamber for 2 minutes and then switching back to a HEPES solution for 5 minutes. Meanwhile, the PC images are recorded with a frame rate of 83 Hz. When subjected to changes in the extracellular ionic strength, the neurons trigger mechanisms to readapt to the environment. This adaptation leads to inward or outward flux of electrolyte solutions, leading to swelling or shrinking of cells[208] (Figure 2.17b). After switching to the K^+ enriched solution, we observed swelling of neurons and when the solution was replaced back to a HEPES solution we observed a shrinking as expected for alive and electrically active neurons[7].

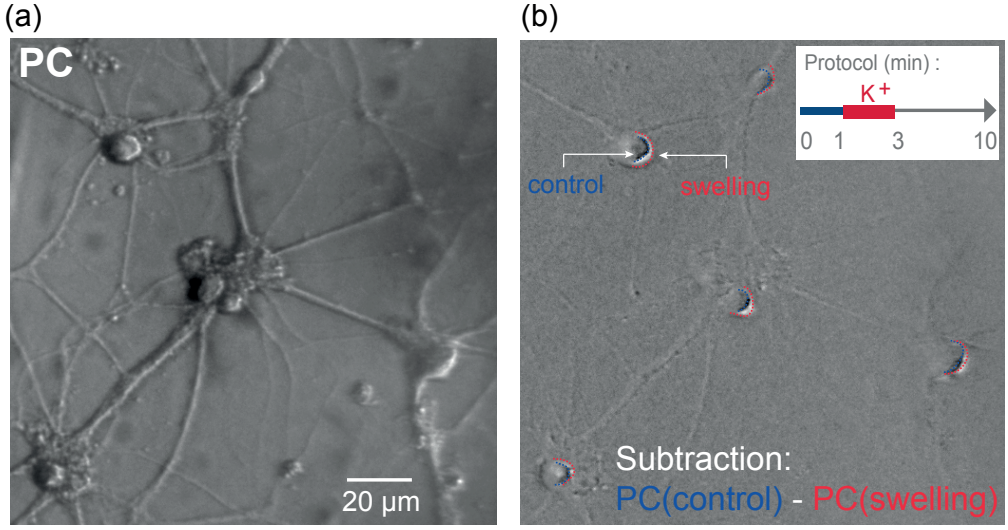

Figure 2.17: Viability test. (a) Phase contrast image of cultured neurons 8 days in vitro (8DIV). The image is an average of 20 frames (0.6 s/frame). (b) Response of the neurons to K^+ enriched solution. Subtraction of an average of 10 frames during the swollen state to 10 frames taken during the control state. The red dotted line indicates the contour of the cell bodies during the swollen state, and the blue dotted line indicates the contour of the cell bodies when they are not swollen. The inset shows the protocol.

Another indicator of alive and dead cells appears to be the SH response itself: cells that have been identified as dead cells by a combination of phase contrast imaging and their absence of response to a to a K^+ enriched solution, are not anymore SH active. Figure 2.18a shows phase contrast image of a healthy cell. Figure 2.18b shows SH intensity emission from all the different morphological parts of the neuron. Figure 2.18c shows a phase contrast image of deceased neurons (29DIV). The SH image in Figure 2.18d shows that the SH intensity has also dropped considerably.

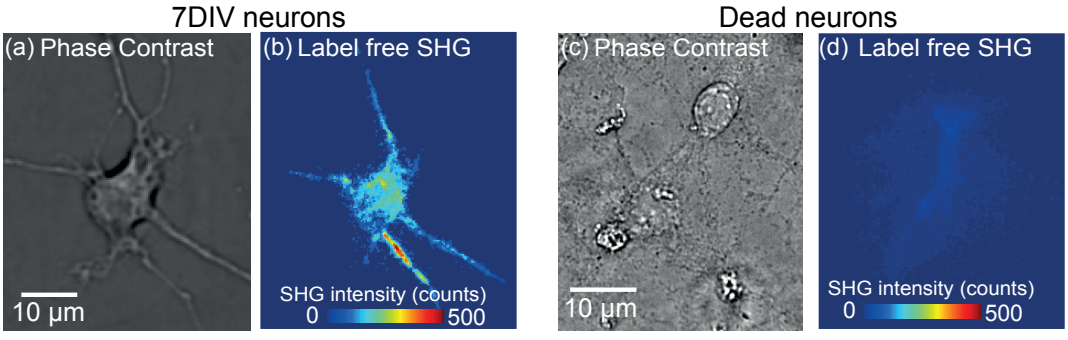

Figure 2.18: SH images from healthy cultured neurons (7DIV) and from dead neurons (29DIV). (a) Phase contrast (PC) image of a neuron at 7DIV. (b) SH image recorded in xxx and yyy polarization combinations and added together. The acquisition time of this image was 10 s. SH intensity is observed from the cell body and the surrounding neurites. (c) Phase contrast image of dead neurons in culture at 29DIV. (d) SH image recorded in xxx and yyy polarization combinations, added together and with the same imaging

parameters and conditions used for (a). The acquisition time of this image was 10 s. Hardly any SH intensity is observed from these neurons.

2.5 Appendix

2.5.1 Particle characterization

The particles were characterized with transmission electron microscopy (TEM) and dynamic light scattering (DLS). Figure 2.19a shows the average (n= 30) DLS result for a solution (3 µg/ml) of $KNbO_3$ particles. The mean diameter is 107 nm, with a PDI value of 0.12. Figure 2.19b-e shows additional TEM images single particles (b), (c) and of several particles (d), (e). It can be seen that the TEM size is somewhat smaller than the DLS size, and that the shape is irregular. Since the size distribution is narrow and since the hydrodynamic radius is needed for the calculation of the rotational and translational diffusion coefficients, we approximate the particle shape as spherical in our model.

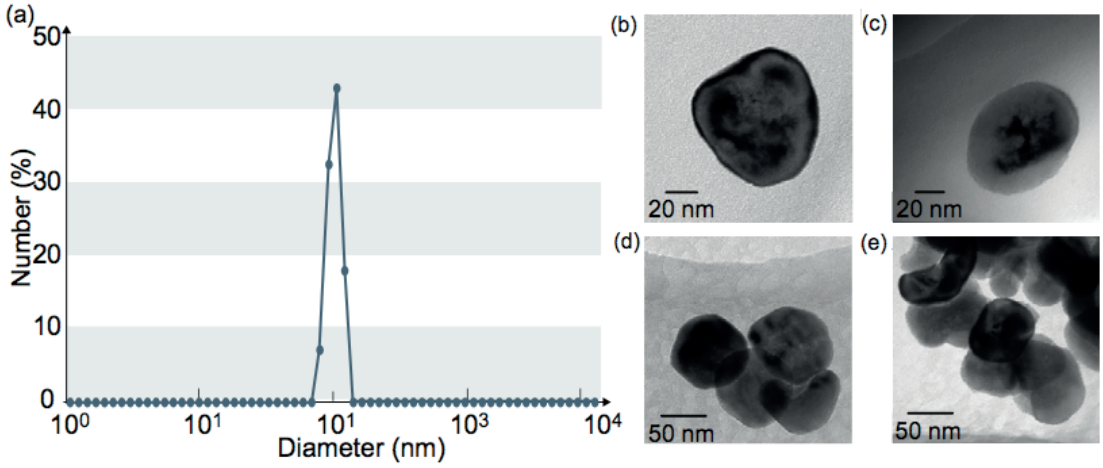

Figure 2.19: Particle characterization. (a) Three series of dynamic light scattering measurements of the KNbO3 particles. (b-e) Transmission electron microscope images of the KNbO3 particles.

2.5.2 Particle electroporation in HeLa cells

To verify that the particles are present within the cell after electroporation, we have measured two-color confocal images of cells that have their lipid content stained with Nile red. The electroporated cells were fixed using 4% paraformaldehyde at room temperature during 10 minutes. Subsequently, the lipid content of the cells was stained with Nile Red. A solution of Nile Red (1 mg/ml in DMSO) was diluted 1:10 000 in PBS and then added to the cell cultures for 5 minutes. After staining and washing, the fixed cultures were mounted on a microscope slide using a PBS solution. The images were then produced in a Leica SP5 MP confocal microscope (1030 nm, 190 fs, 6 mW, 80 MHz) using a 60x (1.2 NA) water immersion objective lens. Figure 2.20 shows a montage of the stack of images through the cell 267 nm apart. The two photons signal from the stained lipid content, measured in

reflection mode (using a built-in monochromator set to detect from 600 to 660 nm), is shown in the red channel, and the second harmonic signal of the particles, measured in transmission mode (using a 0.9 NA condenser and a 525 +\- 25 nm Chroma filter) is shown in the green channel. Each image was scanned at 1000 Hz per line accumulating 10 lines and with 512 x 512 pixels per image. The center of the stack is depicted by the white star. From the 3D stack it can be seen that the particles are located inside the cell.

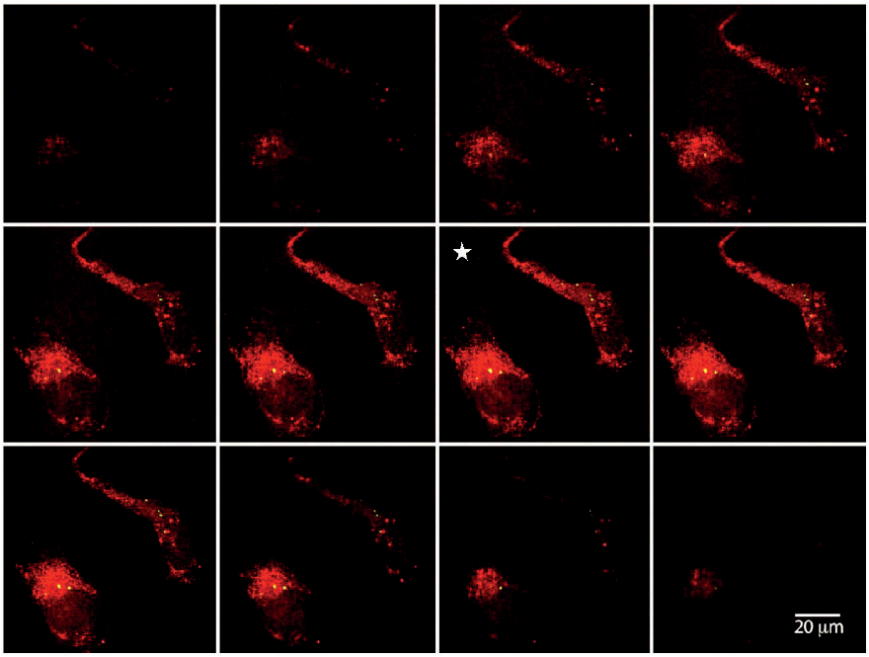

Figure 2.20: Two photon fluorescence and second harmonic confocal image stack of electroporated cells. The fluorescence channel is shown in red and displays the lipid content of the cell, and the second harmonic channel is shown in green, which displays the $KNbO_3$ particles. It can be seen that the particles are inside the cell. The star indicates the center of the stack.

2.5.3 Particle tracking

The single particle tracking was performed using the TrackMate imageJ plugin as shown by Jaqaman et al.[209]. Trajectories were reconstructed using a gap closing maximum distance of 4.5 µm, a maximum linking range of 2 µm, the gap closing maximum frame was 0.82 s. The mean-square displacements (MSD) were calculated at each time value for each particle using a MATLAB algorithm[210] in which spherical geometry for the particle is assumed. The diffusion coefficient was found from averaging the slope values of the lines fitted to 15% of the MSD data, as it is common practice.

2.5.3 Polarization measurements of fixed particles

To estimate the magnitude of the intensity changes and to verify that the particles are single crystalline, we imaged particles fixed on a coverslip illuminated with linearly polarized light under different angles θ. The $KNbO_3$ particles were fixed between two coverslips with an optical adhesive (Norland 61). The curing time was 30 seconds using a Thorlabs UV curing LED system. Figure 2.21a shows the mean SH intensity averaged over all polarization angles. Figure 2.21b shows the intensity changes for a bright and a darker particle as a function of polarization angle. It can be seen that the curve is approximately sinusoidal and that the intensity scale varies from 1-10 (for the brighter particle). These intensity changes are of the same order of magnitude as the ones shown in Figure 2.21b. The mean signal over all polarization angles of the first derivative in θ of the SH signal is shown in Figure 2.21c. The derivative of the intensity is uniform across the particles in the image. This corroborates that there is likely no clusters present. Note that because the particles are fixed with their crystal axis lying in different planes, varying the angle of the polarization does not guarantee the same maximum intensity for all particles in this figure.

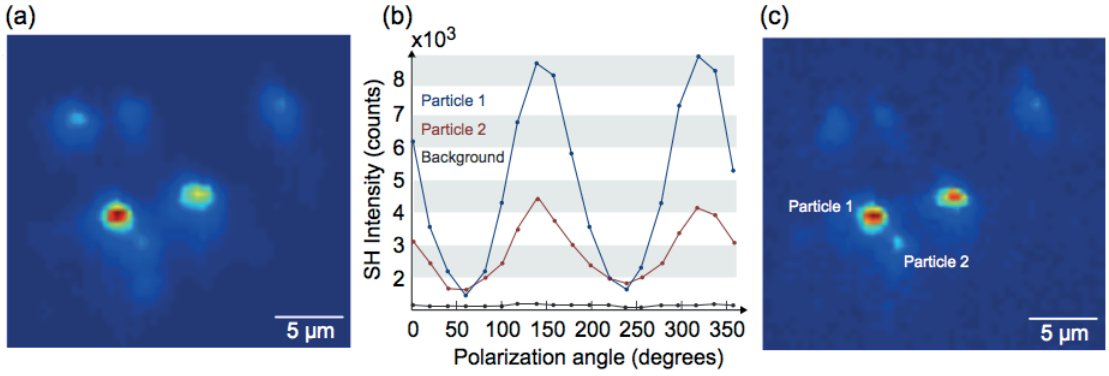

Figure 2.21: Polarization characterization of the nanodoublers. Figure taken from Macias et al.[211]. The mean SH intensity (over all angles) is shown in (a). The SH intensity as a function of the incident polarization angle θ is shown in (b). The mean signal over all polarization angles of the first derivative in θ of the SH signal is shown in (c).

2.5.5 Nanoparticles orientation analysis

To perform the rotational tracking, an expression to relate the intensity and orientation of the crystal principal axis was derived. An MSD algorithm[210] (in which spherical geometry is assumed) was then used on the obtained orientations to calculate the mean square rotation. Three successive rotations relative to the three major coordinate axes are used to estimate the orientation of the principle crystalline axis (C) of the particles with respect to the two beams polarization orientation. We assume that the direction of the electric field is fixed in the laboratory frame with a polarization perpendicular

to the sample plane. The two incoming beams are in the plane of incidence perpendicular to the sample plane forming an angle of -45 and 45 degrees with respect to the normal to the sample plane. With these assumptions and for a given particle with the orientational angles θ, ϕ, and φ between the principal axis (c) and the lab frame z axis (Figure 2.22a-b), the SH intensity (Figure 2.22c), as a function of the orientation angles can be expressed as:

$$I(\theta, \phi, \varphi) = \left|\bar{\bar{D}} \cdot \bar{A}(\theta, \phi, \varphi)\right|^2 \tag{2.3}$$

where $\bar{\bar{D}}$ associated to the matrix representation of the nonlinear susceptibility tensor $\chi^{(2)}$ of the single axis nanoparticle. The single axis of the $KNbO_3$ particle is set along the z direction, thus the stronger tensor component of the single-axis $KNbO_3$ particle is $\chi^{(2)}_{zzz}$. As a result, in the following calculations of the electric field's projection in the crystal's referential, only the components along z will be considered. The directional squared electric field $\bar{A}(\theta, \phi, \varphi)$ is defined as:

$$\bar{A}(\theta, \phi, \varphi) = \begin{bmatrix} E_{x1}E_{x2} \\ E_{y1}E_{y2} \\ E_{z1}E_{z2} \\ E_{y1}E_{z2} + E_{z1}E_{y2} \\ E_{x1}E_{z2} + E_{z1}E_{x2} \\ E_{x1}E_{y2} + E_{y1}E_{x2} \end{bmatrix} \tag{2.4}$$

The general expression of the electric fields associated with the two non-collinear beams $\bar{E}_i(\theta, \phi, \varphi)$ with $i = 1,2$ (for the first and second beam) in the coordinate system of the particle is:

$$\bar{E}_i(\theta, \phi, \varphi) = \begin{bmatrix} E_{xi}(\theta, \phi, \varphi) \\ E_{yi}(\theta, \phi, \varphi) \\ E_{zi}(\theta, \phi, \varphi) \end{bmatrix} \tag{2.5}$$

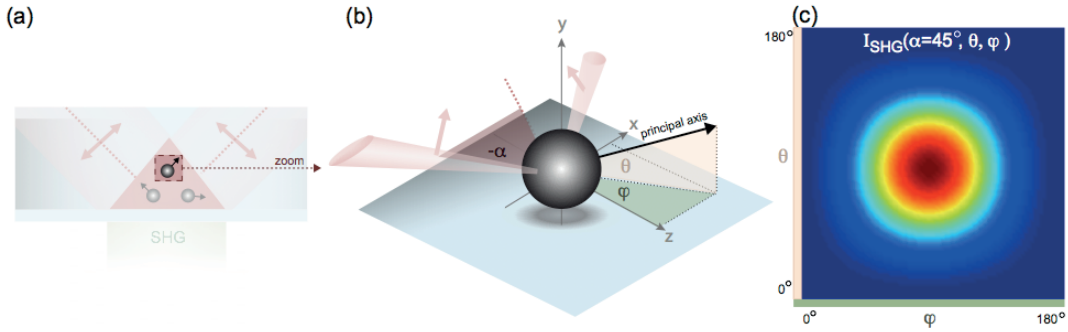

Figure 2.22: Imaging configuration and SH intensity from the nanoparticles in the chamber. The side view of the configuration of the particles and beam geometry is shown in (a). The orientation of the particle with respect to its principal axis is shown in (b). The intensity as a function of θ and φ for an opening angle of α = 45 degrees is given in (c).

To transform the coordinate system of each beam into the coordinate system of the particle one can write

$$\bar{E}_i(\theta,\phi,\varphi) = \bar{\bar{M}}_1(\theta)\cdot\bar{\bar{M}}_2(\phi)\cdot\bar{\bar{M}}_3(\varphi)\cdot\bar{\bar{M}}_4(\alpha), \tag{2.6}$$

where the rotation matrices are defined as

$$\bar{\bar{M}}_1(\theta) = \begin{bmatrix} 1 & 0 & 0 \\ 0 & cos(\theta) & -sin(\theta) \\ 0 & sin(\theta) & cos(\theta) \end{bmatrix}, \qquad \bar{\bar{M}}_2(\phi) = \begin{bmatrix} cos(\phi) & -sin(\phi) & 0 \\ sin(\phi) & cos(\phi) & 0 \\ 0 & 0 & 1 \end{bmatrix},$$

$$\bar{\bar{M}}_3(\varphi) = \begin{bmatrix} cos(\varphi) & -sin(\varphi) & 0 \\ sin(\phi) & cos(\phi) & 0 \\ 0 & 0 & 1 \end{bmatrix}, \qquad \bar{\bar{M}}_4(\alpha) = \begin{bmatrix} 1 & 0 & 0 \\ 0 & cos(\alpha) & sin(\alpha) \\ 0 & -sin(\alpha) & cos(\alpha) \end{bmatrix}.$$

Assuming a $KNbO_3$ crystal is spatially symmetric around ϕ we can write

$$\begin{aligned} I(\theta,\phi) \sim 324|cos\theta\ cos\varphi \sin\varphi|^2 + 676|sin\theta\ cos\varphi \sin\varphi|^2 \\ +2|3\ cos2\varphi + cos2\theta\ sin^2\varphi|^2, \end{aligned} \tag{2.7}$$

which can be further approximated by neglecting the small contribution of the high frequency variations to yield

$$I(\theta,\varphi) \propto |sin^2(\theta)sin^2(\varphi)|^2 \tag{2.8}$$

Moreover, since φ and θ are indistinguishable, the intensity can be written as $I(\theta') = C|sin^2(\theta')|^2$, where C is a proportionality constant, and θ' is the angle. The mean square angular displacement for a spherical single-axis nanoparticle is obtained by inserting the above equation into an MSD algorithm[210] assuming spherical geometry. The error in the analysis is displayed in Figure 2.21.

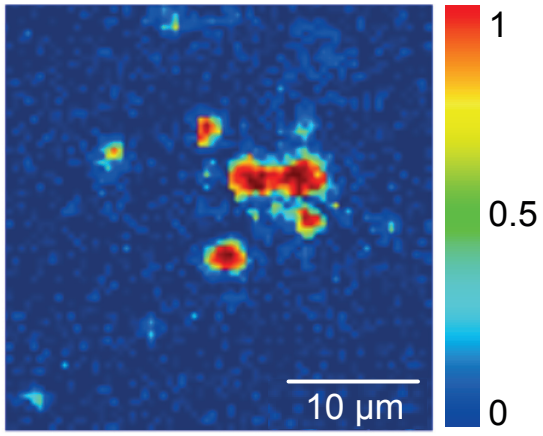

Figure 2.23: R^2 values relative to the rotational diffusion MSD analysis. r^2 values for the fitting of the rotational diffusion shown in Figure 2.9b.

2.5.5 Calculation of fluence and energy deposit on the sample plane

We write the pulse energy, power at the sample plane, the fluence and peak intensity,

$$\text{Pulsed energy at sample} = \frac{\text{Power average at sample}}{\text{f}},$$

$$\text{Power at sample stage} = \frac{\text{Power at Fourier plane}}{2},$$

$$\text{Fluence} = \frac{\text{Power at sample stage}}{\text{f. A}} \times 10^3,$$

$$\text{Peak Intensity} = \frac{\text{Power at sample stage}}{\text{f. A.}\tau}$$

The repetition rate *f*, is 200 kHz, the pulse duration τ is equal to 168 fs, and the illumination area, A is $1.5\text{x}10^{-4}\text{cm}^2$. With these experimental parameters, we calculate the above-mentioned energy and power as a function of the percentage of transmission laser output. The results are shown in Table 2.1.

Laser trasnmission	Laser output (W)	Fourier's plane (W)	Before BS (W)	After BW (W)	Pulse energy at sample (J)	Power at sample (W)	Fluence at sample (mJ/cm2)	Peak intensity at sample (GW/cm2)
100%		0.171	2,112	0.8	4.28×10^{-7}	0.085	2.778	16.96
90%		0.16	1,975	0.77	4×10^{-7}	0.08	2.599	15.87
80%		0.145	1.803	0.70	3.6×10^{-7}	0.072	2.356	14.38
70%	2.78	0.129	1.607	0.63	3.2×10^{-7}	0.064	2.096	12.79
60%	2.39	0.11	1.397	0.55	2.8×10^{-7}	0.056	1.819	11.11
50%	2	0.09	1.187	0.46	2.3×10^{-7}	0.047	1.527	9.32
40%	1,62	0.07	0.964	0.37	1.9×10^{-7}	0.038	1.235	7.54
30%	1,24	0.06	0.738	0.28	1.4×10^{-7}	0.028	0.926	5.65
20%	0.85	0.04	0.505	0.19	0.9×10^{-7}	0.019	0.617	3.77
10%	0.44	0.02	0.263	0.1	4.7×10^{-8}	0.009	0.309	1.88

Table 2.1: Correspondence between laser output power and the different energy distributions at the sample stage. The power at the exit of the laser, at the Fourier's plane, before and after the beam splitter (BS) were measured with an external power meter. A safe fluence[160] corresponds to a laser output power of 2.78 W.

All experiments described in the following sections and chapters were performed with a percentage output power laser of 70% corresponding to an output laser power of 2.8 W. This value, according to previous studies[160,212], is safe for live-cell imaging (bellow 13 GW/cm^2).

2.5.6 Correspondence between the SLM period and the opening angle of the incident beams

The spatial light modulator (SLM) is used as a reflecting grating. The spatial frequency of a grating is defined such as:

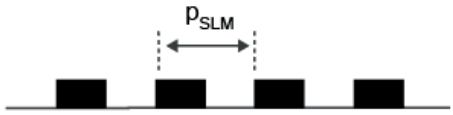

$$sin\theta_{SLM} = \frac{\lambda n}{p_{SLM}}$$

With θ_{SLM} the angle of the beam after hitting the SLM, p_{SLM} the spatial frequency of the SLM, λ the wavelength of the beam hitting the SLM and n the first orders (-1 and +1) diffracted by the SLM as a grating.

Our imaging system, from the SLM to the back focal plane of the top objective can be represented by a combination of several lenses with different focal length. The SLM plane, the Fourier plane between L7 and L8 (green dotted line) and the back focal plane of the objective are conjugated.

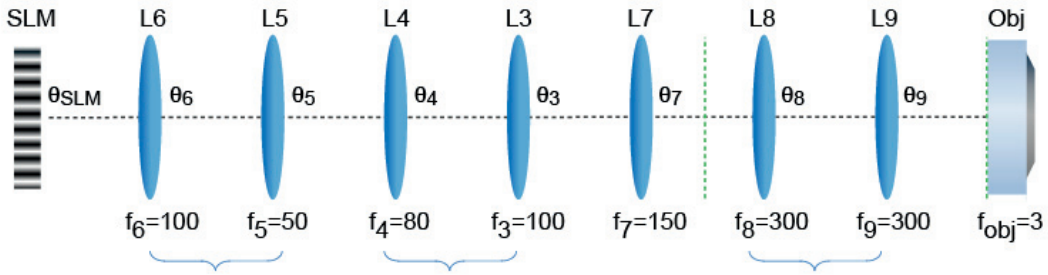

We calculate the correspondence between the angle with which the beams are diffracted by the SLM (θ_{SLM}) and the angle with which the beams hit the sample plane, after recombination with the top objective (θ_{obj}).

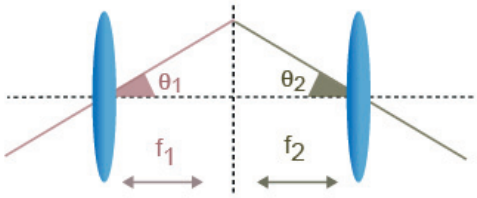

$$f_1 sin\theta_1 = f_2 sin\theta_2$$

The magnification between L8 and L9 is 1. We write the expression of θ_{SLM} as a function of the successive focal lengths and the angle between the two incident beams:

$$sin\theta_{SLM} = \frac{f_5}{f_6} \times \frac{f_3}{f_4} \times \frac{f_{obj}}{f_7} \times sin\theta_{obj}$$

$$sin\theta_{SLM} = \frac{1}{80} \times sin\theta_{obj}$$

On the Fourier plane, the period of the SLM is

$$p_{image} = \frac{\lambda}{2sin\theta_{obj}}$$

We express θ_{obj} as a function of p_{SLM}:

$$p_{SLM} = \frac{80 \times \lambda}{sin\theta_{obj}}$$

$$sin\theta_{obj} = \frac{80 \times \lambda}{p_{SLM}}$$

The period of the SLM is in µm and the correspondence into pixels is:

$$p_{SLM}\ (in\ \mu m) = p_{SLM}\ (in\ pixels) \times 8$$

Finally:

$$\theta_{obj} = sin^{-1}\left(\frac{10 \times \lambda}{p_{SLM}(in\ pixels)}\right) \tag{2.9}$$

Period on SLM (pixels)	Opening angle (deg.)	Period on SLM (pixels)	Opening angle (deg.)	Period on SLM (pixels)	Opening angle (deg.)	Period on SLM (pixels)	Opening angle (deg.)
6	59.1	11	27.9	16	18,9	21	14.2
7	47.36	12	25.4	17	17.6	23	12.9
8	40.1	13	23.3	18	16.6	25	11.9
9	34.9	14	21.6	19	15.7	30	9.9
10	31	15	20.1	20	14.9	35	8.5

Table 2.2: Correspondence between the angle of the two incoming beams and the generated period on the SLM. The total opening angle between the two incident beams is in degrees and the generated period on the SLM is in pixels.

Chapter 3
Mapping of morphological changes in the neuronal cytoskeleton with endogenous second harmonic imaging: a case study of nocodazole

In this Chapter, we demonstrate the use of wide field high throughput second harmonic (SH) microscopy for investigating cytoskeletal morphological changes on the single cell level. The method allows for real-time long term in-vitro label-free measurements of cytoskeletal changes that can under certain conditions be quantified in orientational distribution functions ore changes in the number of microtubules. As SH generation is intrinsically sensitive to non-centrosymmetrically structured microtubules but not to isotropic or centrosymmetric materials we use it to probe the microtubule structure in the cytoskeleton when it undergoes dynamical changes induced by the application of nocodazole. Nocodazole is a microtubule destabilizing drug that reversibly depolymerizes microtubules. SH polarimetry measurements demonstrate how the orientational directionality of microtubules in neurites and cell bodies can be determined label-free. Real-time nocodazole induced morphological changes in neurons of different age and in a single axon are also demonstrated using spatiotemporal SH imaging.

3.1 Introduction

Microtubules are highly dynamic polymers[22] that constitute a major component of the cytoskeletal network of neuronal cells. They are versatile structures capable of polymerizing and depolymerizing[23,24] . Microtubules play an essential role in morphogenesis and are part of numerous cytoplasmic structures[6]. Microtubules are spatially non-centrosymmetric hollow cylinders that are composed of α/β-tubulin dimers[7,214]. In axons of morphologically polarized neurons, microtubules are uniformly oriented in tightly packed bundles[9](refer to Chapter 1 for more details). In contrast, a less uniform directional distribution is present in dendrites[12,215]. To understand the complexity, growth, maintenance and remodelling of the microtubule bundles and thus the cytoskeleton, knowledge of the regulation of microtubule dynamics is important. A variety of drugs are available that can assist with this. In this respect nocodazole is a valuable tool[216]. Nocodazole is a microtubule-specific drug[217] that causes microtubule depolymerization by binding to free tubulin dimers and preventing them from incorporating into microtubules[218]. Used at appropriately high concentration nocodazole interrupts the microtubule polymerization behaviour in a reversible way[64,67,219]. After wash out, microtubules' polymerization occurs without affecting their initial orientation. Nocodazole is often used to probe instability and to uncover microtubule regulation mechanisms in combination with immunofluorescent methods[66].

The dynamics of microtubules *in vitro* was first tracked in 1986 with dark field differential interference contrast microscopy[56]. Immuno-electron microscopy and fluorophore-tagged proteins have also been used to visualize intrinsic and induced microtubule dynamics[57–60,220]. More recently optogenetic modifications or cloned proteins expression in mice[61] and differential interference contrast imaging methods[62] have been used for the investigation of the cytoskeleton.

The necessity to tag microtubules with a label has disadvantages: the difficulty to attach the label specifically and permanently to microtubules, the photo instability induced by the use of a fluorophore, and the harsh interaction of the fluorophore on the chemical reaction of interest[68,221]. In addition, genetic manipulation or differential microscopy have disadvantages from a clinical perspective or have a lack in component specificity. An alternative for microtubule imaging has been recognized and demonstrated in the form of second harmonic microscopy[124,222,223]. In a second harmonic (SH) process two near-infrared photons with frequency ω and field strength $E(\omega)_{j,k}$ (with polarization states j or k) combine into one that has the double frequency 2ω. The optical contrast of a SH microscope is determined by the spatial organization of molecules: A centrosymmetric or isotropic arrangement of molecules does not give rise to any coherent SH emission, while a polar

arrangement of molecules does emit SH photons[224]. This symmetry selection rule generates a unique specificity to non-centrosymmetric structures. Since microtubules are polar they generate SH light, whereas cytoskeletal structures such as actin filaments do not[69]. The SH emission also strongly depends on the way in which microtubules are organized. The intensity in polarization state k ($I(2\omega)_i$) measured in an SHG experiment is given by the absolute square of the second-order nonlinear polarization $P_i^{(2)}(2\omega)$:

$$I(2\omega)_i \sim \left|P_i^{(2)}(2\omega)\right|^2 \text{ and } P_i^{(2)}(2\omega) = \epsilon_0 \chi_{ijk}^{(2)}(2\omega) E_j(\omega) E_k(\omega) \qquad (3.1)$$

$P_i^{(2)}(2\omega)$ can be understood as a charge oscillation in the material that emits photons at the double frequency. The second-order susceptibility $\chi_{ijk}^{(2)}(2\omega)$ is the material response and is given by the orientational average of the responses of the molecular building blocks that make up the material (microtubules), defined by the molecular hyperpolarizability tensor $\beta_{abc}^{(2)}(2\omega)$, with a, b, c the molecular symmetry axes. The second-order susceptibility is given by:

$$\chi_{ijk}^{(2)}(2\omega) = \frac{N}{\epsilon_0} \sum \quad \beta_{abc}^{(2)} \langle R_{ai}(\psi,\theta,\phi) R_{bj}(\psi,\theta,\phi) R_{ck}(\psi,\theta,\phi) f(\psi,\theta,\phi) \rangle_{\psi,\theta,\phi} \quad (3.2)$$

which is the orientational average of the hyperpolarizability tensor elements whereby $f(\psi,\theta,\phi)$ is the orientational distribution function, and ψ, θ, ϕ are the Euler angles[225]. N represents the number of microtubules. Based on the cylindrical symmetry of the system one assumes spatial isotropy around two angles (ψ, ϕ) and directionally around only one orientational angle (θ). For a non-resonant optical process (involving only virtual energy states), there are only two non-zero[226–229] $\chi_{ijk}^{(2)}(2\omega)$ tensor elements, namely $\chi_{yyy}^{(2)}(2\omega)$ and $\chi_{yxx}^{(2)}(2\omega)$. Based on this analysis one can measure the orientational angle of microtubules in a structure by measuring different polarization combinations. One way to obtain the tilt angle of a microtubule segment at a single pixel is to compute the ratio[226–229]:

$$\frac{I(2\omega)_{yyy}}{I(2\omega)_{xxx}} = tan^2(\theta) \qquad (3.3)$$

This analysis thus provides a way to determine the microtubule orientation on a pixel by pixel basis. It does not allow determining the directionality of microtubules. There is one study[230] that provides such information using a combination of SHG and two photon fluorescence from a label. In principle, it would be possible to obtain such information also label-free by using polarization-resolved SH

imaging[231]. This has, however, not yet been applied to neuroimaging. It can also be seen from Eqs. (1-3) that the intensity depends quadratically on the number of microtubules if these are aligned along the same axis. This quadratic dependence is referred to as spatial coherence. This means that axons that have microtubules organized unidirectionally will emit a much stronger SH intensity than structures with a bidirectional organization of microtubules, allowing for identification of the axon by means of the intensity[71]. Thus, in principle SH imaging allows for identification of different parts of the cytoskeleton, and SH polarimetry can be used to determine orientational distributions. As SH imaging requires no immunostaining, such information can be obtained label-free in living neurons in real time. Unfortunately, the relative inefficiency of the nonlinear SH generation process compared to linear fluorescence, has prohibited the wide spread use of SH imaging to map neuronal microtubule-based cytoskeleton and dynamic processes in real time[69,120,232].

In this Chapter, we explore the use of femtosecond wide field medium repetition rate SH imaging[207] for dynamic neuroimaging. The method, as described in Chapter 2, combines an increase in throughput of 3 orders of magnitude of the SH imaging process[201,207] with a low photodamage[212]. We use the well-known interaction of nocodazole with microtubules[213] as an example of a system where spatiotemporal changes are expected. We determine the orientational distribution of microtubules and map the relative intensity of the different structures. We then perform in-vitro imaging of the effect of nocodazole on the axon of a corpus of neurons at different stage of maturity. We observe an overall depletion and recovery of the SH intensity upon nocodazole application and wash-out, consistent with the expected reversible nocodazole-microtubules interactions. We then demonstrate spatiotemporal dynamic SH imaging during and after nocodazole application using image acquisition times of 0.3 ms. The images display a non-uniform degradation and structural recovery of the axonal microtubules. Assuming that the orientational distribution within the axon is unaffected by nocodazole, we convert the SH intensity changes into a change in the number of microtubules present in the structure.

3.2 Materials and methods

3.2.1 Nocodazole treatments

Nocodazole was purchased from Sigma Aldrich (Buchs, Switzerland). A stock solution diluted in DMSO was prepared with a concentration of 5 mg/ml and then diluted in tissue culture medium at a ratio of 1:500 for a final concentration of 10 µg/ml. The tissue culture medium was prepared fresh

prior to the experiment and contained the following concentrations (in mM) 140 NaCl, 3KCl, 3 $CaCl_2 \cdot 2H_2O$, 2 $MgCl_2 \cdot 6H_2O$, 5 mM glucose and 10 mM Hepes (solution denoted as HEPES solution in this work). All chemicals were purchased from Sigma Aldrich. Nocodazole containing medium and the drug-free tissue culture medium were warmed to 37°C before using it at room temperature. Recordings of SH movies started a few seconds after the drug-containing medium was injected in the neurons-containing chamber and were also performed at room temperature. After 2 to 10 minutes, the drug-containing solution was removed from the sample-chamber by pipetting and replaced with a drug-free tissue culture medium. This tissue culture medium was replaced three times following the same procedure by pipetting and re-injection of medium to remove completely any nocodazole residue during the recovering period. The recording of the recovery experiment started after the third rinse and lasted for 10 to 20 minutes depending on the experiments.

3.3 Results and Discussion

3.3.1 The orientational distribution of microtubules

Figure 3.1a shows a phase contrast (PC) image of a cultured neuron at DIV13. The cell body and two neurites that are labeled 1 and 2 are visible in the image. Figure 3.1b shows the SH image recorded with two orthogonal polarization combinations (color coded with green for yyy and red for xxx polarized beams). The inset in Figure 3.2c shows the application of Eq. (3.3) on the obtained data in Figure 3.1b. It can be seen that the neurite 1 has an orientational angles along the X direction (90 degrees), while the neurite 2 has an orientational angle that varies between ~35 and ~60 degrees, indicating that both x and y polarized structures are present. Figure 3.1c shows the angular distribution for neurite 1 and 2 along the mean direction of the neurite orientation obtained from the SH image (Figure 3.1b, arrows are indicated in the figure). It can be seen that neurite 1 contains a narrow angular distribution of microtubule segments fit that are aligned in the direction of the structure, while neurite 2 has a broad orientational distribution that is not directed along the growth direction. The Gaussian fits in Figure 3.1c confirms the broad spread of orientational angles for neurite 2 (standard deviation = 4.3) and a narrower distribution for neurite 1 (standard deviation = 0.76). The ratio of the SH intensity of neurite 1 by comparison with neurite 2 is 1.5, showing a strongest SH intensity in neurite 1. Of all the microtubule containing structures within the cell, the axon is the only one that presents a unidirectional organized array of microtubules, oriented along the growth direction and arranged in parallel ordered bundles[13,27,71,233]. In microtubules, the α/β-tubulin dimer composition induces a dipole along the axial direction of the axonal microtubules bundles. An

excitation parallel to this molecular dipole should lead to a strong SH emission, while excitation perpendicular to the axial direction should result in no SH contrast. Based on the above analysis, we can thus conclude that the structure that has a high SH intensity in combination with a narrow orientational distribution that is directed parallel to the growth direction is the axon (neurite 1), while the other one is a dendrite (neurite 2).

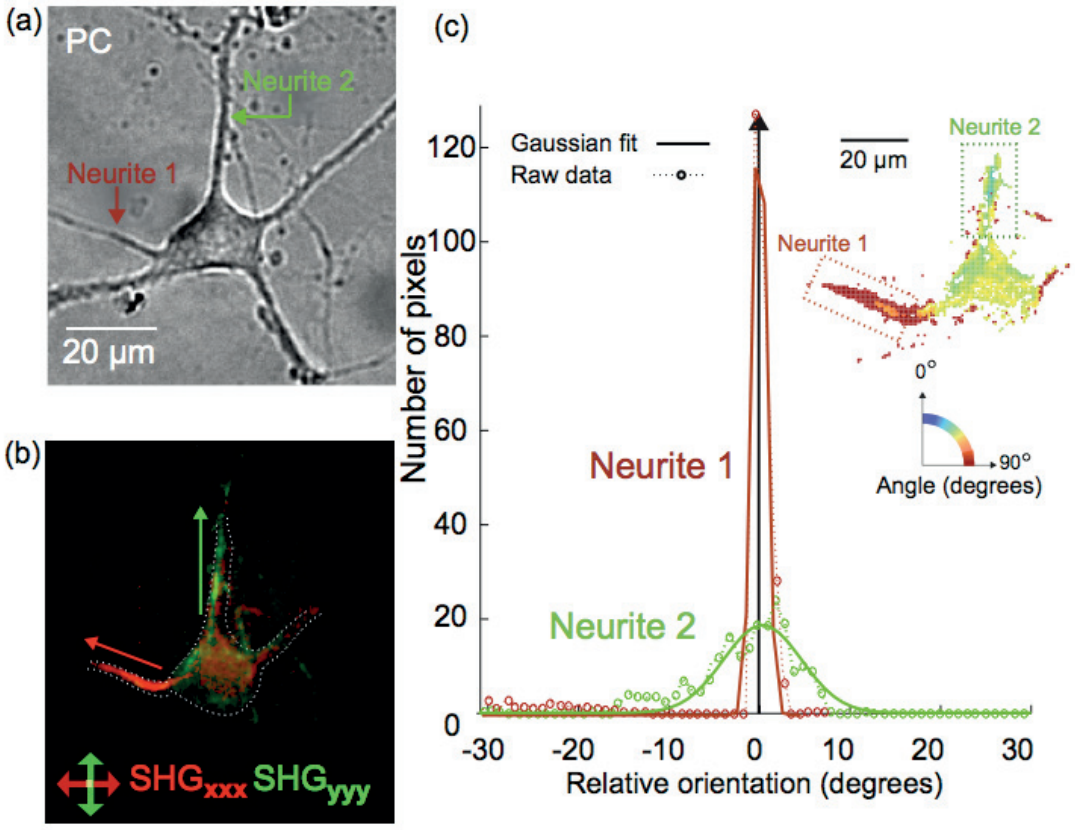

Figure 3.1: The orientational distribution of microtubules from SH polarimetry. (a) Phase contrast (PC) image of a neuron DIV13. The neuron consists of a cell body and 2 neurites. (b) SH images recorded in xxx (red) and yyy (green) polarization combinations. The acquisition time of this image was 18 s for each polarization. (c) The orientational distribution of the neurites is plotted relative to the main axis of the neurite with their respective Gaussian fits. The inset shows a color plot indicating the pixel wise relative tilt angle obtained from applying Eq. (3.3) to the data in panel (b).

3.3.2 SH imaging of microtubule morphology in single neuron

We measure the influence of nocodazole on the SH intensity. Figure 3.2a shows a composite image with phase contrast obtained with PC and SH modalities showing two morphologically polarized neurons at DIV7. At this stage of maturity, neurons have one long and thin process, the axon, and several shorter tapered processes[75,234]. This neuronal morphology is observed in the PC image in

Figure 3.2a. The SH signal, in red in Figure 3.2a, was obtained with the two incoming beams polarized along the vertical direction (yyy, indicated by the red double head arrow). It can be seen that one of the structures in Figure 3.2a generates a brighter SH signal (indicated by the white arrow), while other structures, such as the cell bodies (indicated by the white arrowheads) emit a much fainter SH intensity. We changed the polarization combination of the in- and outgoing beams. Since we only observe an intense SH emission within the structure that could be the axon when it is aligned with one particular polarization orientation, the elongated structure in Figure 3.2a likely corresponds to the axon.

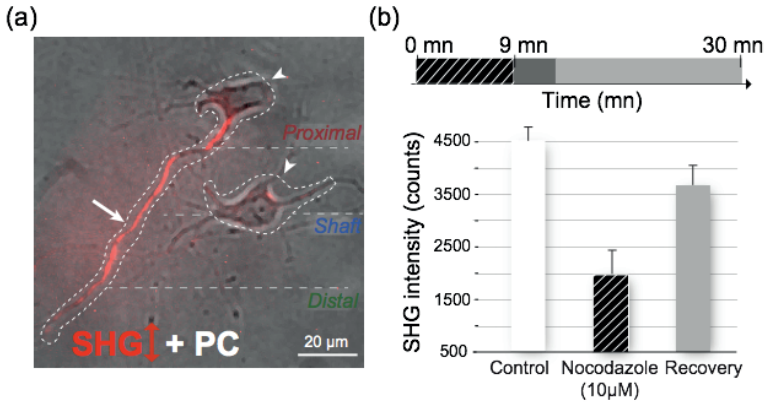

Figure 3.2: **Effects of nocodazole on SH response from microtubules, during application and after washout.** (a) Composite image of the non-polarized white light phase PC of two neurons at stage 3 of their development and label-free SH image (in red). The polarization combination used for the SH image is indicated by the red double head arrow. Arrowheads: cell bodies, arrow: axon. The axon is divided into three parts, proximal, shaft and distal, which will be used for the spatiotemporal SH imaging using the same neuron in Figure 3.4. (b) Top panel: time lapse protocol of the nocodazole application in the wash-out and recovery experiment. Nocodazole (10 µM) was added to the open bath chamber containing the plated neurons (striped shading), 9 minutes later the drug-containing solute was removed and the culture was washed three times with drug-free culture medium (dark gray shading). Recovery lasts 20 minutes after the wash-out (light gray shading). Bottom panel: histograms of the overall SH intensity from the dashed mask averaged for 3 s during the control (no drug added), directly after injection of nocodazole and after a recovery period of 20 minutes.

Nocodazole depolymerizes microtubules and should therefore affect the SH intensity, in accordance with previous studies[69] that showed that SH depletion and recovery follows the application of the depolymerizing drug nocodazole. To investigate the effects of nocodazole on the SH intensity, we applied a 10 µM nocodazole solution in the open bath chamber for 9 minutes and subsequently washed it out. SH images were recorded continuously with 0.3 s per frame. The histograms in Figure 3.2b show the 3s-averaged SH intensity in counts coming from the neurons marked by the dashed mask in Figure 3.2a before and after the application of nocodazole, and at the end of the recovery time. It can be seen that after 9 minutes of drug exposure, the SH intensity arising from the two cells decreases to ~60% of its original value. After 20 minutes following the wash out, the SH intensity

has recovered back to ~80% of its original value in agreement with previous studies[71,124]. As the wide field SH imaging system can be employed to record 0.25 s integration time images, without damaging the cells[212], in what follows we demonstrate two possible applications of SH imaging: To probe morphological drug induced changes for neurons of different age and to dynamically image spatiotemporal changes in real time.

3.3.3 Mapping changes in the microtubule morphology as a function of maturity

Figure 3.3a, shows PC and SH images of neurons at three different stages of maturity, DIV7, DIV11 and DIV22. For each neuron, the displayed SH intensity is averaged over 10 s. Figure 3.3b shows the decrease in signal after application of nocodazole where the first 10 s were taken as a reference (i.e. before nocodazole application). Figure 3.3b shows that newly polarized neurons (DIV7) show a strong response to nocodazole, with a SH depletion of 15 % after 1 minute and a decrease down to 25 % of the original value after 9 minutes. Mature polarized neurons (DIV11) display a slow decrease over a long time, starting from 2.7 % after 1 minute with an SH intensity depletion of 8 % of its original value after 9 minutes of exposure. For advanced mature neurons (DIV23), the SH signal is not changing detectably. This difference in nocodazole sensitivity with age is consistent with a dynamical microtubule cytoskeleton, where at the early stages more and shorter microtubules are present that have many sites to initiate depolymerisation. As neurons mature, microtubules are more inclined to collect post translational modifications (PMT) resulting in an increase of stability[213,235,236]. Thus, the cytoskeleton of older neurons has a better resistance to nocodazole. Although this has not been done in this study, because wide field SH imaging allows for time lapse imaging over long-time intervals, one could potentially use this method to follow the same neuron over extended periods of time.

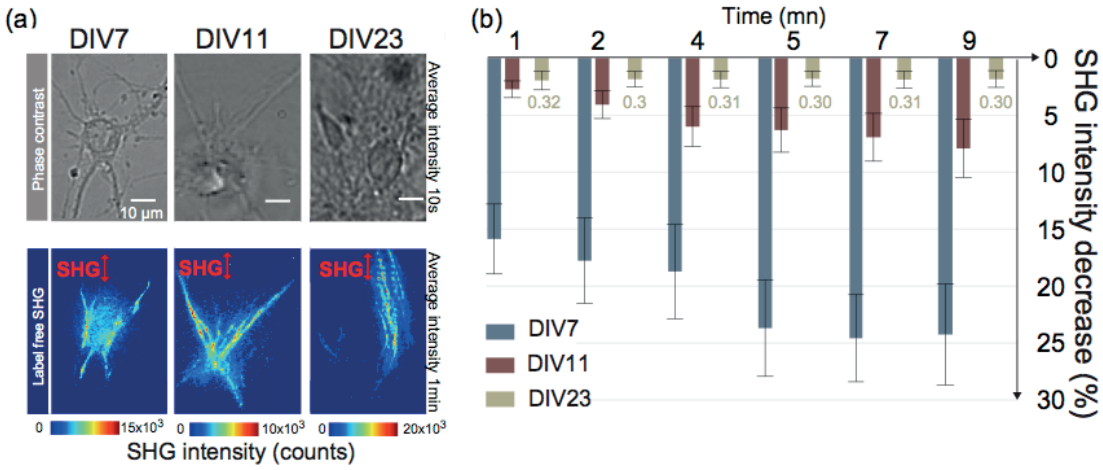

Figure 3.3: **Nocodazole-induced SH intensity depletion from the cytoskeleton of neurons at different stages of maturity.** (a) Top panels, PC images of cultured neurons at different stage of maturity. Bottom panels: respective label-free SH images averaged over 10 s during the control conditions. (b) Histograms of SH intensity decrease (in %) as a function of the time of exposure to a 10 µg/ml solution of nocodazole.

3.3.4 *In vitro* SH imaging of multisite time-resolved microtubule morphology changes

In another application, we demonstrate the possibility of dynamic SH imaging to obtain spatiotemporal stability information about the axonal microtubule network. We image the microtubule network of a single axon of a newly polarized neuron (DIV7, the cell depicted in Figure 3.2a) treated with nocodazole and after wash out. We examine the SH intensity variations in the 0.25 s acquisition time SH images, that occur at three different regions along the axon of the neuron in Figure 3.2a. and represented in the schematic of Figure 3.4a: the proximal region closest to the cell body (ROI 1), a middle shaft part (ROI 2, >50 µm from the cell body) and a distal shaft part (ROI 3, > 100 µm from the cell body). Figure 3.4b shows the decay of the averaged SH intensity as a function of time during nocodazole application for the three ROIs. Single exponential decays are used to fit the data. These fits show that during nocodazole exposure, an exponential depletion in the SH intensity is observed as a function of time, with different decay times for three ROIs along the axon: the averaged SH intensity from the proximal region decreases with a halftime of 2 min 30 s ± 35 s ($R^2 = 0.93$), whereas the halftimes of the middle and distal axonal shafts are slower, 2 min 48 s ± 25 s ($R^2 = 0.98$) and 3 min 47 s ± 76 s ($R^2 = 0.95$) respectively. We observe that the halftimes values of the SH intensity depletion during nocodazole treatment increase with respect to the distance from the cell body. These observations are in agreements with literature[237] although the optical contrast mechanism is dissimilar, the similarity in decay times during nocodazole exposure suggests that both methods report on the decrease in the density of axonal microtubules.

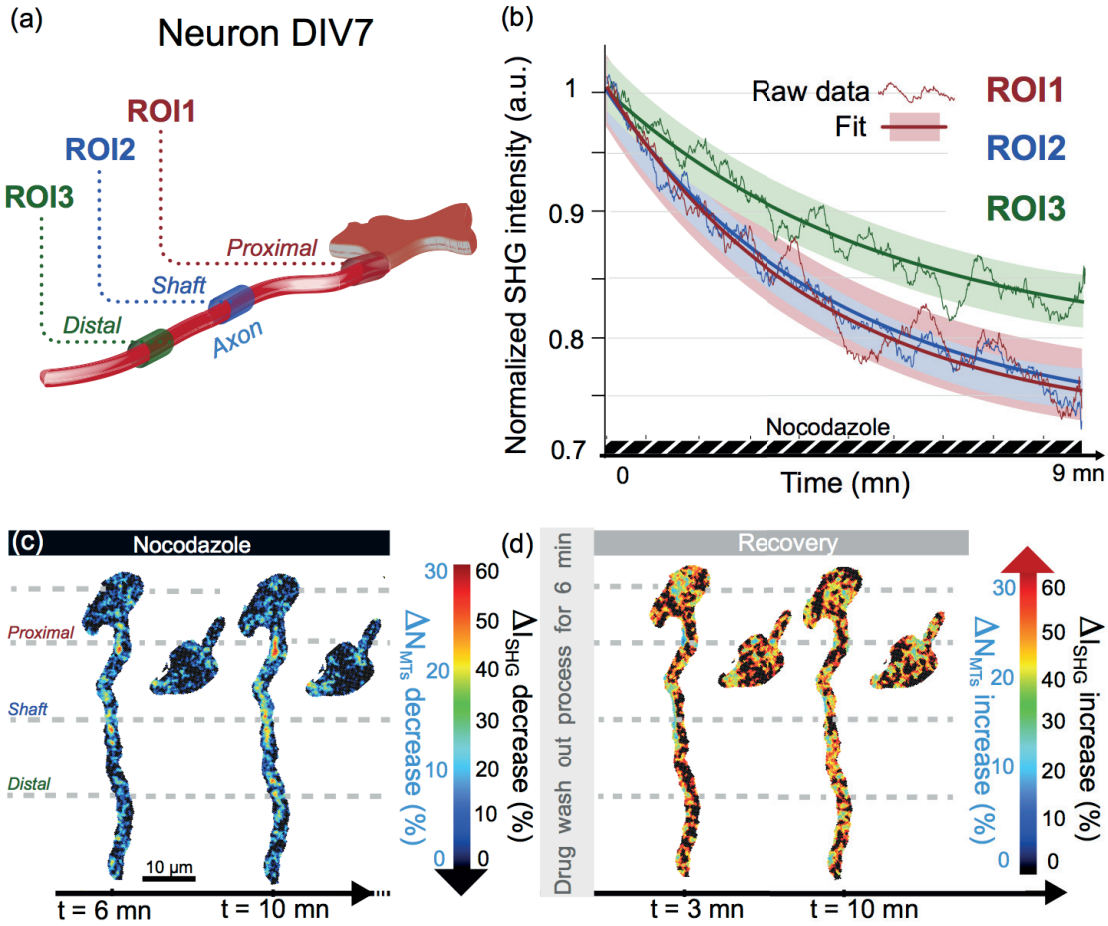

Figure 3.4: Spatiotemporal SH imaging of microtubule stability. (a) Schematic view of an axon with three different regions of interest. (b) Normalized nocodazole-induced SH intensity depletion for the three different regions of interest indicated in (a). The colored intensity traces represent the filtered raw data, obtained with a 7th order median filter, the smoothed darker color traces represent intensity traces that were filtered with a 100th-order median filter and a low pass moving-average filter with a span of 5. (c) Spatiotemporal maps of percentage of decrease in SH (ΔI_{SHG}) and microtubules density (ΔN_{MTs}). The control signal is taken at t = 0 min when the drug is injected into the bath (average of 10 frames with 0.3 s/frame). Then the decrease in the SH intensity and microtubules density is mapped as a function of time during the 10 minutes of the nocodazole treatment (10 µg/mL) and after 20 minutes of recovery following the wash out. The gray dashed lines correspond to different morphological areas along the axon: proximal, shaft (middle shaft of the axon) and distal (distal axonal shaft). In the proximal region of the axon, we observed a gradual loss of SHG spreading towards the distal part of the axon. During the recovery, the middle axonal shaft shows a spread damaged area of SH loss recovering towards the proximal part in discrete local points.

In addition to analyzing the decay of the SH intensity in three distinct regions of interest, we make a pixel-wise comparison and map the reduction and the recovery of SH intensity per pixel as a function of time for the whole neurons (Figure 3.4c-d) and look at the SH intensity variations in the axon. The directional polarity of microtubules in the axon is uniform[9], ($P_{MT} = 1$), as it can also be seen in Figure 3.1c with the narrow orientational distribution of neurite 1. This specific uniform polarity,

allows us to relate the SH intensity to the number of uniformly oriented microtubules[51] with, $I_{SHG} \propto (N_{MT} \times P_{MT})^2$. We apply the above-mentioned equations with the assumption that nocodazole does not alter the orientational distribution of the microtubules and relate the relative SH intensity decrease to the relative change in the microtubules number during nocodazole application (see Appendix 3.1):

$$\frac{N_{MT}(t)}{N_{MT,0}} = \sqrt{\frac{I_{SH}(t)}{I_{SH,0}}}$$

in which $I_{SH,0}$ denotes the initially measured SH intensity of the axon and $N_{MT,0}$ the corresponding initial number of microtubules at t = 0 before nocodazole application. Since Baas[238] has shown that after nocodazole treatment the microtubule polarity is for 96 % identical to the pretreated neuron, we think this assumption is reasonable. With this approach, it is possible to map on a pixel-size scale the spatio-temporal fluctuations of SH intensity and the variation in the number of microtubules. Figure 3.4c shows a map of the percentage of decrease in SH intensity (black scale, $\Delta I(t) = \frac{(I_{SH,0} - I_{SH}(t)) \times 100}{I_{SH,0}}$) and corresponding relative change in the number of microtubules (blue scale, $\Delta N_{MTs}(t) = \frac{(\sqrt{I_{SH,0}} - \sqrt{I_{SH}(t)}) \times 100}{\sqrt{I_{SH,0}}}$) during nocodazole exposure. Figure 3.4d shows the relative SH intensity increase and converted increase in the relative number of microtubules during recovery. It can be seen that 6 minutes after the nocodazole application, there are isolated sites ~ 1 µm in size that have a 30 % reduction in the number of axonal microtubules. These sites occur more frequently closer to the cell body. In the proximal part there is also a 3 µm-size core with a similar decrease in the relative number of microtubule. After 9 minutes these discrete sites of damage connect together and expand towards the distal part of the axonal shaft. During the recovery the damaged cores are restored, whereby the distal part appears to heal the quickest.

The above data demonstrates the possibility of imaging spatiotemporal changes *in vitro* during and after the application of the microtubule destabilizing drug nocodazole. Since the presented data set is limited (N=7) it is impossible to draw conclusions about the mechanistic effects that nocodazole has. Future more extensive studies could map the degradation more clearly as well as conduct intermediate real-time polarimetric measurements to determine if and how and where the microtubule network undergoes structural changes. A combination with SH interferometry[61] could add information on microtubule directionality during nocodazole exposure and after washout.

3.3.5 Conclusions

Wide field high throughput SH microscopy was applied to study living mammalian neurons with the aim of demonstrating the possibility to extract the orientational distribution of microtubules as well as obtaining dynamic label-free spatiotemporal stability information *in vitro*. We used nocodazole, a microtubule destabilizing drug as it is a well-known reversible microtubule-specific depolymerizing drug. We performed SH polarimetry measurements to demonstrate how the pixel-wise orientational directionality of microtubules in neurites and cell bodies can be determined. When the microtubules are oriented along the principle axis of the neurite with a narrow orientational distribution (rather than having a broad orientational distribution that is not aligned with the principle axis of the neurite) and the locally emitted SH intensity is significantly higher than in other parts we can assign a structure as the axon. We also showed the possibility of extracting information of the stability of cytoskeleton relative to nocodazole exposure as a function of the neurons' age with SH imaging. We then performed spatiotemporal SH imaging during and after the application of nocodazole on a single neuron's axon. Assuming that nocodazole does not affect the orientational distribution of microtubules, direct statements can be made to relate the variations in the SH intensity with the changes in microtubule density. These measurements show the possibility of real-time *in vitro* imaging of changes in the morphology of the axonal microtubules, which could be done for other applications. Future integration of real time SH polarimetry, possibly in combination with other methods (i.e. immunostaining), could significantly increase our quantitative understanding of microtubules cytoskeletal morphological changes. These additional imaging modalities may also be promising tools for investigating neurodegenerative diseases or the spatiotemporal dynamics of mitosis.

3.4 Appendix

3.4.1 Relative variations of nocodazole-induced microtubules loss

The SH intensity depends inherently on the density and spatial organization of SH active dipoles. In neurons, microtubules constitute one of the main SH active dipole (see Chapter 1). Compared to the 515 nm SH wavelength, the 8 nm long and 25 nm diameter rings of tubulin dimer which are the main components constituting the microtubules, are considered as point sources. With this respect, it is possible to estimate the relative variation of axonal microtubules density from the SH intensity upon nocodazole exposure. In axons, microtubules have a directional polarity of 1, they are arranged uniformly with their plus-end distal to the cell body (Figure 3.5a) and are arranged within a packed hexagonal lattice[51,71] (Figure 3.5b). We assume a constant hexagonal repartition of the microtubules and a parallel arrangement with respect to the sample plane (Figure 3.5b), ignoring the out-of-the-plane tilted microtubules that could affect the intensity of the SH signal.

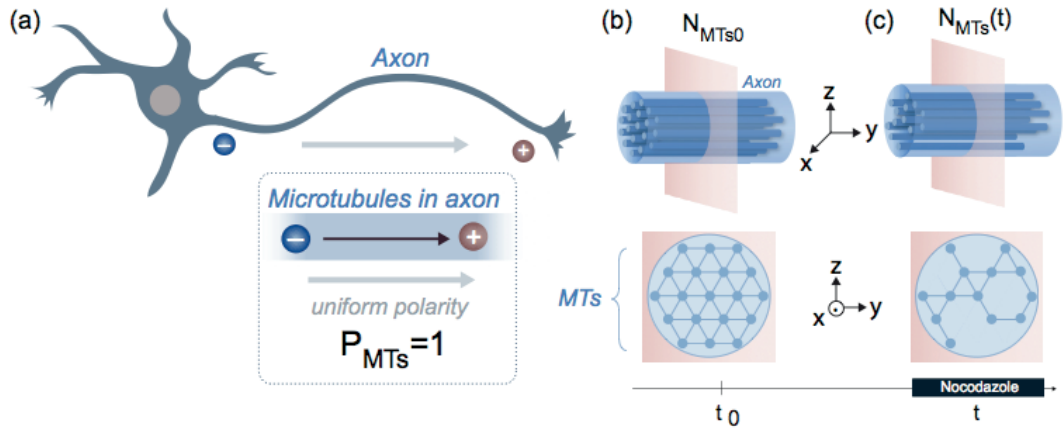

Figure 3.5: **Schematic views of the variation of uniformly oriented axonal microtubules density as a function of time and exposure to nocodazole**. (a) Schematic view of the axon with the expression of the axonal Microtubules orientation. Axons have a uniform orientation of Microtubules with their plus-end distal to the cell body, exhibiting a Polarity (P_{MT}) of 1. (b) Schematic sagittal and coronal views of the microtubules, arranged within a hexagonal packed lattice, and the illustration of the microtubules density loss during nocodazole exposure.

Nocodazole depolymerizes microtubules, this depolymerization can be expressed in term of a loss in the number of microtubules (or density loss) for a given position: At t_0 the number of microtubules for an axonal cross section is intact (N_{MT0}) (Figure 3.5c). During nocodazole exposure, and for the same given position, the cross-section of the axon exhibits less microtubules (Figure 3.5c). The number of the microtubules at t (N_{MT}) is smaller than the initial number (N_{MT0}) at t_0.

In term of SH signal, in our experiments, we denote SHG_0 the initial measured SH intensity of the axon at t = 0 when the nocodazole is injected to the bath. We take the intensity average of 10 frames from t = 0 min as a reference signal and define the variations of the SH intensity as a function of time such as:

$$\frac{SHG_0 - SHG(t)}{SHG_0} \tag{3.5}$$

Considering the microtubules density relation from the equation given in Chapter 3:

$$\frac{SHG_0 - SHG(t)}{SHG_0} = \frac{N_{MT0}^2 - N_{MT}^2(t)}{N_{MT0}^2} \tag{3.6}$$

with N_{MT0} the initial umber of the microtubules at t = 0 and $N_{MT}(t)$ the number of microtubule as a function of time. The variations of the microtubules density become

$$\frac{N_{MT}(t)}{N_{MT0}} = \sqrt{\frac{SHG(t)}{SHG_0}} \tag{3.7}$$

With this expression, it is possible to convert the nocodazole-induced percentage of decrease in SH intensity into a percentage of decrease in the number of microtubules as a function of time (Figure 3.4).

Chapter 4
Probing neuronal morphology and metabolic activity with label-free SH polarimetry and endogenous 2PEF

We investigate the changes in neuronal morphology and metabolic activity by measuring label-free SH polarimetry and endogenous 2PEF using high throughput and low photodamage wide field multiphoton imaging. We calculate the coefficient of polarization (COP), which reports on orientational irregularities in the microtubule cytoskeleton and used endogenous 2PEF as a metabolic marker in cultured neurons throughout the stages of their morphological development.
In the early stages, the SH intensities and COP report on the peripheral organization of microtubules and highlight the centrosome, visible till the stage 3. At this stage, 2PEF reports on a high metabolic activity at interstitial branching points on the outgrowing axon, colocalizing with places where a structural depolarization, as mapped by the COP, is visible. As neurons mature, 2PEF is observed only in soma and neurites exhibit fainter SH responses indicating that structural degradations have taken place. The comparison of the 2PEF and the SH intensities averaged over the cell body as a function of neuron age displays three distinct zones: before, during and after the differentiation.
Being able to observe in a label-free manner morphological changes in the cytoskeleton of living neurons, with clear markers of organization in combination with indicators for metabolic activity, allows to follow neuronal differentiation in detail and may serve as a label-free indicator to determine the relative age of neurons.

4.1 Introduction

4.1.1 The different stages of the morphological neuronal development

The sequential biological mechanisms underlying the morphological neuronal development is shared by most classes of nerve cells *in vitro* and *in vivo*[2]. Neuronal morphogenesis in culture is achieved through a sequence of five well-defined developmental stages that requires precise regulatory structural and metabolic mechanisms[239]: the lamellipodia, minor processes, axonal outgrowth, dendritic outgrowth and the maturation. These stages start from the first hour following the postplating and post-mitotic neuronal process as discussed in Chapter 1.

From a structural point of view, the cytoskeleton is largely responsible for modifying the neuronal shapes during the specific phases of embryogenesis[240] and later during cellular migration. Of particular interest is the reorganization of the cytoskeleton from the centrosome from the early stage 1 until the axonal and dendritic outgrowth during the maturation process.

Figure 4.1 shows cultured neurons taken at different stages of their neuronal development and imaged with different modalities (PC, SH, 2PEF, and the corresponding calculated coefficient of polarization, explained hereafter). Stage 1 of the morphological neuronal development starts with the breakage of the cell body by the growth of thin, sheet-like membrane protrusions, the lamellipodia. This neuritogenesis is accomplished upon specific cytoarchitectural mechanisms comprising a dynamic peripheral and bundling of actin and microtubule arrays[240].

Later, the axonal outgrowth, a process in which the neurons use a combination of guidance cues to assemble a functional neural network is a crucial stage for developing neurons. During this stage, the axons undergo major structural changes with the sprouting of collateral axonal branching, also referred to as interstitial branching[241]. These localized expansions of the plasma membrane in the shape of axon collateral branches aim at establishing extensive synaptic connections with target cells. They also play a crucial role in the endogenous neuroplasticity following an injury[242] or disease[243]. Studying the mechanisms involved in the formation of the collateral axonal protrusions is integral to our understanding of both normal and pathological neurodevelopment. It has been reported that the formation of collateral axonal branches relies mainly on cytoskeleton rearrangements[244]: branch formation is closely accompanied with formation of short, highly dynamic microtubule fragments that invade the sprouting branches resulting in a cytoskeleton reorganization along the axon shaft[3]. Previous studies[245,246] demonstrated evidences of a cross functional activity into the formation of collateral axonal branching between the two main cytoskeletal components: actin filaments and microtubules. However, due to the lack of technical specificity and the close entanglement of actin and microtubules in the cytoskeleton, little is actually known about the specific nature of the

underlying cytoskeleton mechanisms leading to the formation of axonal branching. On the metabolic side, calcium ions have been detected as active actors contributing to the promotion of a multitude of cellular signaling pathways that can affect the activity of cytoskeleton proteins and regulators involved into the promotion of axon branching[247]: localized increases in calcium ion levels have been observed at the origin of nascent branch points[248]. Furthermore, additional fluorescent studies stressed the coordination of the cytoskeleton reorganization and stalled mitochondria metabolic activity in determining sites of branching along the axon[249–251]. These metabolic and structural changes are relevant in the morphogenetic processes of neuronal differentiation. In the quest of understanding the fundamental cellular mechanisms at the origin of the branching formation[252], specific imaging approaches are needed to unravel the structural and metabolic mechanisms at the origin of the promotion and maturation of collateral axonal branching. Once the axonal outgrowth and branching processes terminate, the remaining neurites continue their growth and arborize into a dense morphologically-distinct functional network. The cytoarchitecture of the cytoskeleton becomes more elaborate and complex, requiring specific metabolic and dynamic changes to establish a dense network of active synaptic connections.

Nonlinear imaging, including two photon emission fluorescence (2PEF) and second harmonic generation (SHG) has proven invaluable in observing physiological functionality in microscopic and subcellular neural compartments[253]. Active 2PEF endogenous fluorophores are often used to image the metabolic activity[254] and SHG provides a good mode of contrast to specifically image the structural organization and architecture of the microtubules in the neuronal cytoskeleton as discussed in Chapter 1 and 3. Label-free SHG signal have been observed from mature axons[71,124] but not from dendrites of mature hippocampal cultured neurons[124]. Only few studies reported on the observations of label-free SHG signal from axons throughout the whole neuronal development cycle and from mature apical dendrites in specific sites in acute brain slices of adult mice[124]. Taking into account that SHG is sensitive to the intrinsic organizational polarity of the underlying microtubules, it explains why SHG signal has been mainly observed in mature axons, where the polarity is uniform. On the other hand, in dendrites, where the polarity changes with the maturity, no SHG signal has been observed in dendrites with a mixed microtubule orientational polarity more than 65%[71]. Up to date, there is no mention of label-free SHG signal from juvenile dendrites nor cell bodies throughout all the different stages of maturity of cultured neurons. This lack of observations comes from the deficiency in the imaging throughput of the existing SH techniques. This is probably the reason why no detectable SHG was observed from dendrites presenting a mixed polarity orientation superior to 65% and was observed only from axons.

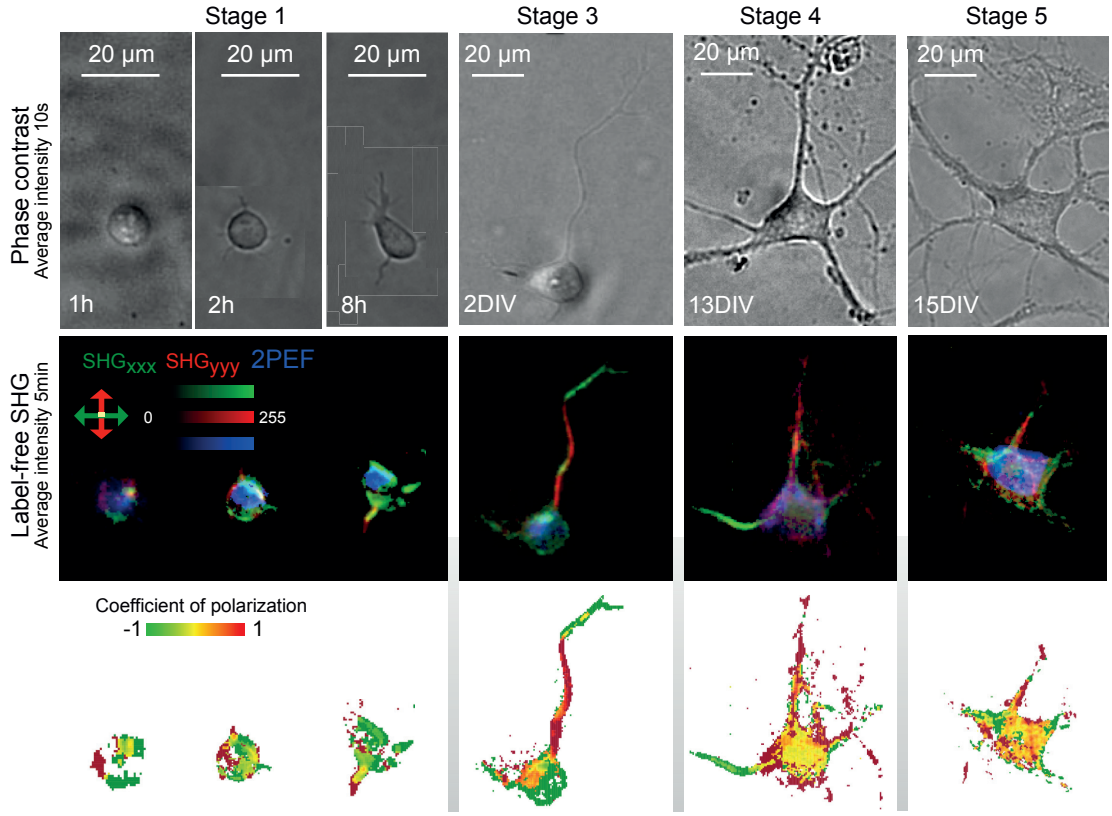

Figure 4.1: Stages of development of primary cortical neurons in culture imaged with different modalities. Phase contrast (PC), second harmonic (SH), two photon excitation fluorescence (2PEF) and the corresponding coefficient of polarization (COP). (a) PC images of primary cultured neurons illustrating each steps of the neuronal development. The age of the neurons is shown in the bottom left corner of each image. Each neuron is taken from a different cell culture. (b) Composite image of the neurons from (a) with SH_{xxx} in green, SH_{yyy} in red and endogenous 2PEF in blue. The stages of neuronal development are written on the top left corner. 2PEF signal is recurrently observed from the cell body throughout every stage. (c) Maps of the COP. Values equal to 1 and -1 expresses uniform organization of the underlying SH active structures along the vertical (y) or horizontal (x) axis respectively. COP values close to 0 express a non-uniform organization of the underlying SH active structures.

4.1.2 Imaging the different stages of the morphological neuronal development

In this Chapter, we performed label-free SH polarimetry and 2PEF measurements on cultured neurons at different stage of development using high throughput wide field multiphoton imaging. With the enhanced throughput of several orders of magnitude combined with the low photodamage[201,212] we use the unique inherent structural sensitivity of SHG to microtubule organization and 2PEF to metabolic activity in cultured neurons at different stages of their morphological development to characterize the structural and metabolic morphogenesis of cultured neurons: we performed white light phase contrast, endogenous 2PEF, and polarization resolved-SH imaging (Figure 4.1). From

the polarization-dependent SH images, we calculate the coefficient of polarization (COP), which is used to quantify the depolarization, which reports on orientational irregularities in the cytoskeletal microtubules and defined such as:

$$COP = {SH_{xxx} - SH_{yyy}}/{SH_{xxx} + SH_{yyy}} \quad (4.1)$$

For neurons of stages 1 and 2 we observe 2PEF from the cell body. This 2PEF is localized to a single 1-micron sized spot, which is placed close to the centriole. SH is emitted from the periphery that extends into proto-processes. In stage 3 we observe 2PEF also from axons and dendrites. This 2PEF co-localizes with places where there is a structural depolarization visible, pointing towards the possibility of label-free detecting axonal branching. For stage 4 and 5 neurons 2PEF emerges uniformly from the soma, but not anymore from the neurites. The SH signal no longer emerges from the periphery only but uniformly from the cell body, and it is very strong from the neuritis, indicating that the neurons have matured. Advanced developed neurites have a much fainter SH response, indicating that structural degradations have taken place. Figure 4.1 shows independent cultured neurons taken at different stages of their maturity and imaged with PC, 2PEF, SHG and their corresponding COP. We also establish a comparison between the ratio of 2PEF and the SHG intensity averaged over the cell body as a function of the neurons' age. This ratio may serve as a label-free indicator to determine the relative stage of maturity of a neuron. In what follows we will examine the different stages of the neuronal development in detail.

4.2 Results and Discussion

4.2.1 Stage 1 and 2

In neuronal cultures, shortly after the attachment of the neurons to the extracellular matrix, stage 1 of the morphological neuronal development starts with the breakage of the spherical membrane symmetry by the growth of nascent projections, the lamellipodia[255]. Figure 4.2a-c show PC, SH (SH_{xxx} and SH_{yyy}) and 2PEF images from neurons 1h to 8h after plating.

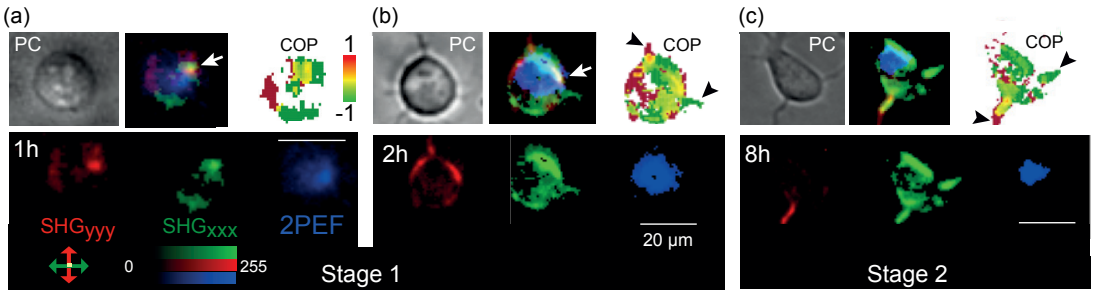

Figure 4.2: Details of stage 1 and 2 of the neuronal development before the morphological differentiation. (a) Primary cultured neurons at stage 1 imaged 1h after their platting, left panel PC image, middle panel composite image obtained with SH_{xxx} in green, SH_{yyy} in red and endogenous 2PEF in blue and right panel COP map. The individual split channels are depicted on the bottom row. (b) Same imaging modalities for primary cultured neurons from a different cultured taken at stage 1 and 2h after platting and (c) taken at stage 2, 8h after platting.

A faint SH emission is detected from the periphery of the cell bodies at stage 1 (Figure 4.2a-b), while stage 2 neurons display a stronger SH emission from the periphery of the cell body and in the nascent protoprocesses (Figure 4.2c). Neurons at stage 1 display a brighter ~1-µm dot observed with both SH_{xxx} and SH_{yyy} polarization combinations at the periphery of the cell body (Figure 4.2a,b indicated by the arrows). Such feature is not visible after stage 1. This bright dot likely coincides with the centrosome, from which microtubules are formed and which silences after stage 2[256].

Regarding the COP map, in Figure 4.2a-b (right panels), we observe signal coming mainly from the periphery of the cell bodies, with values close to -1 or 1. This indicates a uniform directionality of the underlying SH-active structures, the microtubules. Intermediate COP values are observed at the 1-µm size spot that we identify as the centrosome: this indicates that an equal number of X and Y oriented microtubules are found in this spot. The distal parts of nascent protoprocesses from neurons at the end of stage 1 and in stage 2 display extreme values of COP (either -1 or 1), indicating a uniform directionality arrangement of microtubules. On the other hand, the proximal part of the protoprocesses in stage 1 and 2 express COP values around 0 (Figure 4.2b-c black arrow heads) indicating a higher degree of disorganization, indicative of areas with non-uniformly oriented microtubules. In these stage 1 and 2 neurons, we observe a non-homogenous 2PEF signal from the center of the cell body, not colocalizing with SH intensities. The 2PEF signal is a signature of the metabolic activity[43]: general actors of the metabolic activity such as mitochondria, Golgi apparatus and endosomes are known to cluster together closer to the side where the first neurite will from in the cell body[257]. Thus, the non-uniform 2PEF distribution reflects the presence of metabolic organelles near the centrosome.

4.2.2 Stage 3, axonal branching

In stage 3 of the neuronal development, one of the minor processes of the neurons exhibits a higher growth dynamic and elongates at a rapid rate up to several micrometers to become the axon[258]. Compared to the shape of the other minor neurites, the shape of this young axon is rather slender[259]. Figure 4.3a-e shows PC, SH (SH_{xxx} and SH_{yyy}) and 2PEF images from 2 different neurons in stage 3 (2 DIV) of their morphological development.

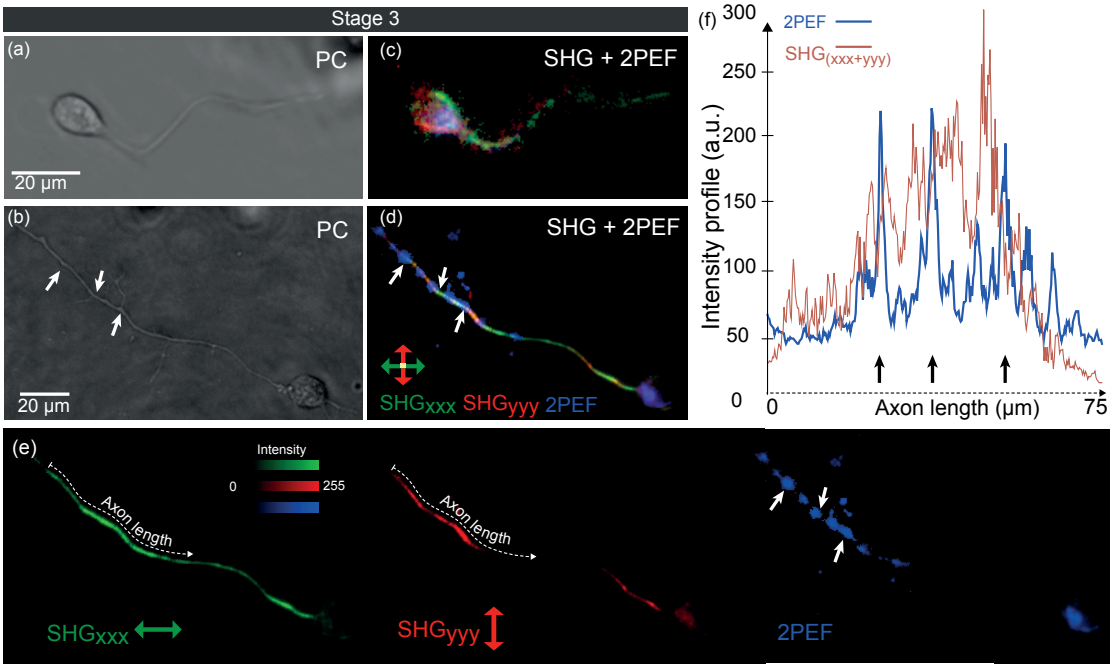

Figure 4.3: Cultured neuron at stage 3 imaged with PC, SHG, and 2PEF. (a) PC image of a neuron during its axonal outgrowth. The newly emerged axon is smooth, with no other protoprocesses. (b) Composite image of the same neuron with 2PEF in blue, SH in x direction (excited and analyzed, in green), in y direction (excited and analyzed, in red). (c) PC image with a neuron during its axonal outgrowth stage, arrows point towards visible branches. (d) Composite image with SH in x direction (excited and analyzed, in green, (e) left panel), in y direction (excited and analyzed, in red, (e) middle panel) and 2PEF in blue (e, right panel). (f) Intensity profile along the axon length from the most distal part of the axon to the axonal shaft for 2PEF and SHG intensity (both polarization added together).

In both PC images (Figure 4.3a-b), the young axon is recognizable with its long and thin shape arising from the cell body. Figure 4.3a displays a neuron with only one smooth and thin process emerging from the cell body whereas in Figure 4.3b (white arrows), we observe morphological protrusions along the axon. These protrusions are examples of one of the major morphological changes that the axons undergo during the outgrowth at stage 3. During this stage, axons develop many collateral protrusions which play a crucial role in the formation of a neural network[241]: the axonal collateral

branches. Figures 4.3c-d show composite images with SH (xxx in green and yyy in red) and 2PEF. When the axon is oriented 45 degrees away from the horizontal (x) direction, both polarization combinations emit a comparable SH intensity. The resulting overlap of the SH intensity acquired with these two polarizations is displayed in yellow in Figure 4.3c-d. Details of the different image modalities of the neuron in Figure 4.3b are shown as split channels in Figure 4.3e. In Figure 4.3e, right and middle panels, we distinguish slight intensity variations along the axonal length that can be associated either with a non-parallel orientation of the underlying SH-active axonal microtubules or are coming from variations in the axonal microtubules density. In Figure 4.3e, right panel, we observe a strong endogenous 2PEF signal coming from the cell body and distinct patches along the distal part of the axon. Some of these distinct patches are localized at the origin of the nascent and developed branches visible in the PC image (Figure 4.3b, white arrows), while others do not correspond to any visible protrusions. To make a connection between the 2PEF and SHG intensity variations, we plot the SH (x+y, red) and 2PEF intensity (blue) profiles along the axonal length in Figure 4.3f. The black arrows indicate the points where some branching is visible in the PC image: they colocalize with the 2PEF intensity peaks. These peaks are likely associated with the metabolic activity of stalled mitochondria found at branching point along the axon[260]. Comparing with the SHG intensity profile, no obvious SHG intensity fluctuations can be correlated with each 2PEF maximum. To investigate further the structural reorganizations from the SH polarization dependent images, we compute the COP. The COP is independent of the intensity fluctuation and dependent solely on the orientational distribution of the microtubules. Thus, heterogeneities in the COP along the axon indicate heterogeneities in the relative orientational distributions of microtubules. The resulting COP map is shown in Figure 4.4a.

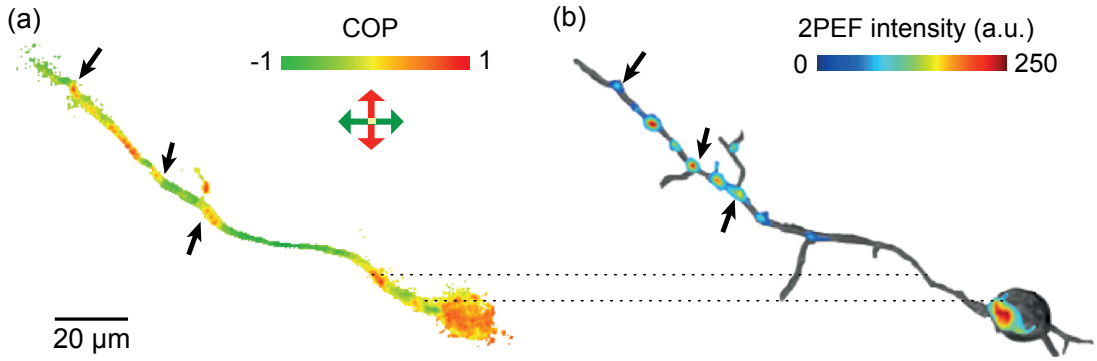

Figure 4.4: Coefficient of polarization from a neuron at stage 3 of its neuronal development. (a) COP: a value close to 1 and -1 expresses an ordered structural organization whereas intermediate value highlights a highly disordered structural organization of SH-active dipoles, the microtubules. Arrows pinpoint the emplacement of developed collateral branches visible in PC. (b) Composite image with endogenous 2PEF and PC signal of the same neuron. The existing collateral branches are marked with black arrows.

Arrows in Figure 4.4a pinpoint the localization of collateral branches visible in PC. We observe distinct heterogeneities in the COP, ranging from 0.3 to 0.6 µm in size, which colocalize with sites of 2PEF patches. We can interpret these observations in terms of a possible connection between a cytoskeletal reorganization and a metabolic activity, which is required for the branching process. Previous studies demonstrated the evidence of the coordination of metabolic activity from stalled mitochondria and cytoskeleton reorganization in determining sites of branching along the axon[249,250], in this sense, our observations and interpretations are in agreement with literature. Thus, the discontinuities in the COP values along the axon are likely associated to structural changes in the orientation of the axonal microtubules. In the proximal part of the axon, no 2PEF is detected and no collateral branches are visible (Figure 4.4a-b dotted lines), however apparent discontinuities in the COP values are discernable. A possible interpretation, in reserve of further detailed experiments, could imply that branching is about to take place.

4.2.3 Stage 4

After the morphological differentiation, stage 4 begins: dendrites establish their complex network and axons slowly pursue their growth. The cycle of the morphological development ends on the stage 5 with the maturation of the neurons[15].

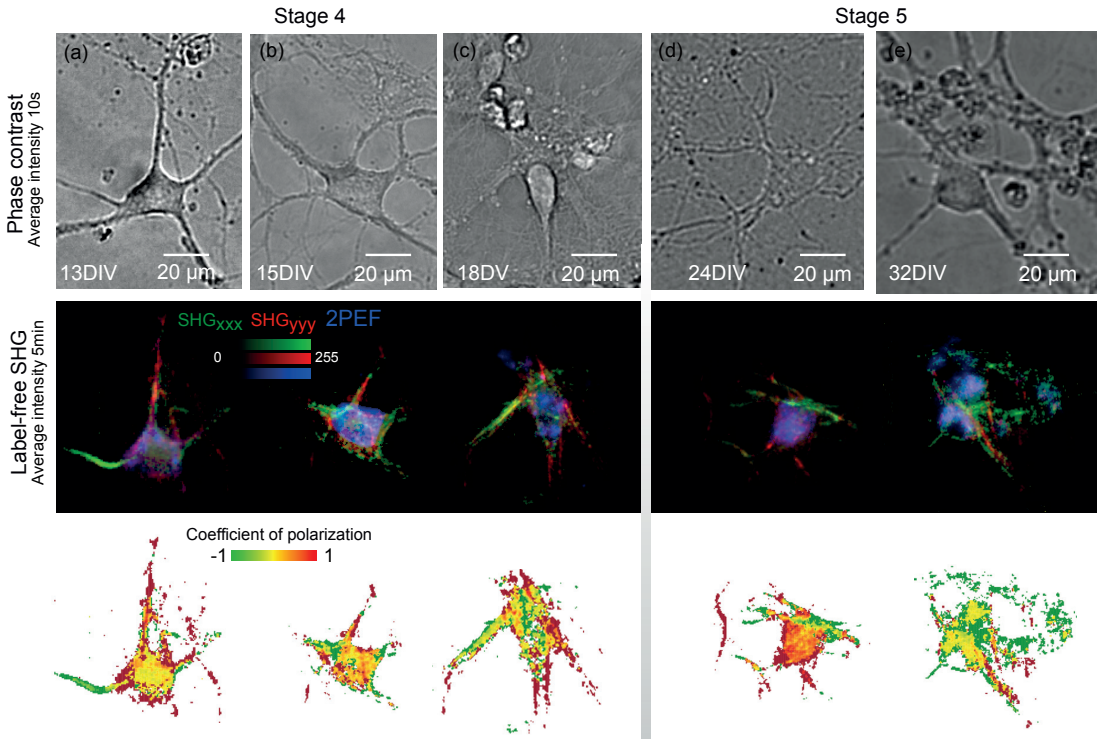

Figure 4.5: Details of stage 5 of the neuronal development during the dendritic outgrowth until the late stage of maturation imaged with PC, SH, 2PEF and the corresponding coefficient of polarization (COP). (Top row) PC images of primary cultured neurons illustrating the stage 5 of the neuronal development. The age of the neurons is shown in the bottom left corner of each image. Each neuron is taken from a different cell culture. (Middle row) Composite image of the neurons from (Top row) with SH_{xxx} in green, SH_{yyy} in red and endogenous 2PEF in blue. The stages of neuronal development are written on the top left corner. 2PEF signal is recurrently observed from the cell body throughout every stage. (Bottom row-) Maps of the COP. Values equal to 1 and -1 expresses uniform organization of the underlying SH active structures, the microtubules, along the vertical (y) or horizontal (x) axis respectively. COP values close to 0 express a non-uniform organization of the underlying microtubules.

Figure 4.5a-e top and middle rows, show PC and respective composite images with SH (SH_{xxx} and SH_{yyy}) and 2PEF intensity from neurons during the stage 4 and 5 of their morphological development, at 13DIV, 15DIV, 18DIV, 24DIV and 32DIV.

At early stage of maturation, Figure 4.5(a-c, middle row) show a strong polarization dependent SH intensity from neurites and a relatively homogeneous 2PEF intensity from the cell body with a brighter intensity shifted either on the side of the axon or the dendrites. 2PEF intensity is observed mostly from the cell bodies, in the form of patches. These bright patches increase in intensity and in size as the neurons mature.

COP values of -1 and 1 are mainly found on neurites, they highlight the uniform orientation of the underlying microtubules array (Figure 4.5a-c, bottom row). Intermediate values of COP are found on the soma, expressing the orientational disorganization of the microtubules in this area.

After 20DIV, (Figure 4.5d-e, middle row) SH intensity is observed all across the neurons, the cell bodies and the neurites, with fainter and dimmer intensity fluctuations along the neurites. At this stage of maturation, the cell body exhibits a faint evenly spread homogenous 2PEF intensity and no more 2PEF is observed after 18DIV on neurites. Figure 4.5d-e, bottom row, shows the COP map, it can be seen that COP values around 0 are still visible in the cell bodies, whereas homogeneous COP values (either – 1 or 1) are observed from the neurites.

4.2.5 Comparison between the metabolic activity and structural changes throughout the whole morphological development cycle with 2PEF and SHG

To assess the change in metabolic activity, compared to structural maturity, we compute the 2EPF/SHG ratio for each neuron taken at each stage of their morphological development and establish a comparison between these two modes of contrast. We calculate the 2PEF/SHG ratio such as:

(4.2)

$$ratio = \frac{2PEF}{\left(SH_{xxx} + SH_{yyy}\right)}$$

Since the only neuronal structure exhibiting both of the contrasts and remnant throughout each of the development stage is the cell body, we focus our analysis on this particular neuronal anatomy. We extracted the mean value of the 2PEF/SHG ratio from the cell body for each neuron at different stages of differentiation and plotted the results as a function of days *in vitro* (Figure 4.6). We further our comparative analysis by plotting on the same graph the width of the COP gaussian distribution as a function of DIV from the same region of interest. This quantity is associated with the angular distribution of microtubules from the cytoskeleton in the cell body. A large width represents a broad orientational arrangement of the microtubules network and a narrow width expresses a uniform orientational arrangement.

From figure 4.6, we distinguish three zones corresponding to the period before, during and after the morphological differentiation. It can be seen that, from the COP values, the orientational distribution of microtubules at stage 1 is narrow (0.13 for 12h old neurons), expressing a small diversification in the orientation of the microtubules. At this stage, before the differentiation the cytoskeleton is organizing itself from the centrosome in a distinct peripherical manner[261], explaining the narrow distribution of the COP. At stage 2, from 0.5DIV to 1DIV, the COP width is the highest (0.8): the cytoskeleton starts to program the emergence of the protoprocesses and future axon, resulting in a broader COP distribution expressing a high distribution in microtubules orientation[262]. From 1DIV to 7DIV, neurons pass through different stages of cytoskeletal reorganization and outgrowth. We observe a chaotic decrease from 0.7 to 0.05 reflecting a reordering of the cytoskeleton: the width of the COP distribution becomes narrow as the neurons mature[263]. After stage 5 and during maturation, the width of the COP distribution reaches low value ranging from 0.05 to 0.02. This expresses either a decrease in the SH intensity, due to cytoskeleton damages from the aging or a highly disordered and complex structure of the mature cytoskeleton. The same trend is observed in the plot of the 2PEF/SHG ratio. As mitochondrial morphology and activity are known to vary as a function of the differentiation stage[43] it is most likely that there is a close relationship between the actors of the metabolic activity in the cell body expressed by endogenous 2PEF fluorophores and a structural regulation of the cytoskeleton dynamics as a function of neuronal developmental stages.

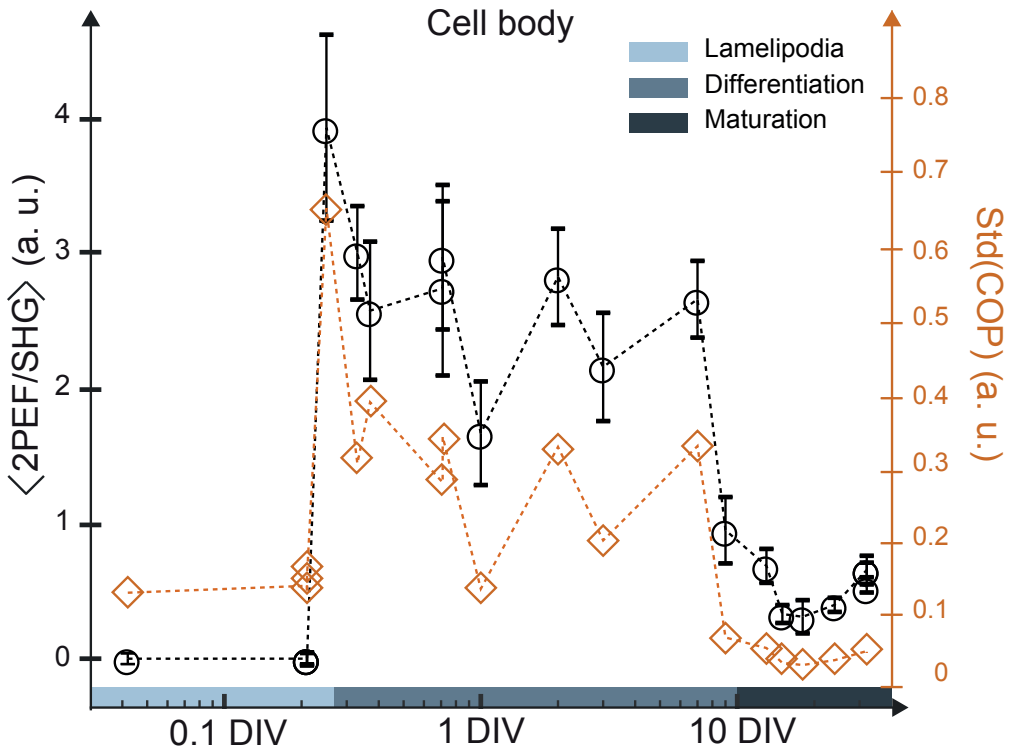

Figure 4.6: Quantitative comparison of the mean value of the 2PEF/SHG ratio and the standard deviation of the COP, from the cell body as a function of DIV (for each case, N = 7). Both quantities reflect the same trend divided in three distinct zones. From 0 to 0.2DIV: the lamellipodia stage, before the differentiation, both 2PEF/SHG and COP quantities are low. From 0.2DIV to 9DIV: during the differentiation process with a chaotic and overall decreasing trend of 50% of the initial values and from 9 to 32DIV: during maturation, low values for both quantities.

4.3 Conclusions

In this chapter, we utilized the unique inherent structural sensitivity of SHG combined with the low photodamage and high throughput of the 3D wide field multiphoton imaging system discussed in the preceding chapter to investigate microtubule organization (polarimetric SHG) and metabolic activity (2PEF) in cultured neurons at different stage of their morphological development. We have been able to observe changes in the metabolic activity as well as changes in the microtubule organization in the various parts of the cells (soma, axons, dendrites, centrosome). In the early stages 1 and 2 preceding morphological differentiation the SH intensity distribution changes from peripherally oriented from the cell body to more directed outgrowth. The centrosome is visible as a region where orthogonal polarization directions are emitted and is placed just above a location with high 2PEF activity. During outgrowth there is a metabolic activity along the axon and where branches are formed[2]. This is apparent from the SH response that shows highly oriented microtubules along the growing axon, and

the 2PEF that arises from localized spots along the axon and dendrites. This 2PEF co-localizes with places where there is a structural depolarization visible (as mapped by the COP). This suggests that label-free detecting of axonal branching is possible by mapping both the COP and the endogenous 2PEF. When the neurons develop further the signature of the 2PEF and SH slightly changes: 2PEF emerges uniformly from the soma, but not anymore from the neurites. The SH signal no longer emerges from the periphery only but uniformly from the cell body, and it is very strong from the neuritis, indicating that the neurons have matured with thicker microtubule bundles in the neurites. Older, more advanced developed neurites have a much fainter SH response, indicating that polarity is lost. A comparison of the 2PEF and the SHG intensities averaged over the cell body as a function of neuron age shows a high intensity plateau during differentiation. This ratio may serve as a label-free indicator to determine the relative age of a neuron.

Being able to observe in a label-free manner morphological changes in the cytoskeleton of living neurons, with clear markers of organization in combination with indicators for metabolic activity, allows to follow neuronal differentiation in detail without modifying the cells. This enables the possibility for long term screening to determine the effects of drugs or diseases that alter the functioning of the nervous systems. Examples are the implication of the structural integrity of the cytoskeleton or the local metabolic activity in neurodegenerative disorders[276, 277]. The introduced techniques could also be combined with targeted fluorescence studies or optogenetics to follow in more detail the intricate complexities of the nervous system[278].

Chapter 5
Membrane water as a probe for neuronal membrane potentials and ionic flux at the single cell level

Neurons communicate through electrochemical signaling within a complex network. These signals are composed of spatiotemporal changes in membrane potentials that are traditionally measured by electrical recordings or using optical probes. Since probes are inevitable invasive and severely damaging to the cells, label-free mechanisms are sought for. For many years second harmonic (SH) imaging has been a promise for delivering direct label-free neuronal membrane potential information. However, to date, this promise has not been delivered, owing to the intrinsic low sensitivity of the SH methods. In this Chapter, we demonstrate a direct application with the 3D wide-field high throughput SH microscope to obtain label-free neuronal membrane potential information. We use changes in the interactions between water dipoles and membrane charges to create membrane potential and ion flux maps of living neurons in real time. To demonstrate the concept, we performed a patch-clamp and SH imaging comparison and show that the whole neuron membrane potential changes correlate linearly with the square root of the SH intensity, as predicted by theory. We then use the nonlinear optical response of the membrane bound water to image spatiotemporal changes in the membrane potential as well as K^+ ion flux during a continuous depolarization induced by an increased in the external K^+ concentration. We observe spatial inhomogeneities that are attributable to a non-uniform spatial distribution and temporal activity of ion channels.

5.1 Introduction

Neuronal signaling occurs through rapid changes in the membrane potential that originate from a redistribution of ionic charges across the plasma membrane, Na^+, Cl^- and K^+ for the most important ions in neurons, associated with the specific permeability of the membrane (see Chapter 1 for more details). An imbalance in the ionic strength between two aqueous solutions that are separated by an impermeable membrane results in a difference in the electrochemical or membrane potential of the two compartments, as described by the Nernst equation[199]. This membrane potential is regulated by ion channels[75,264]. By varying the extracellular concentration of K^+ ions around the giant axons of a squid, while electrically recording the change in resting membrane potential Hodgkin, Huxley and Katz demonstrated the essence of the membrane resting potential regulating mechanism. Ion channels present in the membrane that are either triggered by ligands, neurotransmitters or electrostatic fields regulate the imbalance in ionic strength and thus change the membrane potential[265]. This behavior is modeled by the Goldman Hodgkin and Katz (GHK) equation that relates the membrane potential ($\Delta\Phi$) to the concentration of ionic species (K^+, Na^+, Cl^-) and the permeability (P) of ion channels:

$$\Delta\Phi = \frac{kT}{e} ln \frac{P_K[K^+]_{out} + P_{Na}[Na^+]_{out} + P_{cl}[Cl^-]_{in}}{P_K[K^+]_{in} + P_{Na}[Na^+]_{in} + P_{cl}[Cl^-]_{out}} \quad (5.1)$$

For neurons the potential gradient is mainly controlled by K^+ ions and changing it from 3 mM to 50 mM results in a less negative resting membrane potential, called depolarization. Using standard literature values in Eq. (1), $\Delta\Phi$ changes from -75.4 mV ($[K^+]$ = 3 mM) to -33.3 mV ($[K^+]$ = 50 mM).

Here, we use the interfacial response of the oriented water to construct maps of the electric surface potential. To do so, we related the SH intensity of the interface to the interfacial electrostatic field (E_{DC}) and corresponding surface potential (Φ_0) via[266–268]:

$$I(2\omega, x, y, t) \sim I(\omega, x, y, t)^2 \left| \chi_s^{(2)} + \chi^{(3)\prime} f_3 \int E_{DC}(0, x, y, z) dz \right|^2 \cong \left| \chi_s^{(2)} + \chi^{(3)\prime} \Phi_0(x, y) \right|^2, (5.2)$$

where $\chi_s^{(2)}$ is the surface second-order susceptibility and $\chi^{(3)\prime}$ an effective third-order susceptibility of the aqueous phase that primarily depends on oriented water in the electric double layer, and f_3 is an interference term that takes the value 1 for a transmission experiment (see references[266,269] for more details). Given the low photo toxicity of the high throughput microscope[269], it is possible to use

the reorientation of water molecules in the electric double layer of a membrane to map membrane potentials in living neurons optically and label-free.

We demonstrate the possibility of label-free imaging of the electrical neuronal activity of primary cortical neurons in-vitro employing the unique intrinsic potential sensitivity of SHG. We first characterize the SH throughput for neuroimaging, showing that label-free SH images of neurons can be recorded on 600 ms timescales. We then revisit the experiments of Hodgkin, Huxley and Katz [264] by detecting the resting potential of primary cortical neurons during a K^+ induced depolarization process. Using the nonlinear optical response of interfacial water and nonlinear optical theory we convert the SH images into membrane potential and K^+ ion flux maps. While the average temporal response agrees with the theoretically expected membrane potential changes from the GHK equation and the electrophysiological recordings obtained with the same protocol, the images show clear spatiotemporal fluctuations within the neuron. Different parts of the cells (soma or neurites) are active at different times during the depolarization cycle. Thus, within the framework of the GHK description, there is not only a non-uniform distribution and density of permeant ion channels, but also a different temporal activity. Being able to non-invasively probe membrane potentials and ion flux in active neurons opens up new avenues to understand signaling mechanisms on a single neuron scale or within a larger network.

5.2 Materials & Methods

The Michelson contrast, defined as $\frac{(I_{SHG,max}-I_{SHG,min})}{(I_{SHG,max}+I_{SHG,min})}$, and the signal to noise ratio (SNR) from cultured neurons was calculated for each SH image and plotted as a function of acquisition time We compute the Michaelson image contrast. Figure 5.1a shows an illustration of the experiment. The neurons are kept under a constant flow with a buffer solution containing HEPES, maintained at 37 ºC and are checked for mature electric activity and viability prior to each experiment using phase contrast imaging (see Chapter 2 for details). A composite image of cultured neurons is shown in Figure 5.1b, with a phase contrast (PC) illumination, label-free SH imaging mode (green, red, using different polarization directions of the beams indicated with xxx and yyy) and endogenous two photon fluorescence (2PEF). The images were recorded with a fluence of 2.15 mJ/cm^2 and a peak intensity of 12.79 GW/cm^2. Figure 5.1c shows the Michaelson contrast for SH (green curve), and endogenous 2PF (blue curve). SNRs are also given in the graph. It can be seen that images with an SHG SNR of 4 can be recorded with an acquisition time of 100 ms. Comparing this to literature[124] where label-free images were recorded with scanning microscope systems with acquisition times of 120 s fluences of

340 mJ/cm^2, and peak intensities of 1700 GW/cm^2, the improvement in throughput is more than three orders of magnitude.

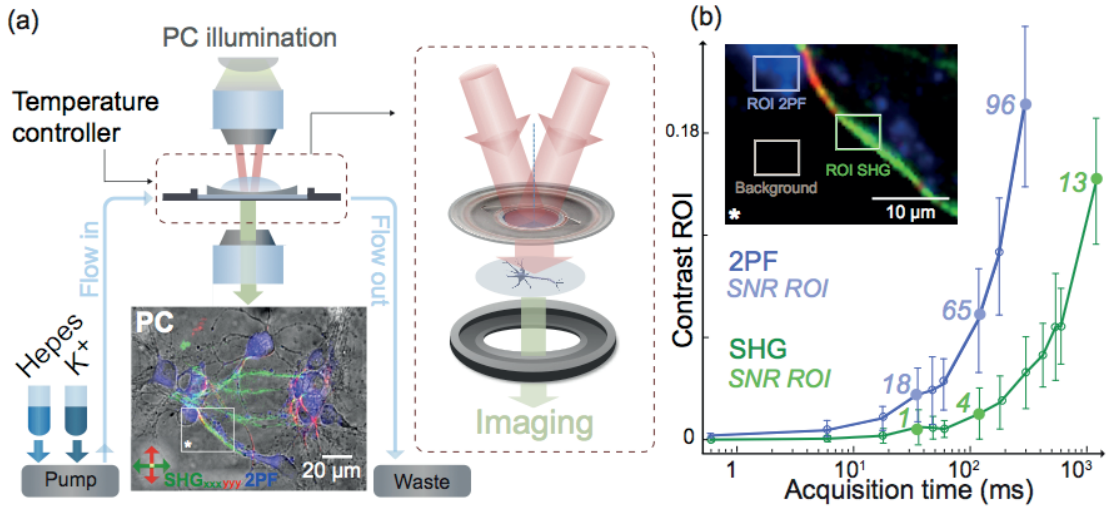

Figure 5.1: Protocol, illumination configuration and second harmonic throughput for neuroimaging. (a) Imaging configuration and protocol with a composite image of 17 days *in vitro* (DIV) cultured neurons. The neurons are provided with a constant flow of solution via a peristaltic perfusion system and SH imaging is done in a wide field double beam transmission geometry. The composite image is composed of a phase contrast (PC), label-free and endogenous two photon fluorescence (2PF). The double head red and green arrows in the image represent the orientation of the respective incoming and analyzed polarization. The white box marked with an asterisk represents the inset in (b). (b) Michaelson contrast with SNR values in italic, calculated from the ROIs in the zoom in the inset, respectively for SHG and 2PF images.

5.2.1 Image processing and data analysis

The raw imaging data were collected from LightField (Princeton Instruments), stored as a TIF stack and exported to Matlab (R2016b) for post-processing. The specific set of data mentioned in this Chapter is composed of a stack of 500 frames with a temporal acquisition of 0.6 s per frame. Noise removing consists of an offset subtraction, a Fast Fourier Transform filter along the temporal dimension, a thresholding and a median filter in the spatial dimension for each frame (kernel = 3).

5.3 Results and Discussion

5.3.1 Comparing electrical and optical recordings

In the following experiments, the cell membrane potential was adjusted by changing the extracellular concentration of K+ ions from 3 mM (normal concentration in the extracellular buffer solution) to 50 mM. A phase contrast (PC) image of a patched neuron (17 days *in vitro*) used for the experiment is shown in Figure 5.2a and its resulting electrophysiological recording in whole-cell current clamp mode is plotted in Figure 5.2b. It can be seen that the resting membrane potential of the neuron (ΔΦ, which corresponds to the difference in surface potentials of the two membrane leaflets) changes from -65 mV to -34 mV. Figure 5.2c is a composite image with PC and SH signals of a single neuron coming from the same culture as the neuron in Figure 5.2a. The normalized square root of the SH intensity recorded under identical conditions and with the same protocol than the electrophysiological recording is plotted in Figure 5.2d. It can be seen that the change in the square rooted SH intensity is very similar to the electrophysiological potential recording. Given Eq. (5.1) and Eq. (5.2), the square root of the SH intensity should scale with the membrane potential. Indeed, plotting $\sqrt{I(2\omega)}$ versus ΔΦ in Figure 5.2e we obtain a linear dependence in agreement with Eq. (5.2). Thus, also in the case of the electrical activity of live neurons, the nonlinear optical response of water can be used as a marker of electrostatic potentials, just like it does at the glass/water[269] and lipid bilayer/water[270] interface.

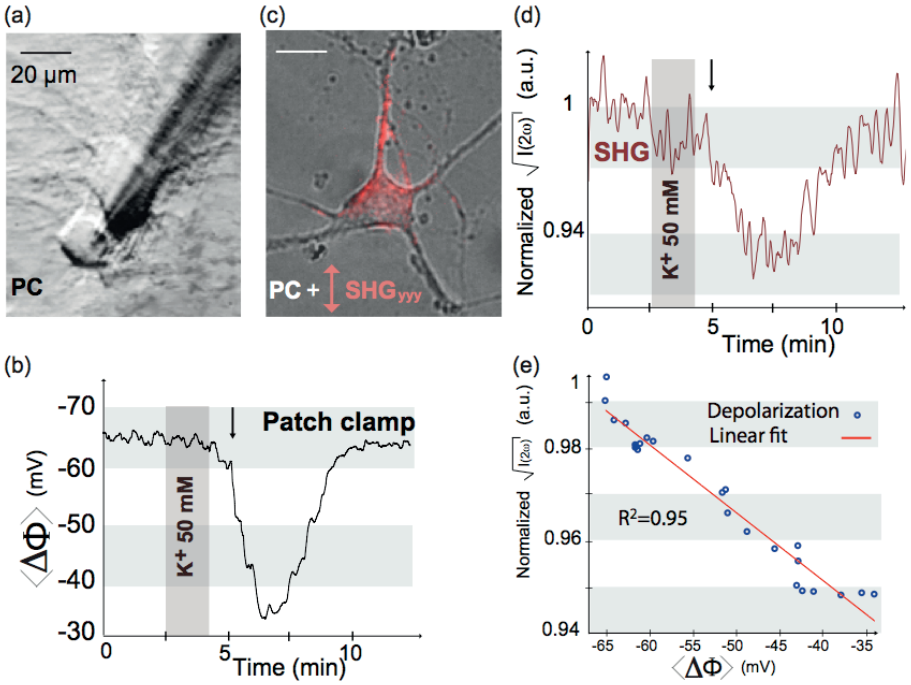

Figure 5.2: Second harmonic and electrophysiological response during a K^+-induced depolarization experiment. Primary cortical neurons in culture undergoing a depolarization induced by increasing the external K^+ concentration, patched (a-b) and probed with SHG (c-d). (b) Whole cell current clamp potential recording, the brown vertical shadow area represents the time lapse application of K^+ solution and the arrow shows when the neurons are undertaking the solution. (c) A composite image with PC and SH signals of a single neuron coming from the same culture as the neuron in (a). The double head arrow indicates the orientation of the polarization (incident and detected). (d) The normalized square rooted spatially averaged SH response from the neuron depicted in (c). The square-rooted spatially averaged SH intensity follows the temporal trend of the patch clamp experiment. (e) Linear correspondence between the changes of the square rooted SHG intensity and the membrane potential from patch-clamp recording with a linear fit.

5.3.2 Membrane potential and ion flux imaging

Having recorded the dependence of electrophysiological membrane potential and SH intensity during K^+-induced depolarization of neurons, we now extract label-free spatiotemporal variations in the membrane potential from the recorded SH images. To do this, we first need to update Eq. (5.2) to reflect better the structural composition of neurons and then apply assumptions that allow us to extract spatio-temporal membrane potential information during the time when the K^+ concentration is changing. As neurons are composed of a cytoskeleton that is constructed by non-centrosymmetric proteins such as microtubules (MT) (refer to Chapter 1) it is necessary to take this into account together with the presence of a lipid membrane (mem) that contains ion channels. Eq. (5.2) then becomes:

$$I(2\omega, x, y) \sim C(x,y) \left| \chi^{(2)}_{MT}(x,y) + \Delta\, \chi^{(2)}_{mem}(x,y) + \chi^{(3)\prime} \Delta\Phi(x,y) \right|^2 \qquad (5.3)$$

where $C(x, y)$ is a constant that converts counts to nonlinear optical response units (m^4/V^2) and includes $I(\omega, x, y)$, the intensity profile of the incoming beams. $\chi^{(2)}_{MT}(x,y)$ is the second-order susceptibility of the microtubules in the cytoskeleton, $\chi^{(2)}_{mem}(x,y)$ the net surface second-order susceptibility of the membrane that is composed of oppositely oriented leaflets $s1$ and $s2$, and $\Delta\Phi(x, y)$ is the membrane potential difference. To determine $\Delta\Phi(x, y)$ from the reorientation of water by the interfacial electrostatic field, we need to find solutions for $\Delta\chi^{(2)}_{mem}(x,y)$, $C(x,y)$, and $\chi^{(2)}_{MT}(x,y)$. Previous SH imaging and scattering experiments on asymmetric free standing lipid membranes[266] and liposome solutions have shown that $\chi^{(3)\prime} = 10.3 \cdot 10^{-22}$ m^2/V^2, and $\Delta\chi^{(2)}_{mem}(x,y) = \Delta\chi^{(2)}_{mem} = 5 \cdot 10^{-24}$ m^2/V. To determine $C(x, y)$, we use the GHK equation and two known values of $\Delta\Phi$, assuming that at steady state the membrane potential distribution across the neuron is constant. At steady state conditions, when the extracellular concentration of K^+ is constant, at $[K^+]_1 = 3$ mM we have $\Delta\Phi_1 = -75.4$ mV and at $[K^+]_2 = 50$ mM we have $\Delta\Phi_2 = -33.3$ mV. Comparing the average intensity over 10

frames (Δt) and subtracting the two resulting time averaged SH intensities to eliminate the contribution of every $\chi^{(2)}$ values, we can determine $C(x, y)$ via:

$$C(x,y) = \frac{\langle\sqrt{I(x,y)(\Delta\Phi_1)}\rangle_{\Delta t1} - \langle\sqrt{I(x,y)(\Delta\Phi_2)}\rangle_{\Delta t2}}{\chi^{(3)\prime}(\Delta\Phi_1 - \Delta\Phi_2)} \qquad (5.4)$$

To estimate compatible (but not unique) $\chi^{(2)}_{MT}(x,y)$ values we use the same assumption and recover $\chi^{(2)}_{MT}(x,y)$, with known values for $\Delta\Phi_1$, $\chi^{(3)\prime}$, and $C(x,y)$. The resulting spatially varying range of values for $\chi^{(2)}_{MT}$ is $-2\cdot10^{-22} < \chi^{(2)}_{MT} < 0.1\cdot10^{-22}$ m^2/V and is in agreement with expectations, as they are an order of magnitude larger than an oriented interfacial monolayer[266].

Finally, the spatio-temporal fluctuations of the calculated membrane potential $\Delta\Phi(x,y,t)$ outside the steady state time windows were determined by substituting the previously calculated $C(x,y)$, $\chi^{(2)}_{MT}(x,y)$ and $\Delta\chi^{(2)}_{mem}$ values into Eq. (5.3).

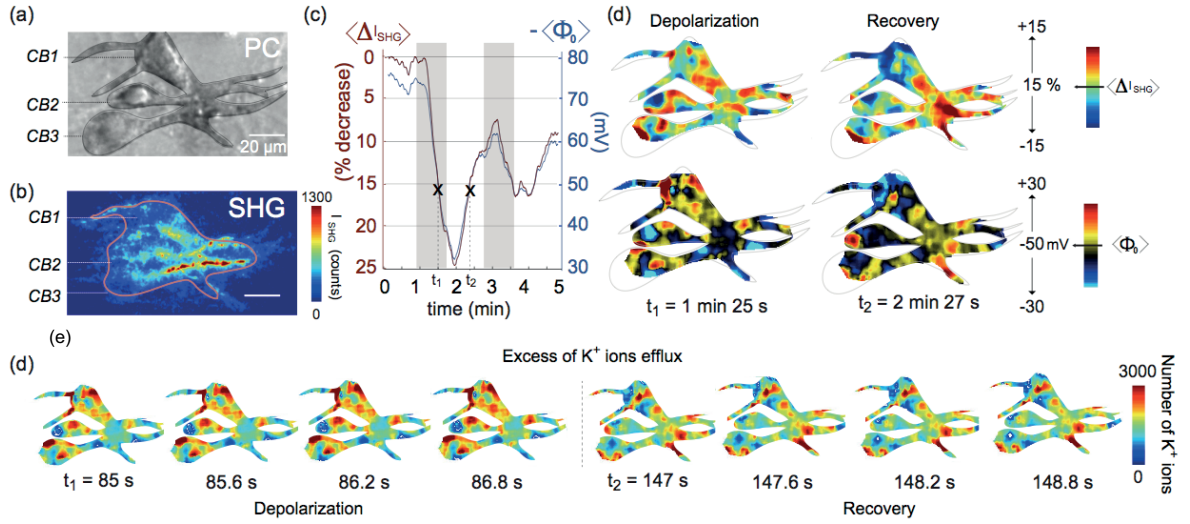

Figure 5.3: Spatiotemporal imaging of membrane potentials and ionic efflux by mean of the nonlinear optical response of water. (a) PC and corresponding label-free SH images (b) of cortical neurons, 15 days *in vitro*, CB states for cell body. Three CBs are seen in the image denoted by CB1, CB2 and CB3 and a bundle of several processes. The colored line in (b) indicates the area in which the membrane potential calculations were made. (c) Spatially averaged SH intensity (left axis, in %) changes as a function of time during application cycles of 50 mM K+ enriched extracellular solution. The average membrane potentials derived from the computational procedure are shown on the right axis (in mV). The time windows where the extracellular solution enriched in K^+ is applied are highlighted by the brown areas. (d) Top row: Images of the percentile change in the SH response at two different times (t_1 and t_2) in the membrane depolarization cycle, indicated by crosses in (c). The bottom images display the corresponding membrane potential maps (in mV). (e) Excess of K+ ion efflux showing snapshots of spatiotemporal dynamic changes with 600 ms intervals during the

continuous depolarization cycle from t_1 = 85 s to 86.2 s and during the recovery period from t_2 = 147 s to 148.2 s.

Figure 5.3 shows an implementation of the procedure. Figure 5.3a shows a PC image of neurons displaying three cell body's (CB) and several processes. Figure 5.3b displays an SH image recorded over a time span of 120 s prior to the membrane depolarization experiment. Upon changing the concentration of K^+ in the extracellular solution from 3 mM to 50 mM (during the time intervals from t=1 min to t=1.45 min and from t=2.45 min to t=3.40 min, highlighted by the brown areas) the spatially averaged SH intensity changes, dropping down by 25 %. When the flow is reversed back to a solution with a control concentration of K^+ of 3 mM the SH intensity recovers, although not fully due to the short waiting time, and then drops back down when the concentration of K^+ in the extracellular is switched back to 50 mM. The computed space-averaged membrane potential value $\langle \Delta\Phi \rangle$ is shown on the right axis and follows the trend of the SH intensity (Figure 5.3c). It can be seen that the average value agrees with the electrophysiological measurements of Figure 5.2b. Figure 5.3d shows pairs of images displaying the percentile changes in the second harmonic intensity (top) and the computed membrane potential maps (bottom) for an average membrane potential of -50 mV. The contours of the cell bodies and processes are highlighted by the thin black lines. Spatial fluctuations across the three neurons are visible in the different images. These fluctuations are, within the framework of the GHK equation, due to local and temporal fluctuations in ion channels activity. This agrees with recent super resolution fluorescent microscopy studies of fixed cells[271]. During the depolarization, the membrane potential reaches more positive values in the somas, while during the recovery the neurites display more positive membrane potential values. Hence, different parts of the cells (soma or neurites) are active at different points of the depolarization cycle. We can display these changes more clearly by considering that the membrane potential change is mainly affected by the change in the K^+ concentration (see Chapter 1 for more details). The charge that is transported through a membrane (ΔQ) can be modeled[272] by $\Delta Q = C_m \Delta\Phi$, with C_m the capacitance of the membrane. Taking a typical value[273] of C_m=1 μF/μm^2, and taking $\Delta\Phi$ from our SH images, ΔQ can be computed, which provides us with direct knowledge estimation of the flow of ions. Figure 5.3e shows 600 ms snapshots of ΔQ, which is here interpreted as the excess of K^+ ion exiting the cell membrane. Snapshots are shown for a few 600 ms intervals during the continuous depolarization cycle from t_1 = 85 s to 86.2 s and during the recovery period from t_2 = 147 s to 148.2 s. We observe that there is not only a non-uniform distribution and non-uniform density of K^+-permeant ion channels, but also a different temporal activity of the specific ionic efflux.

5.4 Conclusions

In this Chapter, we proposed the nonlinear optical response of membrane water as a new mechanism for probing membrane potentials and ion fluxes label-free. We have then used the endogenous response of interfacial water to image the sub-cellular and time dependent response of primary cortical cultured neurons to a potassium-enriched solution. The increase in the external K^+ concentration initiated a change in the resting membrane potential of the neurons. Electrophysiological recordings confirmed this well-known response. The temporal square rooted response of the SH intensity that originates from the oriented water consistently followed the same trend confirming expectations from nonlinear optical theory. We then analyzed the recorded images and constructed maps of the membrane potential as well as the K^+ ion flux. We observed temporal variations and spatial variations in the membrane potential and K^+ ion flux. We attribute these changes to a non-uniform distribution of ion channels within the neurons. Different parts of the cells are active at different parts of the depolarization cycle. Thus, within the framework of the GHK description, there is not only a non-uniform distribution and density of K^+-permeant ion channels, but also a different temporal activity. Being able to non-invasively probe membrane potentials and imaging ion fluxes opens up new avenues for understanding the signaling mechanisms inside single neurons or to the extent of a larger network. While the present 600 ms recordings are still longer than the duration of action potentials, future improvements to the optical layout and noise reduction may bring the recording time down to the 1 ms time scale.

Summary & Outlook

6.1 Summary

In this thesis, we used label-free second harmonic imaging to characterize morphological changes and electrical activity in cultured neurons. To implement this, we built two imaging systems capable to probe label-freely and non-invasively structural and electrical changes in living cells which can be resolved in time.

In the first Chapter of this thesis we characterized the high throughput wide-field SH imaging system in terms of optical layout, efficiency and time resolution. An increase in the detection efficiency was achieved by exploiting the quadratic dependence of the number of generated photons on the pulse energy, while keeping the fluence low. We performed label-free second harmonic and two photon fluorescence imaging of living neurons with short acquisition time and at very low fluences. Then, we demonstrated the possibility for high resolution *in vitro* imaging of cellular processes with specificity to translational and rotational motions with acquisition times in the microsecond range. The elastic nature of the light matter interactions ensures that rotational and translational tracks can be imaged for unlimited periods of time and with minimal invasion.

To continue with Chapter 2, we described the 3D wide-field high throughput SH microscope, the other imaging system we built. The use of a spatial light modulator allowed us to image samples in three dimensions and on the millisecond time scale, with a structurally illuminated wide-field configuration. In view to probe dynamical electrical neuronal activity, we implemented the microscope with an equipment adapted for live-cell imaging (temperature controller, open-bath chamber, patch-clamp).

In Chapter 3, we took advantage of the high imaging efficiency of the 3D wide-field high throughput SH microscope and the specific microtubules origin of the SH signal to perform polarimetry measurements on cultured neurons. From the polarization-dependent SH images, we computed the orientational distribution of microtubules in axons and dendrites and assigned a narrow orientational distribution to the specific microtubule organization of an axon.

With SH imaging, we also extracted information on the cytoskeleton stability as a function of the neurons' age, based on the resistance to nocodazole, a microtubule-specific drug. In the axon, it is

possible to relate the SH intensity variations to the relative change in the number of axonal microtubules upon nocodazole depolimerization. These measurements show the possibility of real-time *in vitro* label-free imaging of structural changes of the axonal microtubules.

In Chapter 4, we investigated microtubule organization (with polarimetric SHG) and metabolic activity (with 2PEF) in cultured neurons at different stage of their morphological development. We observed changes in the metabolic activity as well as changes in the microtubules organization in neurons throughout their development. From the polarization-dependent SH images, we calculated the coefficient of polarization (COP), which reports on orientational irregularities in the microtubule cytoskeleton. At the specific stage 3, 2PEF showed a high-level of metabolic activity at interstitial branching points on the outgrowing axon, colocalizing at places where a structural depolarization, as mapped by the COP, is visible. As neurons mature, 2PEF and SH responses indicated that structural degradations have taken place. Further analysis on the comparison of the 2PEF and the indirect SH intensities averaged from the cell body as a function of the neuronal maturity demonstrated that these imaging modalities can be used to distinguish between the three distinct important steps of the neuronal development: before, during and after the differentiation.

Capitalizing on the greatly improved efficiency of the 3D wide-field high throughput SH microscope, in Chapter 5, we proposed the nonlinear optical response of "membrane water" as a new probe for measuring membrane potentials and ion fluxes label-freely in cultured neurons. As an alternative to patch-clamp, we utilized the unique surface specificity and voltage sensitivity of label-free second harmonic generation to image the sub-cellular and time dependent depolarization responses of cultured neurons to a potassium-enriched solution. By comparison with patch-clamp measurements, SH imaging showed that changes in the neuron membrane potential correlated linearly with the square root of the SH intensity, as predicted by theory. We demonstrated the possibility of using the nonlinear optical response of the membrane-bound water to image and map spatiotemporal changes in the membrane potential and K^+ ion flux during a continuous depolarization. The observed spatio-temporal heterogeneities are attributable to a non-uniform spatial distribution and activity of ion channels. Being able to non-invasively probe membrane potentials at multiple sites opens up new avenues for understanding the signaling mechanism inside single neurons or within a large network.

6.2 Outlook

The initial motivation at the origin of this project was to use the principle of second harmonic scattering, a highly efficient nonlinear optical technique developed in the Laboratory for fundamental BioPhotonics, in order to build a highly efficient imaging system for live-cell measurements. Taking advantage of the voltage-sensitivity of the SH response as well as the noncentrosymmetric structures specificity of the SH signals, this imaging system had to be capable to probe structural and electrical changes, in living cells, label-free, in a non-invasive way and resolved in time. In this sense, we fulfilled our challenge, since we demonstrated in this thesis the possibilities of label-free SH imaging of structural changes and electrical activity in cultured neurons with high throughput wide-field and time-resolved SH microscopy. This work has opened up many possible directions for future studies.

We discussed the high throughput of the imaging systems in this thesis. An interesting outlook would be to explore the limit of the imaging efficiency with a direct application on probing the influence of microtubules orientation and disposition. The spatial resolution of the 3D wide-field SH microscope is 430 nm in (x,y). With this resolution, it is not possible to resolve 1 single microtubule (diameter of 25 nm, with varying length from 5 nm to 1 mm). However, SH imaging is inherently sensitive to the density and spatial organization of the SH active dipoles, which are in the neuronal cytoskeleton, the microtubules. It would be of great interest to "calibrate" the measured SH signal with the number of microtubules (instead of a relative change as performed in Chapter 3). One way to do so would be to reconstitute microtubules *in vitro* from tubulin in solution and with a specific orientational seeding (microtubules are sensitive to the application of an external electrical field and rearrange accordingly). Different models could be considered for parallel and anti-parallel microtubules and for bundles of varying densities and spacings. Additional existing techniques such as dynamic assay[279] with growing microtubules could be used to monitor the orientation of the microtubules. In these conditions, it would be of great interest to measure the SH response from the tailored microtubule samples and test the imaging efficiency limits of the microscope as a function of the orientation and density of microtubules. Follow ups may be devoted to monitor in a label-free way the absolute number of microtubules *in vivo*, by mean of high throughput label-free SH imaging and without the need of super resolution imaging or single-molecule fluoresence[280].

In Chapter 4, we performed SH polarimetry measurements and demonstrated how the orientational directionality of microtubules in neurites and cell bodies can be determined in a label-free manner. Microtubules are polar structures, they have a preferential orientation and direction with a “plus” and “minus-end” known as polarity. In axon, microtubules are oriented uniformly with their “plus-end”

distal to the cell body, whereas in dendrites they present a mixed polarity. Distinguishing the intrinsic direction of microtubules in a label-free way is a significant question in the biology and bio-imaging community nowadays[29]. Polarimetry is a powerful tool in SH imaging[231]. Varying the different polarization combination (linear, circular, cross polarized, etc…) for tailored microtubule samples would open up a possibility to retrieve the microtubule orientations. These experiments could be extended to *in vivo* time-resolved measurements. This would bring great advances in the understanding of how the microtubules migrate and organize themselves in the cytoskeleton. This knowledge is essential to follow the establishment of the neuronal polarity in the cytoskeleton, from the early stage after mitosis to the late maturation[29]. Again, a label-free imaging technique present many advantages over the immunostaining existing techniques. Being able to observe label-free morphological changes in the cytoskeleton of living neurons, with clear markers of organization, would allow to follow neuronal differentiation in detail without affecting the cells. This enables a possibility of long term screening to determine the effects of pharmacological drugs or diseases that alter the structural functioning of the nervous systems. One example is the influence of neurodegenerative processes on the structural integrity of the cytoskeleton[276]. The introduced techniques could also be combined with targeted fluorescence studies or optogenetics to follow in more detail the intricate complexities of the cytoskeleton involved in the nervous system.

In Chapter 5, we demonstrated by probing the membrane-water SH response, a possibility to perform label-free, time-resolved imaging of electrical activity in cultured neurons. SHG is a two-photon process that is active on a non-centrosymmetry structures. The lack of symmetry comes from the intrinsic properties of the material itself, its structural arrangement on a molecular and macromolecular scale, or from breaking the orientation distribution symmetry of molecules either at interfaces or with the application of an electrical field. Our results, in agreement with invasive patch-clamp measurements, demonstrated the power of SH imaging in the measurements of electrical neuronal activity. The detected SH signal and the specific imaging configuration of the 3D wide-field SH microscope, highlighted the fact that the SH signal comes from the breakage of the orientation distribution symmetry of molecules with the application of an electric field (electrical gradient between the inside and outside of the cell) and from the microtubules-based cytoskeleton itself. There is an emerging question nowadays about the implication of the cytoskeleton in the electrical activity of the neurons[281]. Few studies have been conducted on this topic[282-283], either because of the lack of sensitivity of the techniques or the invasive-characteristic of the existing techniques to measure electrical neuronal signals. However, from literature, some evidence suggests that the microtubules network may interact with membrane components modulating membrane potential[284-287], and models

have been proposed to explain the existence of a generated electric field from microtubules[283]. The origin of this electrical field, has be defined such as coming from the difference between the growth rate of the polymerization, where the tubulin attaches to the free plus-end microtubule and the GTP hydrolyses into GDP, and the hydrolyses[282-283]. This difference, leading to energy storage in the microtubules, induces vibrations in microtubules and generates an electrical field. Further studies on the actual role of the microtubules network in the electric activity of neurons should be conducted to emphasize our results and explore further the influence of the cytoskeleton in the membrane potential regulation. A microtubules-stabilizing drug such as cytochalasin D or taxol, and the simultaneous use of patch-clamp measurements while performing SH imaging could be of use. Obviously, being able to non-invasively probe membrane potentials in cultured neurons opens up new avenues for understanding the signaling mechanisms in which polarization-resolved SH imaging finds a significant importance. In this sense, the high throughput label-free, SH imaging system developed in this thesis surely constitutes the key answer in this questioning.

List of Publications

The present thesis is based on the following publications / manuscripts:

Chapter 2:

Macias-Romero, C., Didier, M., Zubkovs, V., Delannoy, L., Dutto, F., Radenovic, A., and Roke, S. Probing rotational and translational diffusion of nanodoublers in living cells on microsecond time scales *Nano Letters,* **15,** 2552–2557 (2014).

Macias-Romero, C., Didier, M., Jourdain, P., Marquet, P., Magistretti, P., Tarun, O. B., Zubkovs, V., and Roke, S. High throughput second harmonic imaging for label-free biological applications *Opt. Express,* **22,** 31102–31112 (2014).

Chapter 3:

Didier, M., Macias-Romero, C., Teulon, C., Jourdain, P., and Roke, S. Mapping of morphological changes in the neuronal cytoskeleton with endogenous second harmonic imaging: A case study of nocodazole *submitted, in the process of responding to referees, Cytoskeleton* (2018).

Chapter 4:

Didier, M., P. Jourdain, and Roke, S. Probing neuronal morphology and metabolic activity with label-free SH polarimetry and endogenous 2PEF *manuscript in preparation,* (2018).

Chapter 5:

Didier, M., Tarun, O. B., Jourdain, P., Magistretti, P. and Roke, S. Membrane water as a probe for neuronal membrane potentials and ionic flux at the single cell level *sumitted, in the process of responding to referees, Nature Com.* (2018).

Bibliography

1. Bray, D. Sympathetic Patterns Neurons of Individual in Culture. *J. Cell Biol.* **56,** 702–712 (1973).
2. Dotti, G., Sullivan, A., Biology, C., College, A. M. & York, N. The Establishment of Polarity by Hippocampal. *J. Neurosci.* **8,** 1454–1468 (1988).
3. Dent, E. W. & Kalil, K. Axon branching requires interactions between dynamic microtubules and actin filaments. *J. Neurosci.* **21,** 9757–9769 (2001).
4. Miller, F. D. & Kaplan, D. R. Signaling mechanisms underlying dendrite formation. *Curr. Opin. Neurobiol.* **13,** 391–398 (2003).
5. Neves, S. R. *et al.* Cell shape and negative links in regulatory motifs together control spatial information flow in signaling networks. *Cell* **133,** 666–680 (2009).
6. Baas, P. W. Microtubules and neuronal polarity: Lessons from mitosis. *Neuron* **22,** 23–31 (1999).
7. Janmey, P. in *Handbook of Biological Physics* (eds. Lipowsky, R. & Sackmann, E.) **1,** 805–849 (1995).
8. Heidemann, S. R. & McIntosh, J. R. Visualization of the structural polarity of microtubules. *Nature* **286,** 517–519 (1980).
9. Mandell, J. W. & Banker, G. a. The microtubule cytoskeleton and the development of neuronal polarity. *Neurobiol. Aging* **16,** 229–37; discussion 238 (1995).
10. Burton, P. R. Dendrites of mitral cell neurons contain microtubules of opposite polarity. *Brain Res.* **473,** 107–115 (1988).
11. Baas, P. W. & Lin, S. Orientation Hooks and Comets: The Story of Microtubule Polarity Orientation in the Neuron the Neuron. *Dev. Neurobiol.* **71,** 403–418 (2012).
12. Yau, K. W. *et al.* Dendrites In Vitro and In Vivo Contain Microtubules of Opposite Polarity and Axon Formation Correlates with Uniform Plus-End-Out Microtubule Orientation. *J. Neurosci.* **36,** 1071–1085 (2016).
13. Conde, C. & Cáceres, A. Microtubule assembly, organization and dynamics in axons and dendrites. *Nat. Rev. Neurosci.* **10,** 319–332 (2009).
14. Dubey, J., Ratnakaran, N. & Koushika, S. P. Corrigendum: Neurodegeneration and microtubule dynamics: death by a thousand cuts. *Front. Cell. Neurosci.* **10,** 1–15 (2016).

15. Lüders, J. *The Microtubule Cytoskeleton*. Springer (2016).
16. Stepanova, T. *et al.* Visualization of microtubule growth in cultured neurons via the use of EB3-GFP (end-binding protein 3-green fluorescent protein). *J. Neurosci.* **23,** 2655–2664 (2003).
17. Lüders, J. & Stearns, T. Microtubule-organizing centres: a re-evaluation. *Nat. Rev. Mol. Cell Biol.* **8,** 161–167 (2007).
18. Stiess, M. *et al.* Axon extension occurs independently of centrosomal microtubule nucleation. *Science* **327,** 704–707 (2010).
19. Zhunussova, A. *et al.* Tumor microenvironment promotes dicarboxylic acid carrier-mediated transport of succinate to fuel prostate cancer mitochondria. *Am. J. Cancer Res.* **5,** 1665–1679 (2015).
20. Sanders, A. A. W. M. & Kaverina, I. Nucleation and Dynamics of Golgi-derived Microtubules. **9,** 1–7 (2015).
21. Jiang, K. & Akhmanova, A. Microtubule tip-interacting proteins: A view from both ends. *Curr. Opin. Cell Biol.* **23,** 94–101 (2011).
22. Mitchison, T. & Kirschner, M. Dynamic instability of microtubule growth. *Nature* **312,** 237–241 (1984).
23. Margolis, R. L. & Wilson, L. Opposite end assembly and disassembly of microtubules at steady state in vitro. *Cell* **13,** 1–8 (1978).
24. Salmon, E. D., McKeel, M. & Hays, T. Rapid rate of tubulin dissociation from microtubules in the mitotic spindle in vivo measured by blocking polymerization with colchicine. *J. Cell Biol.* **99,** 1066–1075 (1984).
25. Gierke, S., Kumar, P. & Wittmann, T. Analysis of Microtubule Polymerization Dynamics in Live Cells. *Methods Cell Biol.* **97,** 15–33 (2010).
26. Baas, P. W., Slaughter, T., Brown, A. & Black, M. M. Microtubule dynamics in axons and dendrites. *J. Neurosci. Res.* **30,** 134–153 (1991).
27. Kollins, K. M., Bell, R. L., Butts, M. & Withers, G. S. Dendrites differ from axons in patterns of microtubule stability and polymerization during development. *Neural Dev.* **4,** 26 (2009).
28. Schek, H. T., Gardner, M. K., Cheng, J., Odde, D. J. & Hunt, A. J. Microtubule Assembly Dynamics at the Nanoscale. *Curr. Biol.* **17,** 1445–1455 (2007).
29. Kapitein, L. C. & Hoogenraad, C. C. Which way to go? Cytoskeletal organization and polarized transport in neurons. *Mol. Cell. Neurosci.* **46,** 9–20 (2011).
30. Desai, A. & Mitchison, T. J. Microtubule polymerization dynamics. *Annu. Rev. Cell Dev. Biol* **13,** 83–117 (1997).

31. Alushin, G. M. *et al.* High-Resolution Microtubule Structures Reveal the Structural Transitions in ab -Tubulin upon GTP Hydrolysis. *Cell* **157,** 1117–1129 (2014).
32. Baas, P. W. & Ahmad, F. J. The plus ends of stable microtubules are the exclusive nucleating structures for microtubules in the axon. *J. Cell Biol.* **116,** 1231–41 (1992).
33. Kapitein, L. C. & Hoogenraad, C. C. Building the Neuronal Microtubule Cytoskeleton. *Neuron* 492–506 (2015).
34. Skala, M. C. *et al.* In vivo multiphoton microscopy of NADH and FAD redox states, fluorescence lifetimes, and cellular morphology in precancerous epithelia. *Proc. Natl. Acad. Sci.* **104,** 19494–19499 (2007).
35. Wu, K., Canterbury, J. D., Wilson, P. T. & Downer, M. C. Electric-field-induced second-harmonic microscopy. *Phys. Status Solidi C Conf.* **3085,** 3081–3085 (2003).
36. Zipfel, W. R. *et al.* Live tissue intrinsic emission microscopy using multiphoton-excited native fluorescence and second harmonic generation. *Proc. Natl. Acad. Sci. U. S. A.* **100,** 7075–80 (2003).
37. Allen, K. B., Sasoglu, F. M. & Layton, B. E. Cytoskeleton-membrane interactions in neuronal growth cones: a finite analysis study. *J. Biomech. Eng.* **131,** 021006 (2009).
38. Knobloch, M. *et al.* Metabolic control of adult neural stem cell activity by Fasn-dependent lipogenesis. *Nature* **493,** 226–230 (2013).
39. Attwell, D. & Laughlin, S. B. An energy budget for signalling in the grey matter of the brain. *J. Cereb. Blood Flow Metab.* **21,** 1133–1145 (2001).
40. Andersen, J. K. Oxidative stress in neurodegeneration: Cause or consequence? *Nat. Rev. Neurosci.* **10,** S18 (2004).
41. Georgakoudi, I. & Quinn, K. P. Optical Imaging Using Endogenous Contrast to Assess Metabolic State. *Annu. Rev. Biomed. Eng.* **14,** 351–367 (2012).
42. Agostini, M. *et al.* Metabolic reprogramming during neuronal differentiation. *Cell Death Differ.* **23,** 1502–1514 (2016).
43. Chang, D. T. W., Honick, A. S. & Reynolds, I. J. Mitochondrial Trafficking to Synapses in Cultured Primary Cortical Neurons. *J. Neurosci.* **26,** 7035–7045 (2006).
44. Bartlett, W. P. & Banker, G. A. An electron microscopic study of the development of axons and dendrites by hippocampal neurons in culture. *J. Neurosci.* **4,** 1954–65 (1984).
45. Peters, A., Proskauer, C. & Kaiserman-Abramof, I. The small pyramidal neuron of the rat cerebral cortex. The Axon Hillock and Initial Segment. *J. Cell Biol.* **39,** 604–619 (1968).
46. Heidemann, S. R., Landers, J. M. & Hamborg, M. A. Polarity orientation of axonal microtubules. *J. Cell Biol.* **91,** 661–665 (1981).

47. Bray, D. & Bunge, M. B. Serial analysis of microtubules in cultured rat sensory axons. *J. Neurocytol.* **10,** 589–605 (1981).
48. Yu, W. & Baas, P. W. Changes in microtubule number and length during axon differentiation. *J. Neurosci.* **14,** 2818–2829 (1994).
49. Mudrakola, H. V., Zhang, K. & Cui, B. Optically Resolving Individual Microtubules in Live Axons. *Structure* **17,** 1433–1441 (2009).
50. Mikhaylova, M. *et al.* Resolving bundled microtubules using anti-tubulin nanobodies. *Nat. Commun.* **6,** 1–7 (2015).
51. Yu, C. H. *et al.* Measuring microtubule polarity in spindles with second-harmonic generation. *Biophys. J.* (2014).
52. Kuczmarski, E. R. & Rosenbaum, J. L. Chick brain actin and myosin Isolation and Characterization. *J. Cell Biol.* **80,** 341–355 (1979).
53. Wang, S. J., Xu, X. J., Wu, Z. X., Huang, Z. G. & Wang, Y. H. Influence of synaptic interaction on firing synchronization and spike death in excitatory neuronal networks. *Phys. Rev. E - Stat. Nonlinear, Soft Matter Phys.* (2008).
54. Maglione, M. & Sigrist, S. J. Seeing the forest tree by tree: Super-resolution light microscopy meets the neurosciences. *Nat. Neurosci.* **16,** 790–797 (2013).
55. Leterrier, C., Dubey, P. & Roy, S. The nano-architecture of the axonal cytoskeleton. *Nat. Publ. Gr.* **18,** 713–726 (2017).
56. Horio, T. & Hirokazu, H. Visualization of the dynamic instability of individual microtubules by dark-field microscopy. *Nature* **319,** 402–403 (1986).
57. Sammak, P. J. & Borisy, G. G. Direct observation of microtubule dynamics in living cells. *Nature* **332,** 724–6 (1988).
58. Haraguchi, T., Kaneda, T. & Hiraoka, Y. Dynamics of chromosomes and microtubules visualized by multiple-wavelength fluorescence imaging in living mammalian cells: Effects of mitotic inhibitors on cell cycle progression. *Genes to Cells* **2,** 369–380 (1997).
59. Bailey, M., Conway, L., Gramlich, M. W., Hawkins, T. L. & Ross, J. L. Modern methods to interrogate microtubule dynamics. *Integr. Biol. (Camb).* **5,** 1324–33 (2013).
60. Webster, D. R., Gundersen, G. G., Bulinski, J. C. & Borisy, G. G. Differential turnover of tyrosinated and detyrosinated microtubules. *Proc. Natl. Acad. Sci. U. S. A.* **84,** 9040–9044 (1987).
61. Rusan, N. M., Fagerstrom, C. J., Yvon, A. M. & Wadsworth, P. Cell cycle-dependent changes in microtubule dynamics in living cells expressing green fluorescent protein-alpha tubulin. *Mol. Biol. Cell* **12,** 971–80 (2001).

62. Bon, P., Lécart, S., Fort, E. & Lévêque-Fort, S. Fast label-free cytoskeletal network imaging in living mammalian cells. *Biophys. J.* **106,** 1588–1595 (2014).
63. Demchouk, A. O., Gardner, M. K. & Odde, D. J. Microtubule tip tracking and tip structures at the nanometer scale using digital fluorescence microscopy. *Cell. Mol. Bioeng.* **4,** 192–204 (2011).
64. Lee, J. C., Field, D. J. & Lee, L. L. Effects of nocodazole on structures of calf brain tubulin. *Biochemistry* **19,** 6209–6215 (1980).
65. Liao, G., Nagasaki, T. & Gundersen, G. G. Low concentrations of nocodazole interfere with fibroblast locomotion without significantly affecting microtubule level: implications for the role of dynamic microtubules in cell locomotion. *J. Cell Sci.* **108,** 3473–3483 (1995).
66. Witte, H., Neukirchen, D. & Bradke, F. Microtubule stabilization specifies initial neuronal polarization. *J. Cell Biol.* **180,** 619–632 (2008).
67. Wilson, L. & Jordan, M. A. Microtubule dynamics: taking aim at a moving target. *Chem. Biol.* **2,** 569–573 (1995).
68. Marklund, U., Larsson, N., Gradin, H. M., Brattsand, G. & Gullberg, M. Oncoprotein 18 is a phosphorylation-responsive regulator of microtubule dynamics. *EMBO J.* **15,** 5290–8 (1996).
69. Dombeck, D. A. *et al.* Uniform polarity microtubule assemblies imaged in native brain tissue by second-harmonic generation microscopy. *Proc. Natl. Acad. Sci. U. S. A.* **100,** 7081–7086 (2003).
70. Stoothoff, W. H., Bacskai, B. J. & Hyman, B. T. Monitoring tau-tubulin interactions utilizing second harmonic generation in living neurons. (2008).
71. Kwan, A. C., Dombeck, D. A. & Webb, W. W. Polarized microtubule arrays in apical dendrites and axons. *Proc. Natl. Acad. Sci. U. S. A.* **105,** 11370–11375 (2008).
72. Peterka, D. S., Takahashi, H. & Yuste, R. Imaging voltage in neurons. *Neuron* **69,** 9–21 (2011).
73. Baas, P. W., Deitch, J. S., Black, M. M. & Banker, G. A. Polarity orientation of microtubules in hippocampal neurons: Uniformity in the axon and nonuniformity in the dendrite. *Neurobiology* **85,** 8335–8339 (1988).
74. Akhmanova, A. & Steinmetz, M. O. Tracking the ends: a dynamic protein network controls the fate of microtubule tips. *Nat. Rev. Mol. Cell Biol.* **9,** 309–22 (2008).
75. Kandel, E., Schwartz, J. & Jessell, T. *Principles of neural science*. (2013).
76. Hamill, O. P., Marty, A., Neher, E., Sakmann, B. & Sigworth, F. J. Improved patch-clamp techniques for high-resolution current recording from cells and cell-free membrane patches. *Pflügers Arch. Eur. J. Physiol.* **391,** 85–100 (1981).
77. Jun, J. J. *et al.* Fully integrated silicon probes for high-density recording of neural activity.

Nature **551,** 232–236 (2017).

78. Cohen, L. B., Keynes, R. D. & Hille, B. Light Scattering and Birefringence Changes during Nerve activity. *Nature* **218,** 438–441 (1968).
79. Tsien, R. Y. New Calcium Indicators and Buffers with High Selectivity Against Magnesium and Protons: Design, Synthesis, and Properties of Prototype Structures. *Biochemistry* **19,** 2396–2404 (1980).
80. Kloppenburg, P., Zipfel, W. R., Webb, W. W. & Harris-warrick, R. M. Highly Localized Ca 2% Accumulation Revealed by Multiphoton Microscopy in an Identified Motoneuron and Its Modulation by Dopamine. *J. Neurosci.* **20,** 2523–2533 (2000).
81. Stosiek, C., Garaschuk, O., Holthoff, K. & Konnerth, A. In vivo two-photon calcium imaging of neuronal networks. *Proc. Natl. Acad. Sci. U. S. A.* **100,** 7319–7324 (2003).
82. Chemla, S. & Chavane, F. Voltage-sensitive dye imaging: Technique review and models. *J. Physiol. Paris* **104,** 40–50 (2004).
83. Jiang, J., Eisenthal, K. B. & Yuste, R. Second Harmonic Generation in Neurons: Electro-Optic Mechanism of Membrane Potential Sensitivity. *Biophys. J.* **93,** L26–L28 (2007).
84. Nuriya, M., Jiang, J., Nemet, B., Eisenthal, K. B. & Yuste, R. Imaging membrane potential in dendritic spines. *Proc. Natl. Acad. Sci. U. S. A.* **103,** 786–90 (2006).
85. Nuriya, M. & Yasui, M. Membrane potential dynamics of axons in cultured hippocampal neurons probed by second-harmonic-generation imaging. *J. Biomed. Opt.* **15,** 020503-1 (2010).
86. Theer, P., Denk, W., Sheves, M., Lewis, A. & Detwiler, P. B. Second-harmonic generation imaging of membrane potential with retinal analogues. *Biophysical journal* **100,** 232–42 (2011).
87. Mennerick, S. *et al.* Diverse voltage-sensitive dyes modulate GABA A receptor function. *J. Neurosci.* **30,** 2871–2879 (2010).
88. Packer, A. M., Roska, B. & Häusser, M. Targeting neurons and photons for optogenetics. *Nat. Publ. Gr.* **16,** (2013).
89. Knöpfel, T., Díez-García, J. & Akemann, W. Optical probing of neuronal circuit dynamics: Genetically encoded versus classical fluorescent sensors. *Trends Neurosci.* **29,** 160–6 (2006).
90. LaPorta, A. & Kleinfeld, D. Interferometric detection of action potentials. *Cold Spring Harb. Protoc.* **2012,** 307–11 (2012).
91. Cotte, Y. *et al.* Marker-free phase nanoscopy. **7,** 113–118 (2013).
92. Liu, B. *et al.* Label-free spectroscopic detection of membrane potential using stimulated Raman scattering. *Appl. Phys. Lett.* **106,** 1–4 (2015).

93. Maiman, T. H. Stimulated optical radiation in Ruby. *Nature* **187,** 493–494 (1960).
94. Hellwarth, Ro. & Christensen, P. Nonlinear Optical Microscope Using Seconf Harmonic Generation. *Appl. Opt.* **14,** 247–248 (1974).
95. Ustione, A. & Piston, D. W. A simple introduction to multiphoton microscopy. *J. Microsc.* **243,** 221–226 (2011).
96. Mulligan, S. J. & Macvicar, B. A. Two-Photon Fluorescence Microscopy : Basic Principles , Advantages and Risks. *Mod. Res. Educ. Top. Microsc.* 881–889 (2007).
97. Nikolenko, V. SLM microscopy: scanless two-photon imaging and photostimulation using spatial light modulators. *Front. Neural Circuits* **2,** 1–14 (2008).
98. Papagiakoumou, E., de Sars, V., Oron, D. & Emiliani, V. Patterned two-photon illumination by spatiotemporal shaping of ultrashort pulses. *Opt. Express* **16,** 22039 (2008).
99. Müller, W. & Connor, J. A. Dendritic spines as individual neuronal compartments for synaptic Ca2+ responses. *Nature* **354,** 73–76 (1991).
100. Ohki, K., Chung, S., Ch, Y. H., Kara, P. & Reid, R. C. Functional imaging with cellular resolution reveals precise micro- architecture in visual cortex. *Nature* **433,** 597–603 (2005).
101. Freund, I. & Deutsch, M. Second-harmonic microscopy of biological tissue. *Opt. Lett.* **11,** 94 (1986).
102. Campagnola, P. J. & Loew, L. M. Second-harmonic imaging microscopy for visualizing biomolecular arrays in cells, tissues and organisms. *Nat. Biotechnol.* **21,** 1356–1360 (2003).
103. Fung, D. T. *et al.* Second harmonic generation imaging and fourier transform spectral analysis reveal damage in fatigue-loaded tendons. *Ann. Biomed. Eng.* **38,** 1741–1751 (2010).
104. Plotnikov, S. V, Millard, A. C., Campagnola, P. J. & Mohler, W. A. Characterization of the Myosin-Based Source for Second-Harmonic Generation from Muscle Sarcomeres. *Biophys. J.* **90,** 693–703 (2006).
105. Nucciotti, V. *et al.* Probing myosin structural conformation in vivo by second-harmonic generation microscopy. *Proc. Natl. Acad. Sci. U. S. A.* **107,** 7763–8 (2010).
106. Hallock, A. J., Redmond, P. L. & Brus, L. E. Optical forces between metallic particles. *Proc. Natl. Acad. Sci.* **102,** 1280–1284 (2004).
107. Sheppard, C. J. R. & Wilson, T. The theory of scanning microscopes with Gaussian pupil functions. *J. Microsc.* **114,** 179–197 (1978).
108. Masters, B. R. & So, P. *Handbook of Biomedical Nonlinear Optical Microscopy*. (Oxford University Press, 2008).
109. Denk, W., Strickler, J. H. & Webb, W. W. Two-photon laser scanning fluorescence microscopy. *Science* **248,** 73–76 (1990).

110. Flörsheimer, M., Bosch, M., Brillert, C., Wierschem, M. & Fuchs, H. Second-harmonic imaging of surface order and symmetry. *Thin Solid Films* **327–329,** 241–246 (1998).
111. Flörsheimer, M. *et al.* Second-harmonic imaging of ferroelectric domains in LiNbO3with micron resolution in lateral and axial directions. *Appl. Phys. B Lasers Opt.* **67,** 593–599 (1998).
112. Kriech, M. A. & Conboy, J. C. Imaging chirality with surface second harmonic generation microscopy. *J. Am. Chem. Soc.* (2005).
113. Nguyen, T. T. & Conboy, J. C. High-throughput screening of drug-lipid membrane interactions via counter-propagating second harmonic generation imaging. *Anal. Chem.* **83,** 5979–5988 (2011).
114. Kriech, M. A. & Conboy, J. C. Counterpropagating second-harmonic generation: a new technique for the investigation of molecular chirality at surfaces. *J. Opt. Soc. Am. B* **21,** 1013 (2004).
115. Peterson, M. D. *et al.* Second harmonic generation imaging with a kHz amplifier. *Opt. Mater. Express* **1,** 57 (2011).
116. Gualtieri, E. J. *et al.* Detection of membrane protein two-dimensional crystals in living cells. *Biophys. J.* **100,** 207–214 (2011).
117. Dewalt, E. L. *et al.* Polarization-resolved second-harmonic generation microscopy as a method to visualize protein-crystal domains. *Acta Crystallogr. Sect. D Biol. Crystallogr.* **69,** 74–81 (2013).
118. Wampler, R. D. *et al.* Selective Detection of Protein Crystals by Second Harmonic Microscopy. *J. Am. Chem. Soc.* **130,** 14076–14077 (2008).
119. Moreaux, L., Sandre, O., Blanchard-Desce, M. & Mertz, J. Membrane imaging by simultaneous second-harmonic generation and two-photon microscopy. *Opt. Lett.* **25,** 678 (2000).
120. Campagnola, P. J., Wei, M., Lewis, A. & Loew, L. M. High-Resolution Nonlinear Optical Imaging of Live Cells by Second Harmonic Generation. **77,** 3341–3349 (1999).
121. Brown, E. *et al.* Dynamic imaging of collagen and its modulation in tumors in vivo using second-harmonic generation. *Nat. Med.* **9,** 796–800 (2003).
122. Campagnola, P. J. *et al.* Three-Dimensional High-Resolution Second-Harmonic Generation Imaging of Endogenous Structural Proteins in Biological Tissues. *Biophys. J.* **81,** 493–508 (2002).
123. Campagnola, P. J. & Loew, L. M. Second-harmonic imaging microscopy for visualizing biomolecular arrays in cells, tissues and organisms. *Nat. Biotechnol.* **21,** 1356–60 (2003).
124. Dombeck, D. A. *et al.* Uniform polarity microtubule assemblies imaged in native brain tissue

by second-harmonic generation microscopy. *Proc. Natl. Acad. Sci. U. S. A.* **100,** 7081–6 (2003).

125. Kwan, A. C., Duff, K., Gouras, G. K. & Webb, W. W. Optical visualization of Alzheimer's pathology via multiphoton- excited intrinsic fluorescence and second harmonic generation. *Opt. Express* **17,** 3679–3689 (2009).
126. Psilodimitrakopoulos, S. *et al.* Quantitative imaging of microtubule alteration as an early marker of axonal degeneration after ischemia in neurons. *Biophys. J.* **104,** 968–975 (2013).
127. Campagnola, P. Second Harmonic Generation Imaging Microscopy: Applications to Diseases Diagnostics. *Anal. Chem.* **83,** 3224–3231 (2012).
128. Suhalim, J. L. *et al.* Characterization of cholesterol crystals in atherosclerotic plaques using stimulated Raman scattering and second-harmonic generation microscopy. *Biophys. J.* **102,** 1988–95 (2012).
129. Latour, G. *et al.* Hyperglycemia-Induced Abnormalities in Rat and Human Corneas: The Potential of Second Harmonic Generation Microscopy. *PLoS One* **7,** 48388–48399 (2012).
130. Latour, G. *et al.* In vivo structural imaging of the cornea by polarization-resolved second harmonic microscopy. *Exp. Ophthalmol* **37,** 100–117 (2009).
131. Dombeck, D. A., Blanchard-Desce, M. & Webb, W. W. Optical recording of action potentials with second-harmonic generation microscopy. *J. Neurosci.* **24,** 999–1003 (2004).
132. Sacconi, L., Dombeck, D. A. & Webb, W. W. Overcoming photodamage in second-harmonic generation microscopy: real-time optical recording of neuronal action potentials. *Proc. Natl. Acad. Sci. U. S. A.* **103,** 3124–3129 (2006).
133. Nemet, B. A., Nikolenko, V. & Yuste, R. Second harmonic imaging of membrane potential of neurons with retinal. *J. Biomed. Opt.* **9,** 873–881 (2004).
134. Nuriya, M., Jiang, J., Nemet, B., Eisenthal, K. B. & Yuste, R. Imaging membrane potential in dendritic spines. *Proc. Natl. Acad. Sci. U. S. A.* **103,** 786–790 (2006).
135. Araya, R., Eisenthal, K. B. & Yuste, R. Dendritic spines linearize the summation of excitatory potentials. *Proc. Natl. Acad. Sci.* **103,** 18799–18804 (2006).
136. Hsieh, C.-L., Pu, Y., Grange, R. & Psaltis, D. Second harmonic generation from nanocrystals under linearly and circularly polarized excitations. *Opt. Express* **18,** 11917–11932 (2010).
137. Pantazis, P., Maloney, J., Wu, D. & Fraser, S. E. Second harmonic generating (SHG) nanoprobes for in vivo imaging. *Proc. Natl. Acad. Sci. U. S. A.* **107,** 14535–14540 (2010).
138. Čulić-Viskota, J., Dempsey, W. P., Fraser, S. E. & Pantazis, P. Surface functionalization of barium titanate SHG nanoprobes for in vivo imaging in zebrafish. *Nat. Protoc.* **7,** 1618–33 (2012).

139. Dempsey, W. P., Fraser, S. E. & Pantazis, P. SHG nanoprobes: advancing harmonic imaging in biology. *Bioessays* **34,** 351–60 (2012).
140. Pantazis, P., Pu, Y., Psaltis, D. & Fraser, S. Second harmonic generating (SHG) nanoprobes: a new tool for biomedical imaging. *Proc. SPIE* **7183,** 71831P (2009).
141. Grange, R., Lanvin, T., Hsieh, C.-L., Pu, Y. & Psaltis, D. Imaging with second-harmonic radiation probes in living tissue. *Biomed. Opt. Express* **2,** 2532 (2011).
142. So, P. T. C., Yew, E. Y. S. & Rowlands, C. High-throughput nonlinear optical microscopy. *Biophys. J.* **105,** 2641–2654 (2013).
143. Hoover, E. E. & Squier, J. A. Advances in multiphoton microscopy technology. *Nat. Photonics* **7,** 93–101 (2013).
144. Kim, K. H., Buehler, C. & So, P. T. High-speed, two-photon scanning microscope. *Appl. Opt.* **38,** 6004–6009 (1999).
145. Iyer, V., Hoogland, T. & Saggau, P. Fast Functional Imaging of Single Neurons Using Random-Access Multiphoton (RAMP) Microscopy. *J. Neurophysiol.* **95,** 535–545 (2005).
146. Sly, K. L., Nguyen, T. T. & Conboy, J. C. Lens-less surface second harmonic imaging. *Opt. Express* **20,** 21953 (2012).
147. Pu, Y., Centurion, M. & Psaltis, D. Harmonic holography: a new holographic principle. *Appl. Opt.* **47,** A103–A110 (2008).
148. Masihzadeh, O., Schlup, P. & Bartels, R. A. Label-free second harmonic generation holographic microscopy of biological specimens. *Opt. Express* **18,** 9840–9851 (2010).
149. Bewersdorf, O., Pick, R. & Hell, S. W. Multifocal multiphoton microscopy. *Opt. Lett.* **23,** 655–657 (1998).
150. Bahlmann, K. *et al.* Multifocal multiphoton microscopy (MMM) at a frame rate beyond 600 Hz. *Opt. Express* **15,** 10991–10998 (2007).
151. Zhu, G., van Howe, J., Durst, M., Zipfel, W. & Xu, C. Simultaneous spatial and temporal focusing of femtosecond pulses. *Opt. Express* **13,** 2153–2159 (2005).
152. Oron, D., Tal, E. & Silberberg, Y. Scanningless depth-resolved microscopy. *Opt. Express* **13,** 1468–1476 (2005).
153. Vaziri, A. & Shank, C. V. Ultrafast widefield optical sectioning microscopy by multifocal temporal focusing. *Opt. Express* **18,** 19645–55 (2010).
154. Cheng, L.-C. *et al.* Spatiotemporal focusing-based widefield multiphoton microscopy for fast optical sectioning. *Opt. Express* **20,** 8939–8948 (2012).
155. Choi, H. *et al.* Improvement of axial resolution and contrast in temporally focused widefield two-photon microscopy with structured light illumination. *Biomed. Opt.* **4,** 19645–19655

(2013).

156. Gomopoulos, N., Lütgebaucks, C., Sun, Q., Macias-Romero, C. & Roke, S. Label-free second harmonic and hyper Rayleigh scattering with high efficiency. *Opt. Express* **21,** 815 (2013).
157. Dadap, J. I. *et al.* Analysis of Second-Harmonic Generation Ultrashort Laser Pulses at Si (001) Interfaces. *IEEE J. Sel. Top. Quantum Electron.* **1,** 1145–1155 (1995).
158. Roke, S., Bonn, M. & Petukhov, A. V. Nonlinear optical scattering: The concept of effective susceptibility. *Phys. Rev. B - Condens. Matter Mater. Phys.* **70,** 1–10 (2004).
159. Macias-Romero, C. *et al.* High throughput second harmonic imaging for label-free biological applications. *Opt. Express* **22,** 31102 (2014).
160. Le Harzic, R., Riemann, I., König, K., Wüllner, C. & Donitzky, C. Influence of femtosecond laser pulse irradiation on the viability of cells at 1035, 517, and 345 nm. *J. Appl. Phys.* **102,** 114701–114702 (2007).
161. Vogel, A., Linz, N., Freidank, S. & Paltauf, G. Femtosecond-laser-induced nanocavitation in water: Implications for optical breakdown threshold and cell surgery. *Phys. Rev. Lett.* **100,** 1–4 (2008).
162. König, K. Multiphoton microscopy in life sciences. *J. Microsc.* **200,** 83–104 (2000).
163. Therrien, O. D., Aub, B., Pag, S. & Koninck, P. De. Wide-field multiphoton imaging of cellular dynamics in thick tissue by temporal focusing and patterned illumination. *Opt. Express* **2,** 696–704 (2011).
164. Saxton, W. M. *et al.* Tubulin dynamics in cultured mammalian cells. *J. Cell Biol.* **99,** 2175–2186 (1984).
165. Gu, Y. *et al.* Rotational dynamics of cargos at pauses during axonal transport. *Nat. Commun.* **3,** 1030–1038 (2012).
166. Gu, Y., Sun, W., Wang, G. & Fang, N. Single particle orientation and rotation tracking discloses distinctive rotational dynamics of drug delivery vectors on live cell membranes. *J. Am. Chem. Soc.* **133,** 5720–5723 (2011).
167. Mizuno, H. & Watanabe, N. mDia1 and formins: screw cap of the actin filament. *Biophysics (Oxf).* **8,** 95–102 (2012).
168. Dahan, M., Le, S. & Luccardini, C. Diffusion Dynamics of Glycine Receptors Revealed by Single – Quantum Dot Tracking. **302,** 2000–2003 (2003).
169. Gal, N., Lechtman-Goldstein, D. & Weihs, D. Gal, N., D. Lechtman-Goldstein and D. Weihs, 'Particle tracking in living cells: a review of the mean square displacement method and beyond', Rheol. Acta 52 , 425-443 (2013). *Rheol. Acta* **52,** 425–443 (2013).
170. Bonacina, L. Nonlinear nanomedecine: Harmonic nanoparticles toward targeted diagnosis and

therapy. *Mol. Pharm.* **10,** 783–792 (2013).

171. Staedler, D. *et al.* Harmonic nanocrystals for biolabeling: A survey of optical properties and biocompatibility. *ACS Nano* **6,** 2542–2549 (2012).
172. McGuinness, L. P. *et al.* Quantum measurement and orientation tracking of fluorescent nanodiamonds inside living cells. *Nat. Nanotechnol.* **6,** 358–363 (2011).
173. Forkey, J. N., Quinlan, M. E., Shaw, M. A., Corrie, J. E. & Goldman, Y. E. Three-dimensional structural dynamics of myosin V by single-molecule fluorescence polarization. *Nature* **422,** 399–404 (2003).
174. Beausang, J., Sun, Y., Quinlan, M., Forkey, J. & Goldman, Y. The Polarized Total Internal Reflection Fluorescence Microscopy (polTIRFM) Processive Motility Assay for Myosin V. *Cold Spring Harb. Protoc.* **151,** 414–420 (2013).
175. Ohmachi, M. *et al.* Fluorescence microscopy for simultaneous observation of 3D orientation and movement and its application to quantum rod-tagged myosin V. *Proc. Natl. Acad. Sci.* **109,** 5294–5298 (2012).
176. Spetzler, D. *et al.* Microsecond Time Scale Rotation Measurements of Single F1 ATPase Molecules. *Biochemistry* **45,** 3117–3124 (2006).
177. Sönnichsen, C. & Alivisatos, A. P. Gold nanorods as novel nonbleaching plasmon-based orientation sensors for polarized single-particle microscopy. *Nano Lett.* **5,** 301–304 (2005).
178. Chang, W.-S., Ha, J. W., Slaughter, L. S. & Link, S. Plasmonic nanorod absorbers as orientation sensors. *Proc. Natl. Acad. Sci.* **107,** 2781–2786 (2010).
179. Wang, G., Sun, W., Luo, Y. & Fang, N. Resolving rotational motions of nano-objects in engineered environments and live cells with gold nanorods and differential interference contrast microscopy. *J. Am. Chem. Soc.* **132,** 16417–16422 (2010).
180. Sun, W., Wang, G., Fang, N. & Yeung, E. S. Wavelength-dependent differential interference contrast microscopy: selectively imaging nanoparticle probes in live cells. TL - 81. *Anal. Chem.* **81,** 9203–9208 (2009).
181. Zhang, B., Liu, B., Liao, J., Chen, G. & Tang, D. Novel electrochemical immunoassay for quantitative monitoring of biotoxin using target-responsive cargo release from mesoporous silica nanocontainers. *Anal. Chem.* **85,** 9245–9252 (2013).
182. Tcherniak, A. *et al.* One-photon plasmon luminescence and its application to correlation spectroscopy as a probe for rotational and translational dynamics of gold nanorods. *J. Phys. Chem. C* **115,** 15938–15949 (2011).
183. Geissbuehler, M. *et al.* Nonlinear correlation spectroscopy (NLCS). *Nano Lett.* **12,** 1668–1672 (2012).

184. Extermann, J. *et al.* Nanodoublers as deep imaging markers for multi-photon microscopy. *Opt. Express* **17,** 15342–15349 (2009).
185. Van Den Broek, B., Ashcroft, B., Oosterkamp, T. H. & Van Noort, J. Parallel nanometric 3D tracking of intracellular gold nanorods using multifocal two-photon microscopy. *Nano Lett.* **13,** 980–986 (2013).
186. Xiao, L., Qiao, Y., He, Y. & Yeung, E. S. Imaging translational and rotational diffusion of single anisotropic nanoparticles with planar illumination microscopy. *J. Am. Chem. Soc.* **133,** 10638–10645 (2011).
187. Marchuk, K., Ha, J. W. & Fang, N. Three-dimensional high-resolution rotational tracking with superlocalization reveals conformations of surface-bound anisotropic nanoparticles. *Nano Lett.* **13,** 1245–1250 (2013).
188. Hsieh, C. L., Grange, R., Pu, Y. & Psaltis, D. Three-dimensional harmonic holographic microcopy using nanoparticles as probes for cell imaging. *Opt. Express* **17,** 2880–2891 (2009).
189. Yan, E. C. Y. & Eisenthal, K. B. Rotational Dynamics of Anisotropic Microscopic Particles Studied by Second Harmonic Generation. *J. Phys. Chem. B chem* **104,** 6686–6689 (2000).
190. Bonacina, L. *et al.* Polar Fe(IO3)3 nanocrystals as local probes for nonlinear microscopy. *Appl. Phys. B Lasers Opt.* **87,** 399–403 (2007).
191. Sandeau, N. *et al.* Defocused imaging of second harmonic generation from a single nanocrystal. *Opt. Express* **15,** 16051 (2007).
192. Pu, Y., Grange, R., Hsieh, C. L. & Psaltis, D. Nonlinear optical properties of core-shell nanocavities for enhanced second-harmonic generation. *Phys. Rev. Lett.* **104,** 207402-1 (2010).
193. Brasselet, S. *et al.* In situ diagnostics of the crystalline nature of single organic nanocrystals by nonlinear microscopy. *Phys. Rev. Lett.* **92,** 1–4 (2004).
194. Pinaud, F., Clarke, S., Sittner, A. & Dahan, M. Probing cellular events, one quantum dot at a time. *Nat. Methods* **7,** 275–285 (2010).
195. Magouroux, T. *et al.* High-speed tracking of murine cardiac stem cells by harmonic nanodoublers. *Small* **8,** 2752-2756 (2012).
196. Kachynski, A., Kuzmin, A., Nyk, M., Roy, I. & Prasad, P. Zinc Oxide Nanocrystals for Non-resonant Nonlinear Optical Microscopy in Biology and Medicine. *J. Phys. Chem. C Nanomater Interfaces* **112,** 10721–10724 (2008).
197. Ladj, R. *et al.* SHG Active $Fe(IO_3)_3$ particles: From spherical nanocrystals to urchin-like microstructures through the additive-mediated microemulsion route. *Cryst. Growth Des.* **12,** 5387–5395 (2012).
198. Mayer, L. *et al.* Single KTP nanocrystals as second-harmonic generation biolabels in cortical

neurons. *Nanoscale* **5,** 8466–8471 (2013).

199. Hunter, R. J. *Foundations of Colloid Science*. (2002).
200. De Beer, A. G. F., De Aguiar, H. B., Nijsen, J. F. W. & Roke, S. Detection of buried microstructures by nonlinear light scattering spectroscopy. *Phys. Rev. Lett.* **102,** 6–9 (2009).
201. Macias-Romero, C. *et al.* High throughput second harmonic imaging for label-free biological applications. *Opt. Express* **22,** 31102–12 (2014).
202. Gustafsson, M. G. L. Nonlinear structured-illumination microscopy: wide-field fluorescence imaging with theoretically unlimited resolution. *Proc. Natl. Acad. Sci. U. S. A.* **102,** 13081–13086 (2005).
203. Mertz, J. & Kim, J. Scanning light-sheet microscopy in the whole mouse brain with HiLo background rejection. *J. Biomed. Opt.* **15,** 016027 (2010).
204. Lim, D., Ford, T. N., Chu, K. K. & Mertz, J. Optically sectioned in vivo imaging with speckle illumination HiLo microscopy. *J. Biomed. Opt.* **16,** 016014 (2011).
205. Lim, D., Chu, K. K. & Mertz, J. Wide-field fluorescence sectioning with hybrid speckle and uniform-illumination microscopy. *Opt. Lett.* **33,** 1819–1821 (2008).
206. Michaelson, J., Choi, H., So, P. & Huang, H. Depth-resolved cellular microrheology using HiLo microscopy. *Biomed. Opt. Express* **3,** 1241 (2012).
207. Macias-Romero, C., Nahalka, I., Okur, H. I. & Roke, S. Optical imaging of surface chemistry and dynamics in confinement. *Science* **788,** 784–788 (2017).
208. Toney, G. M. Regulation of neuronal cell volume: from activation to inhibition to degeneration. *J Physiol* **58818,** 3347–3348 (2010).
209. Jaqaman, K. *et al.* Robust single particle tracking in live cell time-lapse sequences. *Nat. Methods* **5,** 695–702 (2008).
210. Tivenez, J. Y. Mean square displacement analysis of particles trajectories. *MATLAB file Exch.* **8,** 2013 (2013).
211. Macias-Romero, C. *et al.* Probing rotational and translational diffusion of nanodoublers in living cells on microsecond time scales. *Nano Lett.* **14,** 2552–2557 (2014).
212. Macias-Romero, C., Zubkovs, V., Wang, S. & Roke, S. Wide-field medium-repetition-rate multiphoton microscopy reduces photodamage of living cells. *Biomed. Opt. Express* **7,** 1458 (2016).
213. Hammond, J., *et al.* Posttranslational modifications of tubulin and the polarized transport of Kinesin-1 in neurons. *Mol. biology of the cell* **21,** 4042-4056 (2010).
214. Gibbs-Davis, J. M., Kruk, J. J., Konek, C. T., Scheidt, K. A. & Geiger, F. M. Jammed Acid - Base Reactions at Interfaces. *JACS* **130,** 15444–15447 (2008).

215. Yamaguchi, T., Nishizaki, K. & Itai, S. Molecular interactions between phospholipids and electrolytes in a monolayer of parenteral lipid emulsion. *Colloids Surfaces B Biointerfaces* **9,** 275–282 (1997).
216. Wilson, J. D., Bigelow, C. E., Calkins, D. J. & Foster, T. H. Light scattering from intact cells reports oxidative-stress-induced mitochondrial swelling. *Biophys. J.* **88,** 2929–2938 (2005).
217. Brawley, S. H. & Quatrano, R. S. Effects of Microtubule Inhibitors on Pronuclear Migration and Embryogenesis in Fucus Distichus(Phaeophyta). *J. Phycol.* **15,** 266–272 (1979).
218. Hoebeke, J., Van Nijen, G. & De Brabander, M. Interaction of oncodazole (R 17934), a new anti-tumoral drug, with rat brain tubulin. *Biochem. Biophys. Res. Commun.* **69,** 319–324 (1976).
219. Wachsmann-Hogiu, S., Hwang, J. Y., Lindsley, E. & Farkas, D. L. Wide-field two-photon microscopy: features and advantages for biomedical applications. *SPIE* **6441,** (2007).
220. Stepanova, T. *et al.* History-dependent catastrophes regulate axonal microtubule behavior. *Curr. Biol.* **20,** 1023–1028 (2010).
221. Macias-Romero, C. & Török, P. Eigenvalue calibration methods for polarimetry. *J. Eur. Opt. Soc.* **7,** 1990–2573 (2012).
222. Levine, B. F., Bethea, C. G., Levine, B. F. & Bethea, C. G. Second and third order hyperpolarizabilities of organic molecules. *J. Chem. Phys.* **63,** 2666–2682 (1975).
223. Stoothoff, W. H., Bacskai, B. J. & Hyman, B. T. Monitoring tau-tubulin interactions utilizing second harmonic generation in living neurons. *J. Biomed. Opt.* **13,** 064039 (2014).
224. Boyd, W. R. *Nonlinear Optics.* (1992).
225. Goldstein, H., Poole, C. P. & Safko, J. L. *Classical Mechanics 3rd edition*. (2001).
226. Sharoukhov, D. & Lim, H. On probing conformation of microtubules by second-harmonic generation. *J. Mod. Opt.* **63,** 71–75 (2016).
227. Tuer, A. E. *et al.* Hierarchical model of fibrillar collagen organization for interpreting the second-order susceptibility tensors in biological tissue. *Biophys. J.* **103,** 2093–2105 (2012).
228. Psilodimitrakopoulos, S. *et al.* Estimation of the effective orientation of the SHG source in primary cortical neurons. **17,** 11370–11375 (2009).
229. Odin, C., Heichette, C., Chretien, D. & Le Grand, Y. Second harmonic microscopy of axonemes. *Opt. Express* **17,** 9235–9240 (2009).
230. Yu, C. H. *et al.* Measuring microtubule polarity in spindles with second-harmonic generation. *Biophys. J.* **106,** 1578–1587 (2014).
231. Brasselet, S. in *Advances in Optics and Photonics* **3,** 205 (2011).
232. Chen, X., Nadiarynkh, O., Plotnikov, S. & Campagnola, P. J. Second harmonic generation

microscopy for quantitative analysis of collagen fibrillar structure. *Nat. Protoc.* **7,** 654–669 (2012).

233. Baas, P. W. & Lin, S. Hooks and comets: The story of microtubule polarity orientation in the neuron. *Dev. Neurobiol.* **71,** 403–418 (2011).
234. Craig, A. M. & Branker, G. Neuronal polarity. *Annu. Rev. Neurosci.* **17,** 267–310 (1994).
235. Piperno, G., LeDizet, M. & Chang, X. J. Microtubules containing acetylated alpha-tubulin in mammalian cells in culture. *J. Cell Biol.* **104,** 289–302 (1987).
236. Bulinski, J. & Gundersen, G. Stabilization of post-translational modification of microtubules during cellular morphogenesis. *BioEssays News Rev. Mol.* **13,** 1991 (1991).
237. Kempf, M., Clement, A., Faissner, A., Lee, G. & Brandt, R. Tau binds to the distal axon early in development of polarity in a microtubule- and microfilament-dependent manner. *J. Neurosci.* **16,** 5583–92 (1996).
238. Baas, P. W., Black, M. M. & Banker, G. A. Changes in microtubule polarity orientation during the development of hippocampal neurons in culture. *J. Cell Biol.* **109,** 3085–3094 (1989).
239. Beckervordersandforth, R. Mitochondrial Metabolism-Mediated Regulation of Adult Neurogenesis. *Brain Plast.* **3,** 1–15 (2017).
240. Flynn, K. C. The cytoskeleton and neurite initiation. *Bioarchitecture* **3,** 86–109 (2013).
241. Gallo, G. Coordination of the axonal cytoskeleton during the emergence of axon collateral branches. *Neural Regen. Res.* **11,** 2016–2018 (2016).
242. Hagg, T. & Oudega, M. Neural Degeneration and Regeneration Myelin and Scar-Derived Inhibition. *J. Neurotrauma* **23,** 264–280 (2006).
243. Larner, A. J. Physiological and pathological interrelationships of amyloid beta peptide and the amyloid precursor protein. *Bioessays* **17,** 819–824 (1995).
244. Kevenaar, J. T. & Hoogenraad, C. C. The axonal cytoskeleton: from organization to function. *Front. Mol. Neurosci.* **8,** 1–12 (2015).
245. Schuyler, S. C. & Pellman, D. Microtubule 'plus-end-tracking proteins': The end is just the beginning. *Cell* **105,** 421–424 (2001).
246. McNally, F. J. Cytoskeleton: Clasping on to the end. *Nat. Rev. Mol. Cell Biol.* **2,** 321 (2001).
247. Tang, F. Netrin-1 Induces Axon Branching in Developing Cortical Neurons by Frequency-Dependent Calcium Signaling Pathways. *J. Neurosci.* **25,** 6702–6715 (2005).
248. Lau, P. M., Zucker, R. S. & Bentley, D. Induction of filopodia by direct local elevation of intracellular calcium ion concentration. *J. Cell Biol.* **145,** 1265–1275 (1999).
249. Spillane, M., Ketschek, A., Merianda, T. T., Twiss, J. L. & Gallo, G. Article Mitochondria Coordinate Sites of Axon Branching through Localized Intra-axonal Protein Synthesis.

CellReports **5,** 1564–1575 (2013).

250. Courchet, J. *et al.* Terminal axon branching is regulated by the LKB1-NUAK1 kinase pathway via presynaptic mitochondrial capture. *Cell* **19,** 389–399 (2009).
251. Ketschek, A. *et al.* Nerve growth factor promotes reorganization of the axonal microtubule array at sites of axon collateral branching. *Dev. Neurobiol.* **75,** 1441–1461 (2015).
252. Winkle, C., Hanlin, C. & Gupton, S. Utilizing Combined Methodologies to Define the Role of Plasma Membrane Delivery During Axon Branching and Neuronal Morphogenesis Cortney Access. *J. Vis. Exp.* **67,** 558–569 (2015).
253. Magistretti, P. J. & Allaman, I. Review A Cellular Perspective on Brain Energy Metabolism and Functional Imaging. *Neuron* **86,** 883–901 (2015).
254. Wong-Riley, M. T. T. Cytochrome oxidase: an endogenous marker for neuron activity. *Trends Neurosci.* **12,** 94–101 (1989).
255. Mandell, J. W. & Banker, G. A. The microtubule cytoskeleton and the development of neuronal polarity. *Neurobiol. Aging* **16,** 229–238 (1995).
256. Stiess, M. *et al.* Axon Extension Occurs Independently of Centrosomal Microtubule Nucleation. *Science* **327,** 704–707 (2010).
257. de Anda, F. C. *et al.* Centrosome localization determines neuronal polarity. *Nature* **436,** 704–708 (2005).
258. Liu, M. *et al.* Kinesin-12, a Mitotic Microtubule-Associated Motor Protein, Impacts Axonal Growth, Navigation, and Branching. *J. Neurosci.* **30,** 14896–14906 (2010).
259. Baas, P. W., Black, M. M. & Banker, G. a. Changes in microtubule polarity orientation during the development of hippocampal neurons in culture. *J. Cell Biol.* **109,** 3085–94 (1989).
260. Ketschek, A., Jones, S. & Gallo, G. Axon Extension in the Fast and Slow Lanes: Substratum-Dependent Engagement of Myosin II Functions Andrea. *Neurobiology* **67,** 1305–1320 (2009).
261. Wang, L. & Brown, A. Rapid movement of microtubules in axons. *Curr. Biol.* **12,** 1496–1501 (2002).
262. Dent, E. W., Gupton, S. L. & Gertler, F. B. The Growth Cone Cytoskeleton in Axon Outgrowth and Guidance. *Cold Sping Harbor Persp. in Biol.* **3,** 1-39 (2011).
263. Blagosklonny, M. V, Streets, C., Hall, M. N., Commons, C. & License, A. Growth and aging : a common molecular mechanism Mikhail. *AGING* **1,** 357–362 (2009).
264. Hodgkin, A. L. & Huxley, A. F. A quantitative description of membrane current and its application to conduction and excitation in nerve. *Bull. Math. Biol.* **52,** 25–71 (1952).
265. Purves, D. *et al. Neuroscience.* Sunderland (2004).
266. Lütgebaucks, C., Gonella, G. & Roke, S. Optical label-free and model-free probe of the surface

potential of nanoscale and microscopic objects in aqueous solution. *Phys. Rev. B* **94,** 2–7 (2016).

267. Gonella, G., Lütgebaucks, C., De Beer, A. G. F. & Roke, S. Second harmonic and sum-frequency generation from aqueous interfaces is modulated by interference. *J. Phys. Chem. C* **120,** 9165–9173 (2016).
268. Ong, S., Zhao, X. & Eisenthal, K. B. Polarization of water molecules at a charged interface: second harmonic studies of the silica/water interface. *Chem. Phys. Lett.* (1992).
269. Macias-Romero, C., Nahalka, I., Okur, H. I. & Roke, S. Optical imaging of surface chemistry and dynamics in confinement. *Science* **357,** 784–788 (2017).
270. Tarun, O. B., Hannesschläger, C., Pohl, P. & Roke, S. Label-free and charge-sensitive dynamic imaging of lipid membrane hydration on millisecond time scales. *Proc. Natl. Acad. Sci.* **10,** 1–6 (2018).
271. Moerner, W. E. Microscopy beyond the diffraction limit using actively controlled single molecules. *J. Microsc.* **246,** 213–220 (2012).
272. Lesage, F. Pharmacology of neuronal background potassium channels. *Neuro Pharmacol.* **44,** 1–7 (2003).
273. Coster, H. G. L. The Physics of Cell Membranes. *J. Biol. Phys.* **29,** 363–399 (2003).
274. Chance, B., Jobsis, F., Schoener, B. & Cohen, P. Intracellular oxidation-reduction states in vivo. *Science* **137,** 499–508, (1962).
275. Erni, R., Rossell, M. D., Kisielowski, C., Dahmen U., Atomic-Resolution Imaging with a Sub-50-pm Electron Probe. *Phys. Rev. Let.***102,** 096101 (2009).
276. Perlson, E., *et al.* Retrograde axonal transport: pathways to cell death? *Trends Neurosci.* **33,** 335-344, (2010).
277. Kuijpers, M., & Hoogenraad, C.C., Centrosomes, microtubules and neuronal development. *Mol. Cell Neurosci.* **48,** 349-358 (2011).
278. Yizhar, O., Fenno, L. E., Davidson, T. J., Mogri, M. & Deisseroth, K. Optogenetics in neural systems. *Neuron* **71,** 9-34 (2011).
279. Gell, C., *et al.* Microtubule dynamics reconstituted in vitro an imaged by single-molecule fluorescence microscopy. *Methods Cell Biol.* **95,** 221-245 (2010).
280. Gell, C., Brockwell, D. J., and Smith, D.A.M. Handbook of Single Molecule Fluorescence Spectroscopy." Oxford, UK, Oxford University Press (2006).
281. Personal communication, 2017.
282. Pokorný, J., Jelínek, F., Trkal, V., Lamprecht, I & Hölzel, R. Vibrations in microtubules. *Astrophys. Space Sci.* **23,** 171-179 (1997).

283. Pokorný, J., Electric field around microtubules. *Bioelectrochemistry and Bioenergetics* **45,** 239-245 (1998).

284. Niggli, V. & Burger, M. Interaction of the cytoskeleton with the plasma membrane. *J. of Membrane Bio.* **2,** 97-121 (1987).

285. Aszalos, S., Damjanovich, S. & Gottesman, M. M. Depolymerization of microtubules alters membrane potential and affects the motional freedom of membrane proteins. *Biochem.* **25,** 5804-5809 (1986).

286. Allen, K., B., Sasoglu, F. & Layton, B. Cytoskeleton-membrane interactions in neuronal growth cones: a finite analysis study. *J. Biom. Eng.* **131,** 021006 (2009).

287. Sivaguru, M., Pike, S., Gassmann, W. & Baskin, T. Aluminum rapidly depolymerizes cortical microtubules and depolarizes the plasma membrane: evidence that these responses are mediated by a glutamate receptor. *Plant & cell phys.* **44,** 667-675 (2003).

Marie DIDIER
+41789497859
mariedidier1@gmail.com
French, 6th of May 1987

Pluridisciplinary imaging methods In Art & Science

Work experience

May 2013 – Nov. 2018

PhD employee,
Marie Curie Early Stage Researcher (FINON network)
Non destructive, label-free, time resolved non linear imaging of neuronal activity
Nonlinear optics, second harmonic generation, data denoising, Neurosciences, microscopy
Supervisor: Sylvie Roke**, LBP** (Laboratory for fundamental BioPhotonics), **EPFL,** Switzerland

September 2012 – April 2013

Kress-Mellon Fellow in Imaging Science
IR Reflectography, Improving underdrawing visualization in masterpiece's paintings using Hyperspectral and Multispectral imaging
Image processing with Matlab, Kubelka-Monk algorithms, optics in complex media, impressionism
Supervisor: John Delaney, **National Gallery of Art,** USA

March 2012 – July 2012

Internship / Master project
3D characterization of collagen fibril organization in human cornea using multiphoton microscopy
Nonlinear optics, image processing with Matlab, Hough transform algorithms
Supervisors: Marie-Claire Schanne-Klein**, LOB, Ecole Polytechnique,** France

February 2011 – July 2011

Internship / Master project
UV-visible luminescence of Stradivarius' varnishes
Statistical treatment of spectral data in R, Synchrotron experiments
Supervisor: Jean-Philippe Echard**, Laboratoire de recherche du Musée de la musique**, France

June 2010 – August 2010

Internship / Master project
Terahertz Imaging applied on paintings
Experimental setups on optical bench, 3D reconstruction with Matlab, Radon transform algorithms
Supervisor: Patrick Mounaix, **Centre de Physique Moléculaire d'Optique Hertzienne**, France

June 2009 – August 2009

Intern Master 1
The non proportionnality in inorganics scintillators
Theoritical physics, photon-matter interactions
Supervisor: Gregory Bizarri, **Lawrence Berkeley National Laboratory**, USA

Education and training

September 2011 - 201

Master 2 : (with honors) Optics, matter, plasma : Light, matter, extreme measurements
Lasers, spectroscopy, non-linear optics, near-field microscopy, optical microscopies, biophotonics
Université Pierre et Marie Curie, Paris 6, France, **14.2/20**

September 2010 – June 2011

Master 2 : (with honors) Materials and cultural heritage

Methods of characterization and datation of archaeological and art objects, museography, art history

CRP2A, Maison de l'archéologie and Université de Bordeaux 3, Talence, France, **14.5/20**

September 2009 – June 2010

Master 1 : Physical sciences Université Claude Bernard Lyon 1, Villeurbanne, France

Optics and lasers, particles physics, atoms and molecules, solid states physics, quantum mechanics, nanomaterials, statisctical phyics

September 2007 – January 2009

Bachelor : Physics Université Claude Bernard Lyon 1, Villeurbanne, France

Bachelor : Exchange program University of Western Ontario, London, Canada

Awarded prices and grants

- 2018, **Awarded mentee** for the one-to-one mentoring 1-year program "Fix the leaky pipeline" from ETHZ domain, Switzerland
- 2017, Best Flash Presentation, FOM conference, Bordeaux, France
- 2015, Best Flash Presentation of my Thesis for the Photonics Days, EPFL, Switzerland
- 2015, Student Poster Award for the Bio Engineering Days, EPFL, Switzerland
- 2013-2017, **Marie Curie Early Stage Researcher** (FINON: Female Investigation for Nonlinear Optics and Nanoscopy)**,** EPFL, Switzerland
- 2012-2013, **Kress-Mellon Fellowship** in Imaging Science**,** National Gallery of Art in Washington DC, USA
- 2011, **COST IE0601 & MP0601 Training School**, *"Wood Cultural Heritage conservation: advanced X-ray and optical techniques",* Italy

Publications

- M. Didier, P. Jourdain, S. Roke "Probing neuronal morphology and metabolic activity with label-free SH polarimetry and endogenous 2PEF", *in preparation,* **2018.**
- M. Didier, C. Macias-Romero, C. Teulon, P. Jourdain, S. Roke "Mapping of morphological changes in the neuronal cytoskeleton with endogenous second harmonic imaging: A case study of nocodazole", *submitted*, *in the process of responding to referees,* **Cytoskeleton, 2018.**
- M. Didier, O. Tarun, P. Jourdain, P. Magistretti, S. Roke "Membrane water as a probe for neuronal membrane potentials and ionic flux at the single cell level", *submitted*, *in the process of responding to referees,* **Nature Communications, 2018.**
- C. Macias-Romero, C. Teulon, M. Didier, S. Roke, "Edogenous SHG and 2PEF coherence imaging of substructures in neurons in 3D", *accepted,* **Optics Express**, **2018**
- J. K. Delaney, G. Trumpy, M. Didier, P. Ricciardi, K. Dooley, "A high sensitivity, low noise and high spatial resolution multi-band infrared reflectography camera for the study of paintings and works on paper", **Heritage Science**, **2017.**
- J.-P. Echard, M. Thoury, B. Berrie, T. Severin-Fabiani, A. Vichi**,** M. Didier, M. Refregiers, L. Bertrand, "Synchrotron DUV luminescence micro-imaging to identify and map historical organic coatings on wood", **The Analyst** 140(15), **2015.**
- C. Macias-Romero, M. Didier, P. Jourdain, P. Marquet, P. Magistretti, O. Tarun, S. Roke, "High throughput second harmonic imaging for label-free biological applications", **Optics Express** 22(25), **2014.**
- C. Macias-Romero, M. Didier, V. Zubkovs, L. Delannoy, F. Dutto, A. Radenovic, S. Roke, "Probing Rotational and Translational Diffusion of Nanodoublers in Living Cells on Microsecond Time Scales", **Nano Letters** 14(5), **2014.**
- G. Latour, J.-P. Echard, M. Didier, M.-C. Schanne-Klein, "Multiphoton microscopy: an efficient tool for in situ study of historical artifacts", **SPIE, 2013.**

Personal skills & committees

Recent Scientific outreach :

- Course and obtention of **Leadership certificate**, EPFL/ETH, May 2018
- "Fix the leaky pipeline" for **Women in Science** kick off event, Bern, 2018
- Organized the Girls & Science event in my laboratory, EPFL, Switzerland 2016
- Hosted high school students within the Open doors event for new EPFL students, Switzerland, 2016 and 2017 and organized a visit of EPFL campus
- Interviewed for the video promotion for the Photonics Doctoral School, EPFL, 2016

Committees

Team work, philantropy & committees:

- **President of ACIDE association**, (Association du Corps Intermédiaire & Doctorant-e-s de l'EPFL)
- **Representing member at the Bureau of the School Assembly (AE)**
- **Representing member of the Intermediate Staff (CI) at the School Assembly (AE)**
- **2nd Price winner with Juvenilia association for the European Charlemagne Youth Prize,** Aachen, Germany, 2018
- **Elected board member: Event coordinator for Juvenilia**, The European Network of the Young Opera Friends 2018 – 2-year mandate –
- **Representative member of CI (Corps intermediaire) for the STI Faculty at the Assemblée d'Ecole (EPFL)** (Science and Technique de l'Ingenieur), EPFL, 2018
- **Young Patron** of Salzburg Easter Festival, 2017-ongoing
- **Public Relations and sponsoring** for FORUM EPFL, (organizer of one of the biggest career fairs in Europe), 2014-2016
- Member of **LEO Club Lausanne** (Junior of Lions Club) 2015-2017
- **Patron member** of **Juvenilia**: The European Network of the Young Opera Friends 2015-2017
- **Representative and patron member** of the Junior Club Committee of AROP (Association pour le rayonnement de l'Opera de Paris,), 2012-2017
- Consul of Lausanne Art Group for Internations, 2015
- **Patron member** of The John F. Kennedy Center for the Performing Arts, Washington DC, 2013-2014

Social skills

Volunteer work :

- Reporter for the Tech4Dev UNESCO conference, Switzerland, 2015
- Volunteer for Lausanne Underground Film and Music Festival, 2014-2018
- Volunteer in fundraising for WETA classical radio, Washington DC, 2012
- Volunteer for National Gallery Classical Concerts, 2012
- Volunteer firefighter and Emergency Medical Service (with diploma, 1997-2011)
- Volunteer at Mac Intosh Art Gallery, University of Western Ontario, London, Canada

Artistic skills

- Exhibition of my water color works with CreaPoly, EPFL, Switzerland, 2017
- Piano and music theory, 3rd degree Conservatory diploma, France
- Piano, chamber orchestra, music theory and improvisation, Saint-Fonds Music School, France
- Art, painting, drawing and sculpting studies for 10 years
- **Book Illustrator** : « La poétique de la maison musée, 1847-1989 », by B. Bourgeois
- **Exhibition** of my drawings and paintings, London, Ontario, Canada, 2008
- In 2008, during my exchange year, I represented my country (France) at a multicultural event in King's College University in London, Canada with a french composers **piano recital**